6-23-2015

The Nucleation and Growth of Nanoparticles for Heterogeneous Catalysis

Angelica Benavidez

Recommended Citation

Benavidez, Angelica. "The Nucleation and Growth of Nanoparticles for Heterogeneous Catalysis." (2015).
https://digitalrepository.unm.edu/cbe_etds/30

Angelica Benavidez
Candidate

Chemical and Biological Engineering
Department

This dissertation is approved, and it is acceptable in quality and form for publication:

Approved by the Dissertation Committee:

Abhaya Datye , Chairperson

Ronald Loehman

Ayman Karim

Sivakumar Challa

THE NUCLEATION AND GROWTH OF NANOPARTICLES FOR HETEROGENEOUS CATALYSIS

by

ANGELICA BENAVIDEZ

B.S., Chemical Engineering, The University of New Mexico, 2009

DISSERTATION

Submitted in Partial Fulfillment of the
Requirements for the Degree of

Doctor of Philosophy
Engineering

The University of New Mexico
Albuquerque, New Mexico

May 2015

DEDICATION

To Jacob and Carlos

You are my inspiration, I love you

And also to the rest my family, especially Mom and Dad

Without your unconditional love and support, this wouldn’t have been possible

Acknowledgements

I would like to thank my advisor, Professor Abhaya Datye, for your support and encouragement. I will always be grateful for the guidance and opportunities you provided to me.

I would like to acknowledge the other members of my committee. Dr. Ayman Karim, thank you for allowing me to spend time in your lab and for your guidance and patience teaching me EXAFS. Dr. Sivakumar Challa, thank you for all the interesting discussions on nucleation and sintering. And Dr. Ronald Loehman, thank you for your willingness and enthusiasm to serve on my committee.

I would also like to thank the Heterogeneous Catalysis Research Group; everyone was always more than willing to help and teach, and for all the useful discussions.

I would also like to acknowledge NSF for my financial support through the GRFP, LSAMP-BD, and IGERT fellowships.

And I would like to thank the invaluable friends I have made through this journey, especially Ulises Martinez and Jonathan Paiz. Ulises, you were always there to give support, encouragement, and comfort when I needed it most, thank you.

THE NUCLEATION AND GROWTH OF NANOPARTICLES FOR HETEROGENEOUS CATALYSIS

By

Angelica Benavidez

B.S., Chemical Engineering, The University of New Mexico, 2009

Ph.D., Engineering, The University of New Mexico, 2015

ABSTRACT

These studies investigate the nucleation and growth of nanoparticles and how their interaction with a support affects their reactivity as a heterogeneous catalyst. As capabilities in both synthesis methods and characterization methods advance, the use of nanoparticles and sub-nanometer species are more commonly used. These small particles introduce new factors that can cause differences in reactivity.

Various catalyst synthesis methods are employed to deposit mono-dispersed particles on different oxide and carbon supports. Electron microscopy is used to study nanoparticle sintering and the careful tracking of individual particles gives insight into growth mechanisms. X-ray absorption spectroscopy measurements are used to characterize catalysts and elucidate the reasons for a support effect in both hydrogenation and oxidations reactions.

This investigation aims to produce a more active catalyst by exploring different aspects that play a role in reactivity and selectivity. Understanding the growth

mechanisms that commonly to lead deactivation gets us one step closer to creating a sinter resistant catalyst. These studies also show that changing a catalyst support can increase its activity. The exploration of the fundamentals of nanoparticle structure and interaction with its surroundings leads to a more efficient catalyst.

Table of Contents

List of Figures

List of Tables

1. Introduction

1.1 Statement of the Research Problem

This research is aimed at understanding the atomic scale details of nanoparticles that are relevant to heterogeneous catalysis. Catalysts accelerate the rate of a reaction and modify the selectivity of chemical reactions to produce desirable products. Heterogeneous catalysts constitute about 75% of the total use of catalysts in industry. They typically consist of an active metal phase dispersed on a support, usually a high surface area oxide, or carbon. Catalysis is a surface phenomenon, hence it is important to control the size of the active phase on the scale of atoms to a few nanometers. The hypothesis guiding this work is that controlling nucleation sites on a catalyst support will lead to improved dispersion as thus improved performance which will be a major advance for heterogeneous catalysts. There are two challenges for highly dispersed catalysts, synthesizing and maintaining the small particle size. Improved synthesis techniques have made it possible to generate nanoparticles and sub-nanometer species of uniform size and composition onto a support surface. A challenge is to retain these particles in their original size, and to slow the rates of coalescence and ripening that lead to particle growth. As we move towards the use of smaller metal species on a support, the metal-support interaction is increased. It would be desirable to develop catalysts that are more robust and understanding the sintering behavior and effect of the support could do this. This research applies techniques such as aberration corrected electron microscopy and X-ray absorption spectroscopy to increase our knowledge of the atomic scale details of heterogeneous catalysts.

1.2 Catalysis

Catalysts play an important role in our everyday lives, from the production of energy, chemicals, and polymers to maintaining a cleaner environment through the purification of automotive emissions and wastewater treatment. Today, over 85% of chemical processes utilize catalysts [1]. They are immensely important in all aspects of chemical industry as they are used to produce high volume chemicals such as polymers, petrochemicals, and ammonia. Catalysts also play a big role in petroleum refining, production of pharmaceuticals, and in the prevention and abatement of pollution.

Catalysts are substances that change the kinetics of a chemical reaction without being consumed. Although catalysts can be inhibitors, they are typically used to accelerate the rate of reaction allowing a reaction to proceed more quickly and/or at lower temperatures and pressures, thus consuming less energy. They are also used to modify the selectivity of a reaction allowing for the increased production of desirable products.

Figure 1.1 shows a potential energy diagram for a catalytic and a non-catalytic reaction. The reactants, A and B, must collide with sufficient energy to overcome the activation barrier (E_a) in order to form the product, C. The change is Gibbs free energy (ΔG) is the energy difference between the reactants and the products and remains unchanged with the use of a catalyst. A catalyst allows for an alternative reaction pathway that is more energetically favorable and decreases the activation energy. There are two types of catalysts, homogeneous and heterogeneous. Homogeneous catalysts are in the same phase as the reactants, mostly commonly both being in the liquid phase.

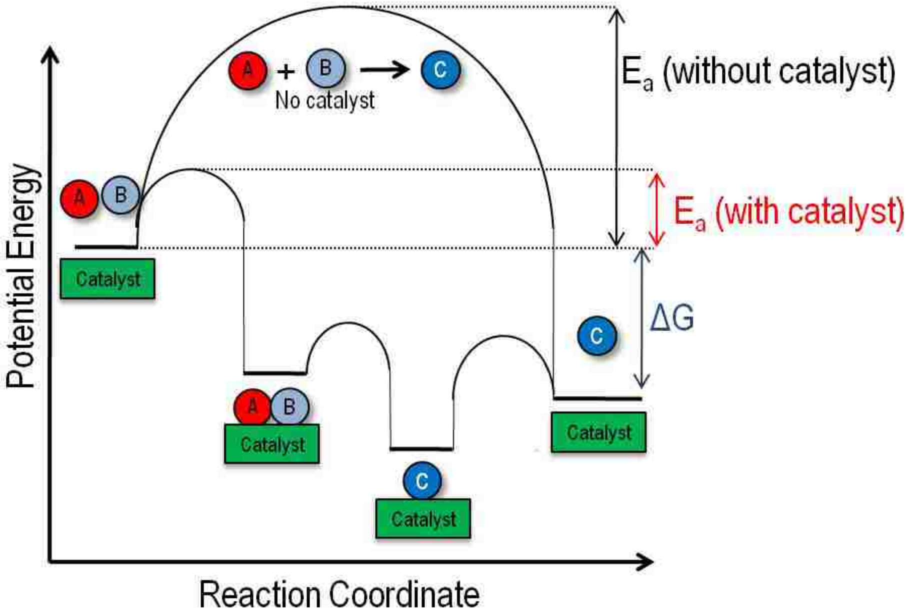

Figure 1.1 Potential energy diagram showing the differences between catalytic and a non-catalytic reaction.

Heterogeneous catalysts are typically solids while the reactants are either gas or liquid and consist of an active metal phase dispersed on a support. The support is usually a high surface area metal oxide or carbon. Metal catalyst particles are often present in the form of nanoparticles and the control of their size is an area of interest. Particle size control is important to minimize the amount of catalyst used, which is typically a precious metal, as well as to maximize the activity by increasing the catalyst surface area. Thus, a high surface to volume ratio is desired since the reactants usually only interact with the surface of the catalyst.

1.3 Dispersion

In catalysis, it is desirable to have as many active sites available to the reactants as possible. In supported metal catalysts, this is done by depositing nanoparticles on a support in order to increase the surface area of metal. A term called dispersion is commonly used to characterize a catalyst. Dispersion is defined as the percentage of atoms on the surface relative to the total number of atoms in a particle. The equation for dispersion is given as

$$D = N_S/N_T \tag{1.1}$$

where N_S is the number of surface atoms and N_T is the total number of atoms. The surface area and volume occupied by an atom were used to calculate the dispersion of a spherical palladium particle and the effect of particle size on dispersion is shown in Figure 1.2. It can be seen from this correlation that particle size has a dramatic effect on dispersion and that by using small (< 2nm) particles the number of surface atoms (sites available to the reactants) is greatly increased.

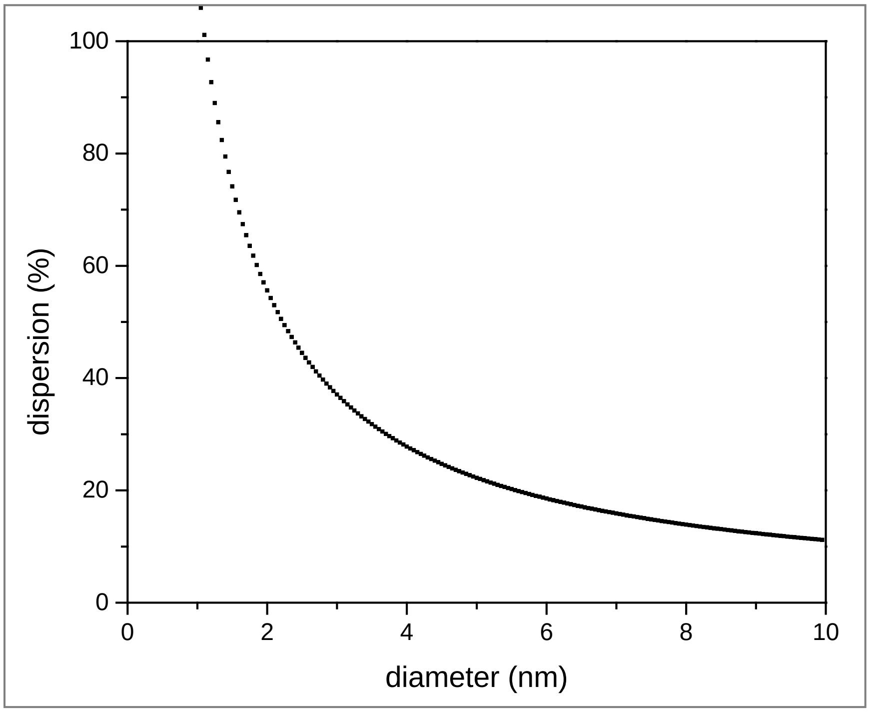

Figure 1.2 Percentage of surface atoms as a function of particle diameter for spherical palladium particles.

There are two challenges when using a highly dispersed metal as a catalyst, the first is synthesizing the small particles and the second is maintaining the high dispersion through the catalysts use.

1.4 Catalyst Synthesis Methods

There are currently many methods used to prepare catalysts. While these methods are widely used both in research and in industry, the dispersion of catalyst particles on the support surface is often not homogeneous, which will affect both the activity and stability of the catalyst. For research purposes, it can often be important to synthesize catalysts having the same particle size (or dispersion) on different supports. This can be difficult to do using aqueous precursors because oxides have different isoelectric points. This is also commonly referred to as the point of zero charge (PZC). This is the pH at which the material doesn’t carry an overall charge. This material property influences the adsorption of metal salts [2] and is illustrated below in Figure 1.3. The figure shows TEM images and particle size distributions (PSDs) of three commonly used catalyst supports with a broad range of PZCs. All three catalysts were prepared using impregnation, described in the following section, and palladium nitrate as the metal precursor. The mean particle diameter ranges from 7.4 to 13.1 nm on the different supports and the effect of PZC can clearly be seen. The PZC is 1.1 and 7.9 for SiO_2 and Al_2O_3, respectively, which influences the resulting particle size for catalysts prepared using incipient wetness impregnation [3]. And in the case of another widely used support, zinc oxide (ZnO), the strongly acidic solutions of a precursor can make it difficult to prepare catalysts without modifying the support morphology [4].

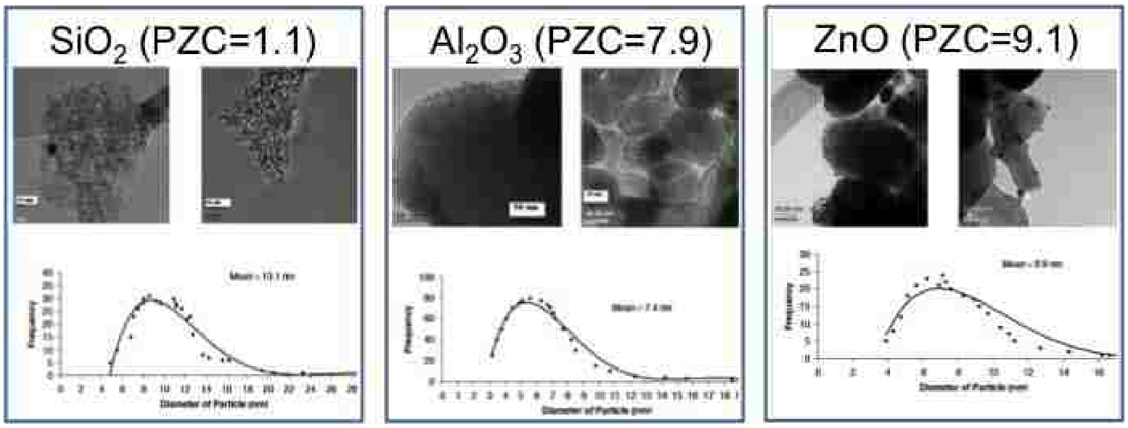

Figure 1.3 TEM images along with corresponding PSDs showing the differences in particle sizes using the same deposition method and different supports.

1.4.1 *Impregnation*

Impregnation is a deposition method in which the pores of a support are filled with an aqueous solution of the metal precursor. The amount of metal deposited on the support is dependent on the solubility of the precursor in the pore filling solution. If the solubility is exceeded, the resulting catalyst usually has large particles and/or a non-homogeneous distribution of particles. This is a fairly simple method but yields low metal weight loadings on the support because of the solubility limit. This limitation often makes it necessary to perform multiple impregnation steps to achieve high loadings, which can be time consuming.

1.4.2 *Deposition-Precipitation*

Another method commonly used is deposition-precipitation. A metal salt is dissolved and the metal is then precipitated out of solution. This is usually accomplished by changing the pH and/or the temperature of the solution, which causes the metal particles to nucleate on the surface of the support. This method requires a strong chemical affinity between the metal and support in order to achieve a homogeneous dispersion [5].

1.4.3 *Colloids*

There are colloidal methods that use ligands and capping agents to generate uniformly sized particles; the size and structure of a particle is inhibited by the ligands. The size and structure of the particles are not influenced by the support since they are formed in its absence. Although this method has been shown to produce mono-dispersed nanoparticles, the ligands or capping agents must be removed as not to interfere with the catalyst activity [6,7]. The removal of the ligands often involves high temperatures and harsh conditions that can cause particle sintering and also adds an extra costly and time consuming step during synthesis. This heat treatment could also influence the support and/or metal support interface having an effect on the selectivity and activity of the catalyst [8,9].

1.4.4 *Alcohol Reduction*

The alcohol reduction method of depositing metal nanoparticles on a support utilizes a metal acetate precursor and uses alcohol as a reducing agent [10]. The rate of nanoparticle formation can differ depending on the alcohol used as the reducing agent. This synthesis method has shown to have the ability to produce similar sized particles on various supports and does not need an oxidization or additional reduction treatment before being active as a catalyst.

1.5 Sintering

The second issue that can affect a catalyst's dispersion is the growth of particles during their use. In the field of catalysis, this growth is often referred to as sintering. Sintering is a considerable problem because this loss of surface area leads deactivation of the catalyst. There are two commonly accepted mechanisms of particle sintering, Ostwald Ripening (OR) and particle migration and coalescence (PMC). Figure 1.4 shows a schematic illustrating the differences between the two sintering mechanisms.

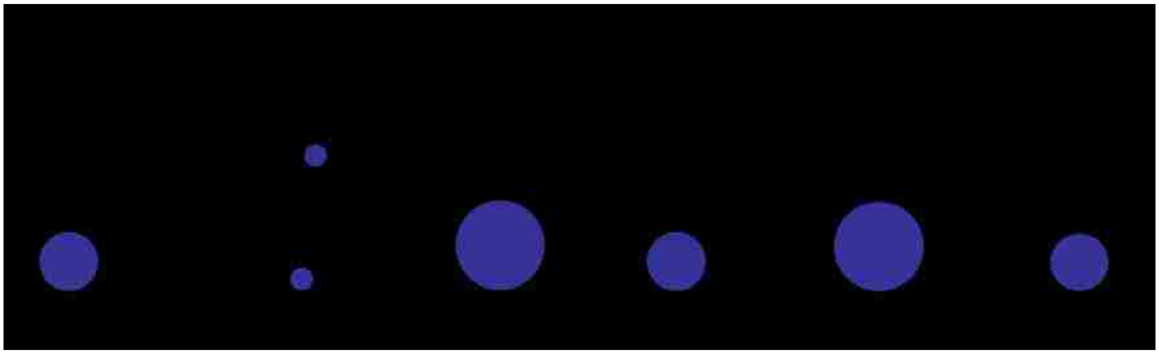

Figure 1.4 Schematic illustrating the differences between the two particle growth mechanisms, Ostwald ripening and coalescence.

1.5.1 *Ostwald Ripening*

OR ripening involves interparticle transport in which atoms are emitted from particles and captured by other particles. The thermodynamic driving force for this process is governed by the Gibbs Thompson relation,

$$\mu = \mu_0 + \frac{2\gamma\Omega}{r} \qquad (1.2)$$

Where μ_0 is the chemical potential of a bulk particle, γ is the surface free energy of the particles, Ω is the atomic volume, and r is the radius of curvature of a particle. The chemical potential of a particle is inversely proportional to its size. The smaller a particle is, the more surface free energy it has and the less stable it is. The instability leads to emission of atoms, which can diffuse along the surface of the support or in the gas phase. These atoms are ultimately captured by the larger particles in the system. This leads to the small particles getting smaller and eventually disappearing and the large particles getting larger. The larger particles grow at the expense of small particles.

Lifshitz and Slyozov [11] and Wagner [12] were the first to develop a kinetic model for Ostwald ripening. Although this work focuses on grain growth during precipitation from a supersaturated solution, the system is analogous to a solid ripening in the gas phase. Chakraverty applied this model to metal particles and thin films and determined the shape of a distribution function [13]. The corresponding particle size distribution (PSD) is shown in Figure 1.5. This PSD is skewed to the left indicating a higher concentration of large particles with a sharp cutoff at about 1.5 times the mean diameter. The supply of small particles continuously decreases and results in a long tail towards the smaller diameters.

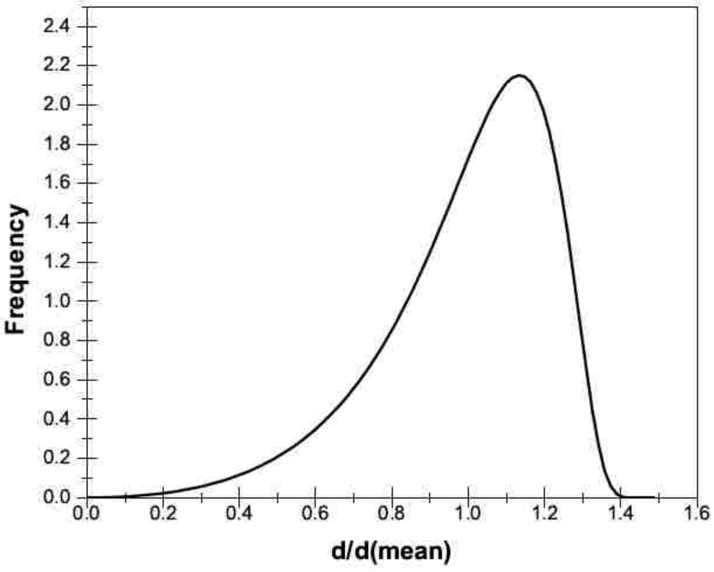

Figure 1.5 Calculated particle size distribution for Ostwald ripening.

1.5.2 *Particle Migration and Coalescence*

In the process of particle migration and coalescence, whole particles move and collide with one another to form larger particles. Adatoms on the surface of particles are in constant flux. As this atomic diffusion takes place, atoms can accumulate on one side of the particle due to random fluctuations. This can cause a shift in the particle's center of mass, which leads to migration. Particle migration is considered to be more likely for small particles with a particle becoming increasing immobile as it grows larger. Some studies have shown that particles as small as a few nanometers in diameter are too large to migrate. As particles migrate along the surface of a support, they collide and coalesce together.

Granqvist and Buhrmann showed that a distribution predicted for PMC corresponds to a log normal distribution which is illustrated in Figure 1.6 [14]. This PSD has a long tail towards the large diameters and no specific cut off for a maximum diameter.

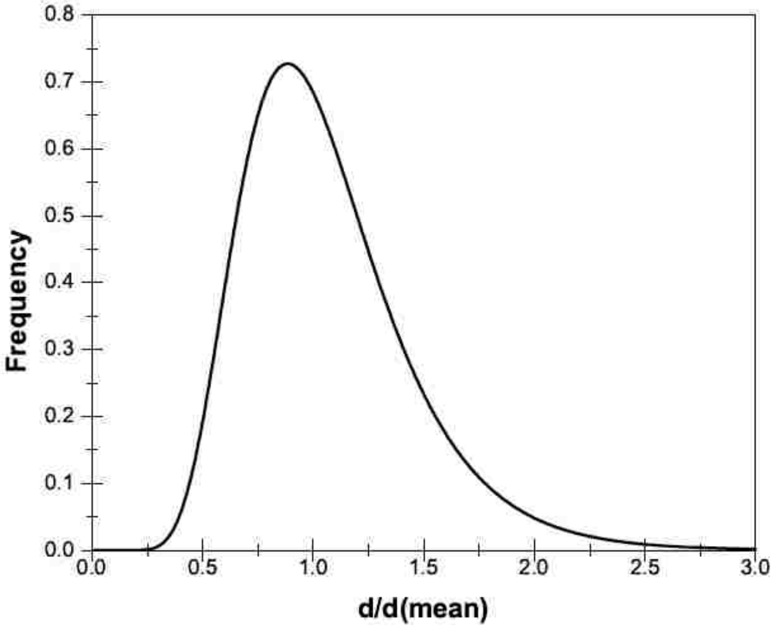

Figure 1.6 Calculated particle size distribution for particle migration and coalescence.

1.6 Support Effects

The function of a support is to allow for the dispersion of the metal in order to increase its active surface area and to prevent agglomeration of the active phase. Initially, a support was thought to be inert and its function purely physical in nature. Works by Schwab and Solymosi were some of the first studies to show that a support could play a role in the activity of a reaction [15,16]. They concluded that this effect was due to an electronic interaction between the metal and the support. These studies also suggested that the effect of the support would be greater, the smaller the particle due to the increased surface interaction.

1.7 From Model Studies to Practical Catalysts

Synthesis methods used for model systems are quite different from those used for practical catalysts. Model systems are most often used to study fundamental properties and are prepared by condensing atoms or aggregates on single crystal or flat supports. Wet chemical methods are often used to prepare practical supported metal catalysts and introduce factors not present in model studies. These factors include things such as impurities and a difference in particle structure and size distribution. There can also be a greater than theoretical binding between the metal and support and a difference in the metal support interactions.

1.8 Control Nucleation to Improve Dispersion

One way to improve dispersion is to control the nucleation sites on a catalyst support. This is illustrated in Figure 1.7. It shows gold nanoparticles on two supports with differing nucleation sites for the particles to bind to on the support. One image shows a silica support with little nucleation sites, which results in a few large gold particles. The other image shows the same silica support with nucleation sites added. This dispersion of the catalyst is quite different than the support with few nucleation sites. The gold particles are much smaller and are dispersed along the surface of the support more evenly.

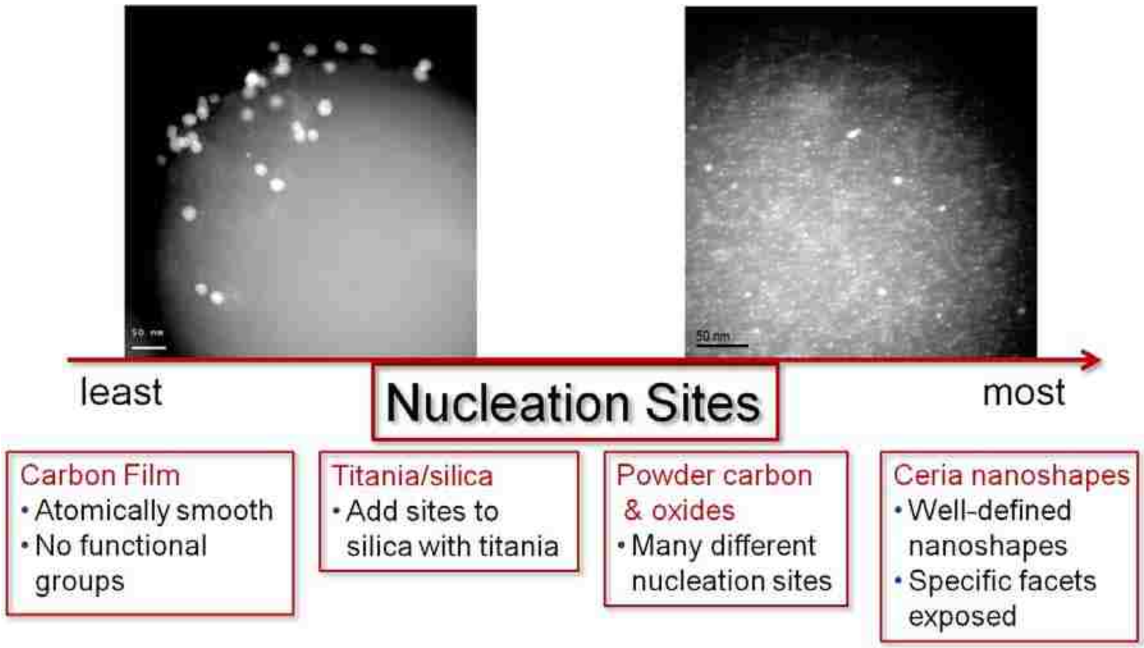

Figure 1.7 Two STEM images showing Au nanoparticles on silica spheres with different amounts of nucleation sites on the support for the particles to bind to. Schematic represents the studies in this dissertation

This dissertation studies several different systems with differing numbers of nucleation sites in order to see how these variations affect the dispersion and ultimately the reactivity of the catalysts.

The first study has the least number of nucleation sites. It uses a carbon film as the support that is atomically smooth and has no functional groups. Using colloidal nanoparticles further minimizes the interaction between the metal particles and the support.

The second study uses silica as a support that typically doesn’t have many nucleation sites. Titania was added to create a mixed oxide support and add nucleation sites to the silica. Both silica and titania were studied independently as supports and neither was found to have the ability to both create and maintain a highly dispersed catalyst. Titania coated on silica was found to greatly improve this and the study optimized the synthesis method to create many nucleation sites which resulted in a stable catalyst.

The next study used powder carbon and metal oxides as a support. Metal particles usually bind to oxides through the hydroxyl groups on the surface. Because of this, it is often difficult to obtain similar dispersions across different supports. This study aimed to use a synthesis method that could take this factor out of play and create similar dispersions on different supports. By doing this, the support effect was isolated and it was found that the support plays a role in the catalyst’s reactivity.

Lastly, the nucleation sites on different facets of the same material were studied. It has been shown that by synthesizing ceria in different nanoshapes, specific crystallographic planes can be exposed. It was found that there was little difference in the metal species deposited on the different ceria nanoshapes. Although the crystallographic face exposed did not seem to play a role in the nucleation of the metal, these catalysts showed a difference in reactivity.

2. ETEM study of the origins of anomalous particle size distributions in supported metal catalysts

2.1 Abstract

In this Environmental TEM (ETEM) study, the growth patterns of uniform distributions of nanoparticles using model catalysts were examined. Pd/carbon was heated in vacuum at 500°C and in 300 Pa of 5% H_2 in Argon at temperatures up to 600°C. Individual nanoparticles of Pd were tracked to determine the operative sintering mechanisms. Anomalous growth of nanoparticles occurred during the early stages of catalyst sintering wherein some particles started to grow significantly larger than the mean, resulting in a broadening of the particle size distribution. The abundance of the larger particles did not fit the log normal distribution. Sample non-uniformity can be ruled out as a cause for the growth of these large particles, since images were recorded prior to heat treatments. The anomalous growth of these particles may help explain particle size distributions in heterogeneous catalysts that often show particles that are significantly larger than the mean, resulting in a long tail to the right. It has been suggested previously that particle migration and coalescence could be the likely cause for such broad size distributions. We did not detect any migration of nanoparticles leading to coalescence. A directed migration process was seen to occur at elevated temperatures for Pd/carbon under H_2. This study shows that anomalous growth of nanoparticles can occur under conditions where Ostwald ripening is the primary sintering mechanism.

2.2 Introduction

When heterogeneous catalysts are subjected to reaction environments at elevated temperatures there is a growth in particle size and the particle size distributions (PSD) usually show a long tail to the right, i.e. particles that are significantly larger than the mean [17-20]. Some examples from previous work include the particle size distributions for Ni steam reforming catalysts aged at temperatures from 500°C - 750°C [18,21], for Pd automotive catalysts aged at 900°C [19] and in Pd combustion catalysts aged at 1000°C [17] all of whom show particles significantly larger than the mean, often 5–10 times larger. It is often speculated that particle migration (PM) could lead to coalescence and the formation of such large nanoparticles (NP) [14,21], however previous studies have concluded that only particles smaller than approximately 6 nm in size could likely show sufficient mobility to lead to coalescence [22]. There are only a few direct observations of particle mobility [23] and recent work by STM suggests that even particles smaller than 1 nm get pinned to the oxide surface and are rendered immobile [24]. On the other hand the largest particles observed in previous studies of industrial catalysts were of the order of 100 nm in diameter or even larger [19,25]. The origin of such large particles in industrially relevant catalysts aged at high temperatures is rather puzzling if particle migration is an unlikely mechanism for the growth of such large particles. The other accepted mechanism for particle growth is Ostwald ripening (OR), which involves inter-particle transport of atomic species.

The classical mathematical model for OR predicts that the largest particles formed should only be 1.5 times as large as the mean size [26]. It was later suggested that a simple modification of the equations used to model OR could result in altered size distributions [27]. Some of these PSDs resulting from the OR formalism also resemble the log normal distribution [28]. It is therefore of interest to determine if the larger particles seen in the experimentally determined PSDs are consistent with the models proposed in the literature [27,28]. The formation of abnormally large particles in industrial catalysts has major economic consequences since large particles consume a lot of the precious metal in a catalyst but provide very little reactivity. Most of the surface area in a catalyst comes from small particles, which have high surface area per unit of mass. To achieve the desired level of long-term performance and overcome the loss of metal surface area by sintering, catalyst manufacturers often resort to increased loading of the precious metal in industrial catalysts. With increasing cost of precious metals like Pt and Pd, there is a need to improve our understanding of growth patterns for nanoparticles in supported catalysts.

One complication when working with catalysts prepared on an industrial scale is the uniformity of the initial catalyst precursor. It has been speculated that the large particles observed in the industrial catalysts could arise from non-uniform distributions of the catalyst precursor. This initial distribution of precursor could result in locally high concentrations of metal in certain regions of the catalyst, and lead to abnormally large particles after catalyst ageing. In industrial catalysts, it is difficult to image via microscopy the same region of a catalyst before and after a long term treatment. Therefore many studies have used model catalysts that start out with a uniform distribution of metal particles. The published PSDs when model catalysts were heated to elevated temperature also show the presence of anomalously large particles. For example, in their comprehensive review of supported metal catalysts, Wynblatt and

Gjostein [26] report that anomalously large particles were seen in a model catalyst system consisting of Pt particles on a microcrystalline γ-Al_2O_3 film (100 Å thick). These authors proposed that the growth of the metal particles was related to evaporation of Pt in an O_2 containing atmosphere leading to volatile PtO_2 as the mobile species. Their observations were done at 700-1000°C in a quartz tube with either air or 2% O_2 in N_2 at atmospheric pressure. It was found that higher O_2 partial pressure led to faster particle growth and they attributed the abnormally large particles to a morphological instability whose details were not elucidated in their experiments. They speculated that there was a change in growth mode resulting from differences in the structure of the particles. 'Normal' growth patterns for the first 7 hours of sintering were followed by 'abnormal growth' resulting in some particles growing considerably faster than average [29]. The abnormal growth rates led to an inflection point in a plot of mean radius as a function of time, but the precise location of the inflection depended on temperature and oxygen partial pressure. The growth patterns were modeled using power law growth models with different values of the exponent but without any mechanistic insight [30]. The emergence of the anomalously large particles could not be explained, but the authors did speculate that the particles that started to grow large were initially twinned particles whereas all other particles were single crystals.

Harris et al. [31,32] observed similar phenomena (growth of abnormally large particles) on model samples of Pt/Al_2O_3 heated to 600°C-700°C in air at atmospheric pressure for up to 8 hours. Like the previous work by Wynblatt and Gjostein [26], Harris et al. [31,32] also concluded that the abnormal growth patterns appeared at the later stages of catalyst sintering. The large particles that resulted were often observed to be highly faceted with hexagonal or triangular outlines. The authors conjectured that small particles would sinter via PM while larger particles would be virtually immobile and grow only via OR [22]. Hence, they argued that the phenomenon of abnormal growth was difficult to explain by PM and suggested that twinning of some particles might cause the generation of reentrant surfaces facilitating growth by interparticle transport. Since Pt is known to form a volatile oxide PtO_2, it is possible that vapor phase processes may also play a role. However, observations of abnormal growth are not confined only to Pt catalysts under oxidizing conditions since similar observations were reported for Ni/SiO_2 heated in H_2 and N_2 at temperatures ranging from 500-800°C [33]. The data was fit to a power law and it was inferred that the drastic changes in the fitting exponent indicated a change in mechanism from PM to OR. The PSDs show anomalously large particles in sample sintered at 800°C. Kim and Ihm [34] observed similar anomalously large particles for a Ni/Al_2O_3 model catalyst system after heating to 800°C in H_2 atmosphere for 43 hours.

The literature on catalyst sintering shows that the mechanism of the formation of large particles, and the long tail in the PSD, are still poorly understood. There is uncertainty about the importance of PM versus OR as mechanisms responsible for the growth of metal particles. With recent advancements in the technique of *in situ* TEM, it is now possible to study smaller particles (which would be more likely to undergo PM) and to expose the catalyst different atmospheres in the microscope. We decided to explore the growth patterns of Pd nanoparticles that were most likely to undergo PM (by using a non-interacting support such as carbon). Pd was studied in vacuum and under reducing conditions. Nanoparticles were prepared by via colloidal routes (leading to weak interactions with the support). Continuous observations of Pd allowed us to infer the mechanisms of particle growth. Since the samples were examined before and after heat treatment, we ensured that there were no locally high concentrations of metal that could lead to anomalous growth patterns. The term locally high concentrations is meant to indicate the type of non-uniformities seen in supported catalysts where excess catalyst precursor may lead to higher coverage of the metal in some parts of the catalyst sample. The specific objectives of this work were to determine if abnormal growth patterns were prevalent in the early stages of catalyst sintering and whether the origins of the formation of larger particles could be identified. A secondary objective was to determine the mechanism of particle growth and its influence on the formation of a long tail in the PSD. The surprising observation in this work is that abnormally large particles could be observed even under conditions where the particle growth occurred exclusively through interparticle transport of atomic species via OR, and that PM did not occur, even with the particles that were most weakly held on the support.

2.3 Experimental Methods

2.3.1 *Synthesis of Pd nanoparticles*

The Pd nanoparticles were synthesized by the reduction of Pd acetate with methanol based on the approach described by Burton et al. [10]. Specifically, 11.2 mg Pd acetate (Sigma-Aldrich, recrystallized in the lab using glacial acetic acid) was dissolved in 1 mL anhydrous toluene (Sigma-Aldrich) followed by the addition of 16.4 µL oleylamine (1:1 oleyalmine:Pd, molar ratio) used as the capping agent. The solution was degassed using ultra high purity Ar (20 mL/min) for 20 minutes to remove any dissolved

O_2. Similarly, anhydrous methanol (Sigma-Aldrich) was also degassed and then added to the Pd acetate/oleylamine in toluene solution at 1:1, volume:volume, ratio to get a final concentration of 25 mM Pd acetate. The Pd was reduced by heating the solution at 60°C (under a stagnant Ar atmosphere) on a hot plate for 30 minutes. The solution color changed from dark yellow to black. This method allowed us to create a stable suspension of Pd NPs with a mean diameter of 3 nm.

2.3.2 *In situ Transmission Electron Microscopy*

The colloidal solution was diluted 200:1 with toluene and a drop of the diluted solution was deposited on a Protochips Aduro™ TEM holder. The Aduro™ heating holder consists of a carbon film deposited on a Si MEMS device that can be heated rapidly via resistive heating. The sample was mounted in an aberration corrected FEI Titan ETEM G2, and all imaging was performed at the accelerating voltage of 300kV, and reduced electron dose rate of approximately 0.15-0.3 A/cm^2 to minimize electron beam induced effects. Under the imaging conditions used, there was no change in the size or distribution of nanoparticles at room temperature. To further minimize any electron beam induced effects, the beam was blanked during prolonged experiments, and the majority of the observations reported here occurred in an "interrupted heating cycle" mode. That is, the observations were made at room temperature after the sample was heated to or above 500°C for a preset period of time. Due to the rapid heating/cooling rates and very low drift rates associated with the Aduro™ heating holder, observations of multiple areas of interest could be performed almost instantly. The temperature of 500°C was chosen since it represents the approximate onset of sintering for Pd NPs. The majority of the experiments were performed in vacuum at the base pressure of ~10^{-5} Pascal, one additional set of experiments involved heating the sample in 5% H_2 in Argon at the pressure of approximately 300Pa.

2.4 Results

2.4.1 *Aging of Pd/carbon in vacuum*

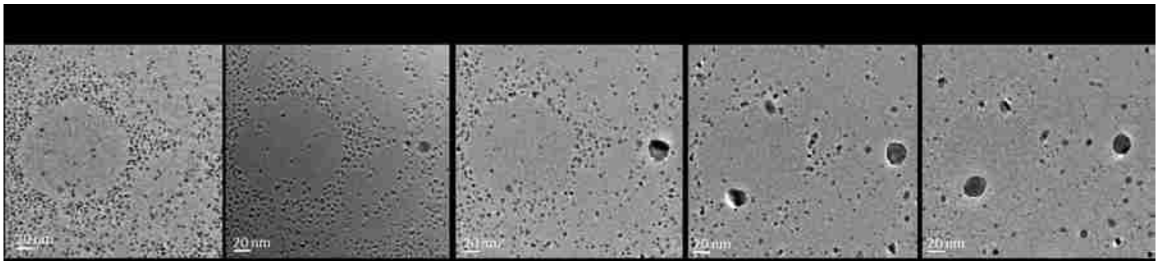

Figure 2.1 Palladium nanoparticles supported on a carbon film imaged in vacuum at 500°C. The images were acquired after 0, 2, 20, 25, and 30 minutes of heating, respectively. The series of images capture the anomalous growth large particles
.

Figure 2.1 shows images after 0, 2, 20, 25, and 30 minutes, respectively, after heating to 500°C in vacuum. The figure illustrates the growth of palladium particles under these conditions. By carefully monitoring the positions of the particles, it was concluded that there was very little movement of the particles. What is most striking is the growth of a few anomalously large particles. Before the heat treatments (0 min), the regions where anomalous growth was observed do not show particularly high density of particles and instead have a fairly uniform distribution of similarly sized particles. In Figure 2.1, 853 particles were counted at time 0. The number of particles in this region decreased with time and 234 particles remained after 30 minutes of heating. Figure 2.2 shows the particle size distributions corresponding to the images in Figure 2.1. Initially, there is a narrow particle size distribution that broadens shifts slightly to the right after 2 minutes of heating.

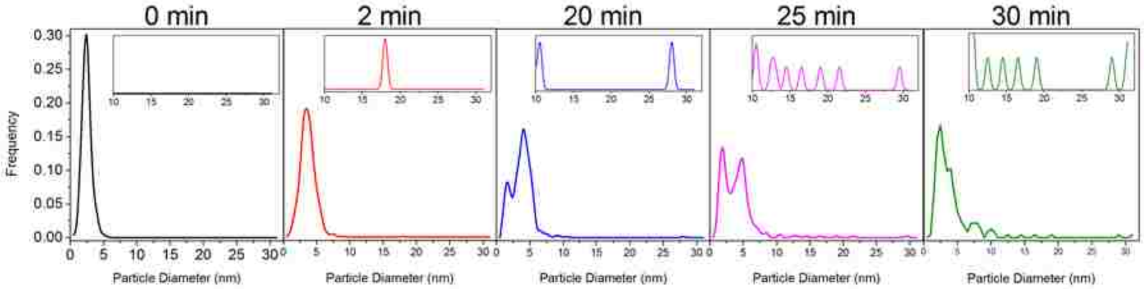

Figure 2.2 PSDs corresponding to images in Figure 2.1. The distributions show an appearance of the particle size bimodality after heating Pd NPs at 500°C in vacuum. The bin size is 0.5 nm.

After 20 minutes of heating, the size distribution becomes bimodal and some of the particles observed earlier have decreased in size. This is clear evidence that the primary sintering mechanism is Ostwald ripening and not coalescence. The bimodal size distribution becomes more prominent after 25 minutes of heating and then becomes less noticeable after 30 minutes of heating. After 30 minutes of heating, there are still many small particles (<5nm) and several large particles (>10nm). Figure 2.3a and 2.3b show the same region of the sample imaged in Figure 2.1 after 2 and 20 minutes of heating, respectively. A region of this image was magnified and is shown as Fig. 2.3c and 2.3d. In Figure 2.3c each particle is outlined in red to identify its position and size. The outlines marking all the particles were converted into a mask, which was transferred to Figure 2.3d in order to see clearly the changes that occur after heating the sample.

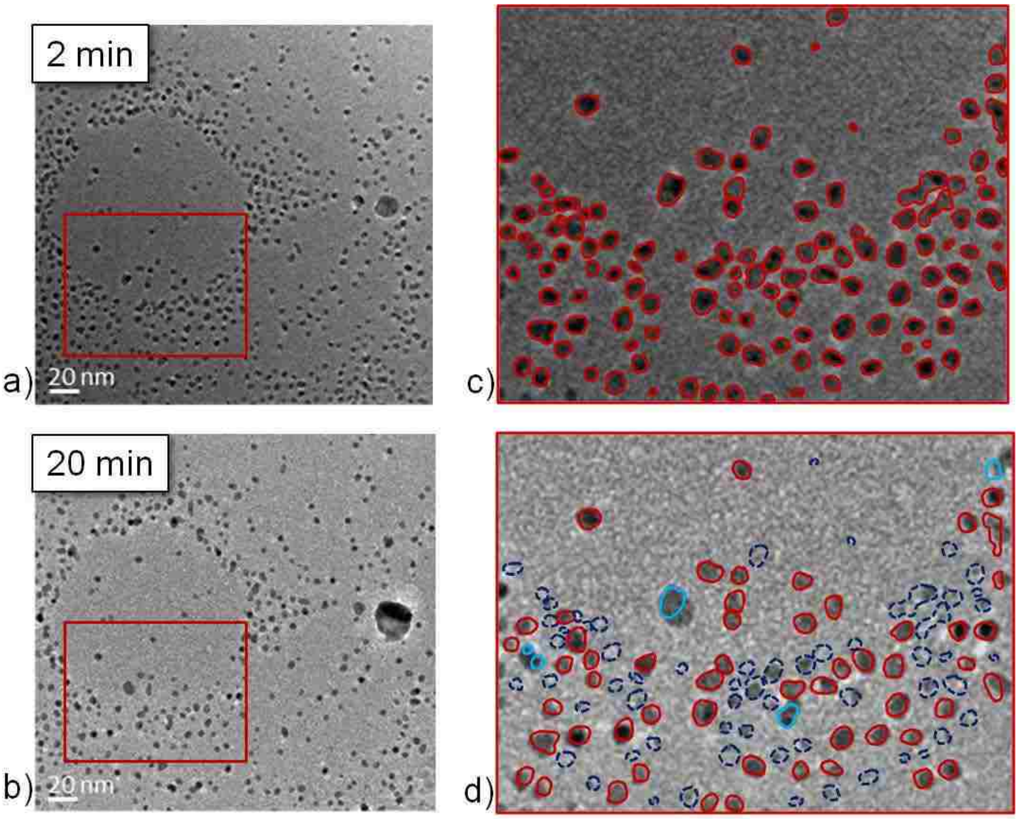

Figure 2.3 Images a) and b) correspond to images in Figure 2.1 after 2 and 20 minutes of heating, respectively. Images c) and d) are higher magnifications of the areas shown in the red boxes. An outline of the particles in image c) is shown in red. This mask was transferred to image d) to show how these particles changed over time. The outline is changed to light blue where particles grew and is retained red for particles that had no change. The outline is dashed dark blue for particles that shrunk or disappeared.

Where the particles grew in size, the mask color was changed to light blue. Where the particles decreased in size or disappeared, the mask color was changed to dashed dark blue. For particles that had little or no apparent change the mask color was retained and is shown in red. This makes it easy to see that while there are changes in size, none of the particles have moved. In addition to the particles being immobile, some particles are increasing in size and there are many particles that have shrunk in size, hence the mechanism is clearly OR. This figure also illustrates that the particles that are growing in size are in the immediate vicinity of particles that are neither migrating nor shrinking in size. The same sample region was further observed for 10 more minutes as shown in

Figure 2.4. Here a new mask is generated for each image so as to show incremental changes. The particles that started to grow larger than their neighbors in the early stages continued to grow in size until they were about 10 times the mean diameter.

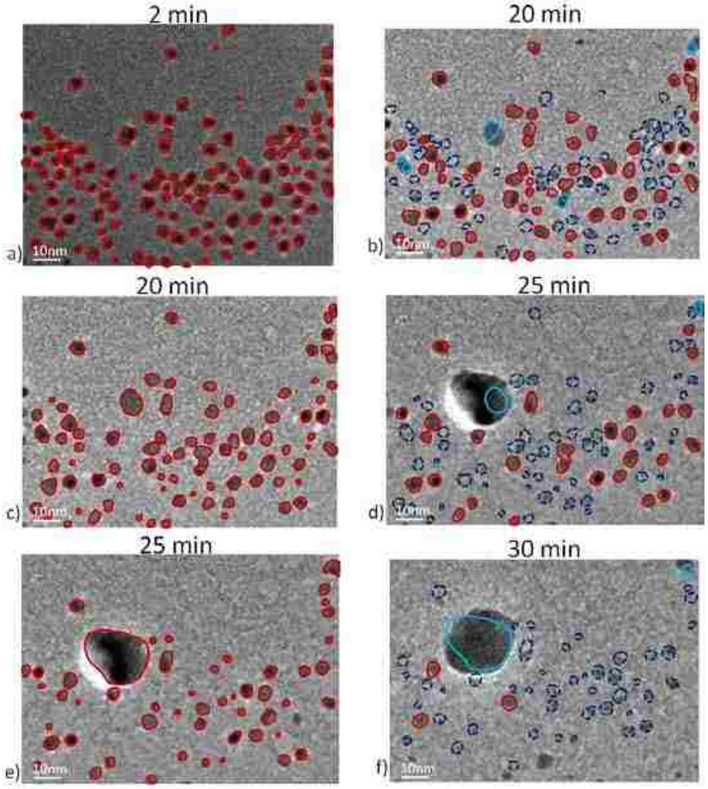

Figure 2.4 These images show the continued evolution of the region shown in Figure 2.3. Images on the left are outlined to mask the particles. Each mask was transferred to the image to its right, which is the next image in the time series. The outline is changed to light blue where particles grew and remained red where particles had no change. The outline is changed to dashed dark blue for particles that shrunk or disappeared. The anomalous growth of one particle can clearly be seen.

The phenomena documented here were confirmed to occur in other regions of the sample. Images from a different region of the sample are shown below in Figures 2.5 and 2.6.

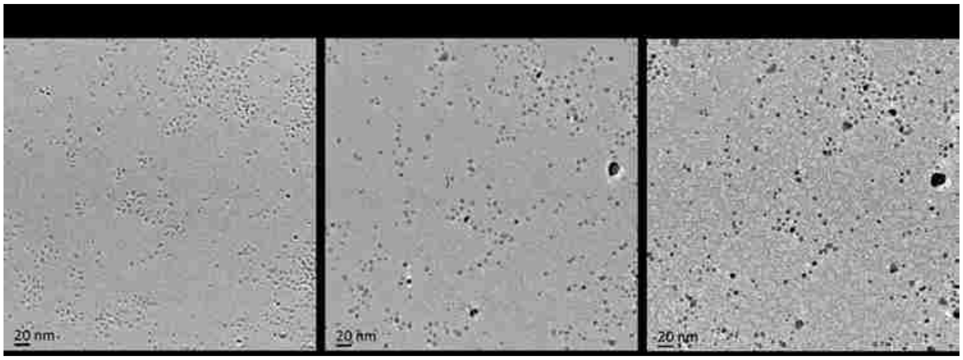

Figure 2.5 Another region of the sample showing palladium nanoparticles supported on a carbon film imaged after successively longer treatments in vacuum at 500°C. The images were acquired after 0, 20, and 30 minutes of heating, respectively. The series of images is included to show how the phenomenon of anomalous growth shown in Figures 2.1-2.4 is widespread across this sample.

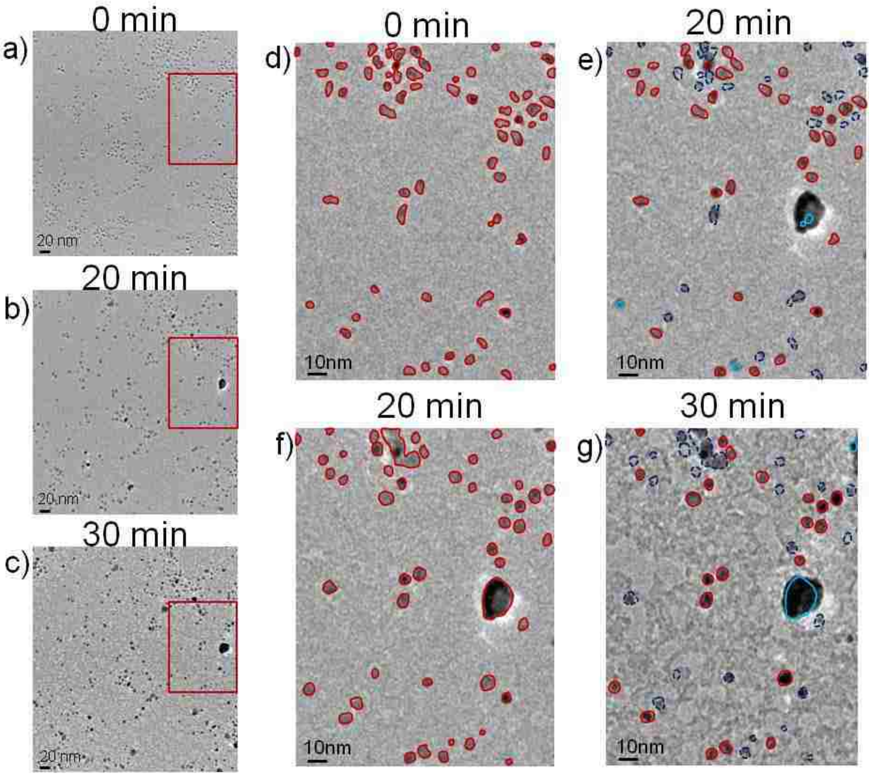

Figure 2.6 Images a), b), and c) are palladium nanoparticles after heating at 500°C in vacuum for 0, 20 and 30 minutes, same images as in Figure 2.5. Images on the right are high magnification views of the areas boxed in red. The particle masks in images d) and f) were transferred to images e) and g), respectively. This highlights the particle size changes over time.

These images show that anomalous growth patterns similar to those documented in Figures 2.1-2.4 occurred elsewhere on this sample. The PSD corresponding to the images in Figure 2.5 is shown in Figure 2.7. This also demonstrates a bimodal distribution as in the previous region shown.

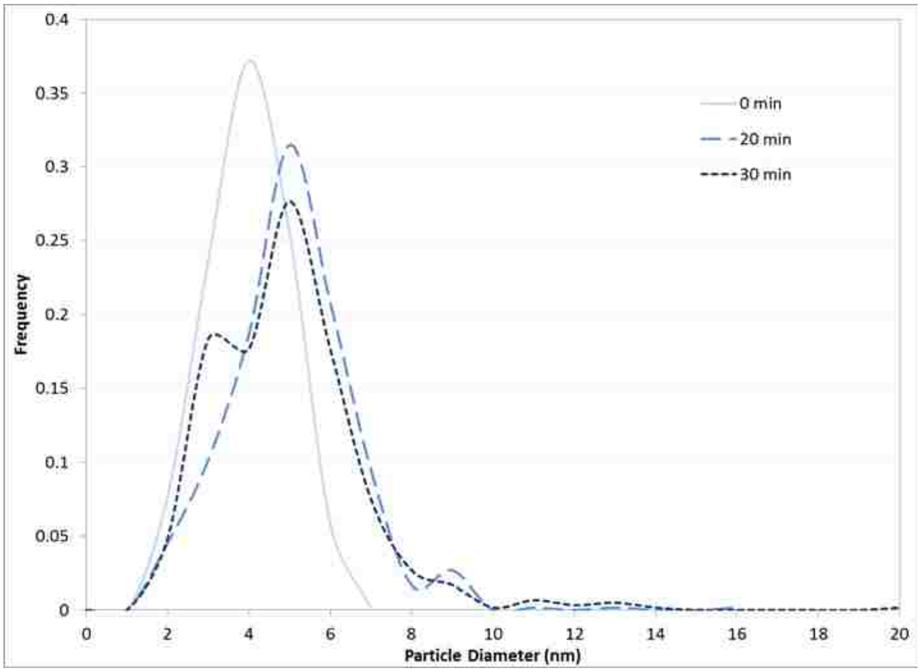

Figure 2.7 Particles size distributions corresponding to images in Figure 2.5. There is an appearance of bimodality in particles sizes after heating at 500°C.

At the end of the heating cycle, sample areas that were not observed at earlier times in the heat treatment sequence were imaged. The overall appearance of the sample in regions not imaged previously (and hence not exposed to the electron beam) was similar to the regions that were repeatedly observed at successive time intervals. Such an image is shown in Figure 2.8 where anomalous growth of particles is seen after 30 minutes of ageing in vacuum.

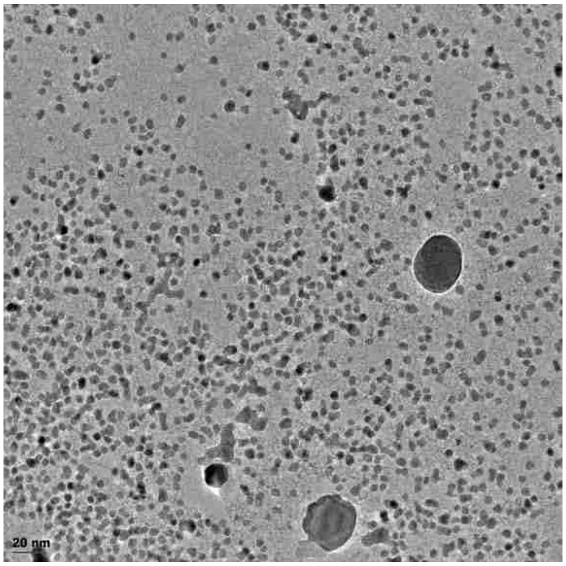

Figure 2.8 Image of a location previously unexposed to the electron beam during the experiment. This image was acquired by moving far away from locations that were previously imaged, to determine how the sample looked in areas not subjected to any electron beam exposure. This sample of palladium nanoparticles on carbon film was heated to 500°C in vacuum for 30 minutes. All of the images observed from regions unexposed to the beam showed similar anomalous particle growth, confirming this is not a beam effect.

Heating the specimen in vacuum for 30 minutes causes some degradation of the carbon film which can be seen in Figure 2.8. The region that was repeatedly exposed to the electron beam for 30 minutes also showed similar changes; see Figures 2.1 and 2.5. The carbon film is starting to disintegrate and shows regions of lighter contrast. Traces of oxygen and moisture may have caused gasification of the carbon. Electron beam exposure may create point defects and further accelerate this oxidation of the carbon film. We did not see any influence of the electron beam on the phenomenon of Ostwald ripening at the beam illuminations used in these experiments.

2.4.2 *Aging of Pd/carbon in H_2*

A second sample of the Pd/carbon was heated in H_2 to study the role of the gas phase environment. This sample was first heated in vacuum at 500°C and anomalous growth patterns were observed that were similar to those described in the previous section. The sample was cooled down and exposed to flowing H_2 at a pressure of 300 Pa (5% H_2 in Argon). Next the sample was heated to 500°C and no further changes in size over the time interval of our observation were found to occur in the presence of H_2. The major changes had already occurred during the heating of the sample in vacuum to 500°C. The sample was then heated to 600°C in the H_2 atmosphere and more rapid transformations in the Pd NPs occurred. One such sequence is shown in Figure 2.9 where adjacent particles form a neck and eventually merge to form a single large particle.

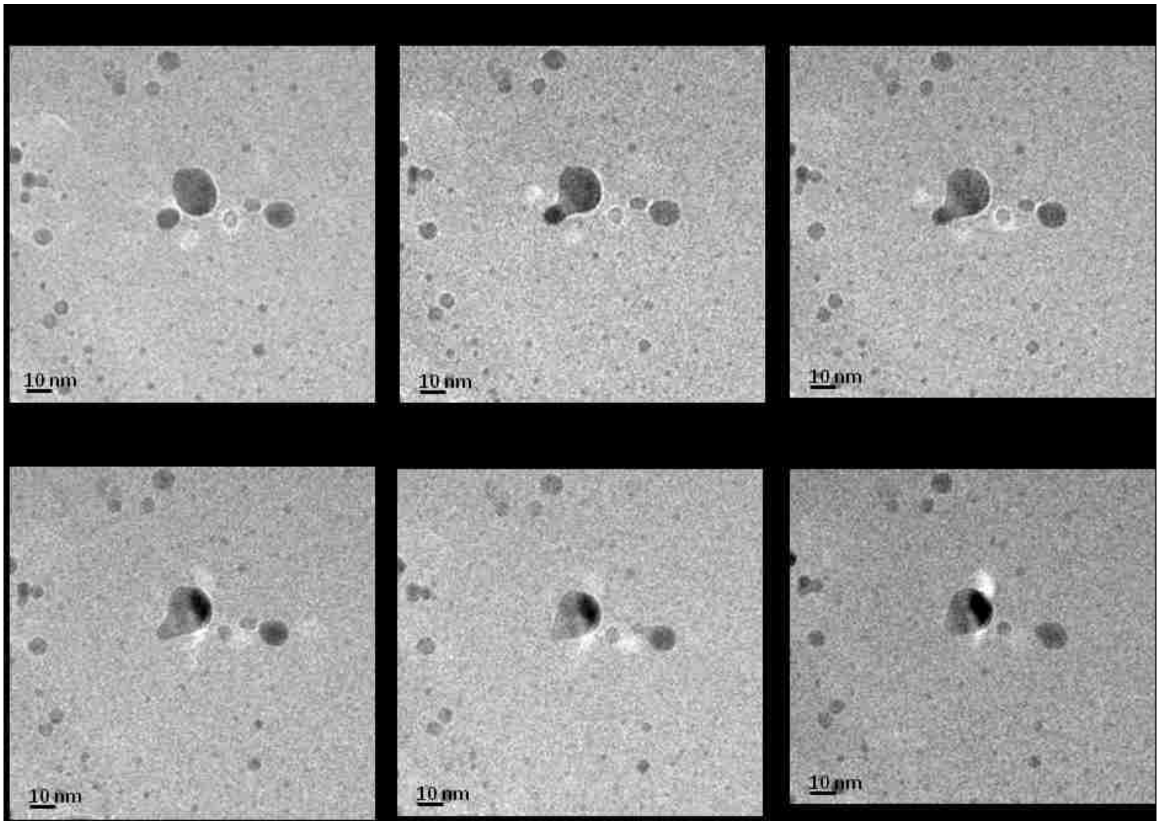

Figure 2.9 Images show a time series of the same region of palladium nanoparticles on a carbon film heated to 600°C in 5% H_2/Ar. The images show the formation of a neck between two large adjacent particles and their eventual coalescence after more than 6 minutes.

The series of images clearly shows that the process of neck formation and that the fusion of two particles is driven by atomic scale migration events. The process repeats itself with two smaller particles adjacent to the large particle in the center of the image. It appears that when particles are in close proximity, they appear to move close to each other and coalesce. The actual process of merging of the particles occurs first by the formation of a neck or bridge, which then fills in via metal atoms migrating to the reentrant surface. The process of coalescence observed at 600°C in H_2 is very similar to that reported by Yang et al. [35] who called it attractive migration and coalescence. This process is caused by the non-uniform surface concentration of metal atoms around the NPs. The image sequence shows clearly that the fusion of these particles is not caused by random migration of the metal particles, rather a directed motion is seen to occur causing the neck formation and eventual fusion of the particles. Further work is needed to investigate the role of gas atmosphere and temperature on the onset of particle fusion.

2.5 Discussion

The model samples presented here are considerably different from the real-world catalysts used in industry, but they provide suitable systems for determining particle size distributions. The samples are uniformly thick and there are no overlapping support features. The carbon substrate has a smooth texture and there is no surface topography or heterogeneity for anchoring metal atoms or nanoparticles. HAADF images of the carbon confirm the uniformity of sample thickness. Industrial catalyst supports consist of spheroidal particles with surface curvature and reentrant surfaces. Crystalline supports such as alumina expose surface facets, and the industrial supports have a much higher degree of surface roughness. The model catalysts are therefore ideal substrates to study the role of particle migration on the sintering of nanoparticles. Furthermore, the same region of the specimen can be observed before and after heat treatment, allowing us to infer mechanistic details. Prior to heat treatments, it was confirmed that the distribution of the metal particles was uniform. This ensures that the observed particle size distributions after heat treatments were not influenced by the initial non-uniformities in the samples as-prepared.

A Pd/carbon sample was studied in two different environments, in vacuum and in the presence of H_2 gas. Our observations show that the metal particles are effectively immobile in either condition, independent of the gas phase, at a temperature up to 500°C. Anomalous growth was evident in each of the samples, wherein some particles start to grow larger than the mean, and continue to do so until they reach sizes as large as ten times the mean diameter. These particles start to grow in regions that are otherwise no different from their neighbors. However, as some particles grow in size, others shrink or disappear, indicating that the process can be explained by atomic scale migration of mobile species emitted from the nanoparticles, i.e. Ostwald ripening. The classical model for OR would predict a sharp cut off at 1.5 times the mean diameter [26]. The modified equations developed more recently suggest that a log normal distribution may also be possible during Ostwald ripening, based on the formalism of the mean field approximation and a linearization of the Gibbs Thompson equation for surface energy [27,28]. Both of these assumptions have been questioned in the context of Ostwald ripening [36,37]. Nonetheless we examined carefully whether the larger particles we observed could be consistent with a log normal distribution. Figure 2.10 corresponds to the PSD in Figure 2.2 after 30 minutes of heating when the anomalous growth is very evident. This data was fit to a lognormal curve and the fit was integrated from bin end to bin beginning to calculate the area under the curve. The total area was normalized to 1 to get a frequency for each bin. This calculated frequency was then multiplied by the total number of particles counted to obtain a prediction for how many particles would be in each bin according to a log normal fit.

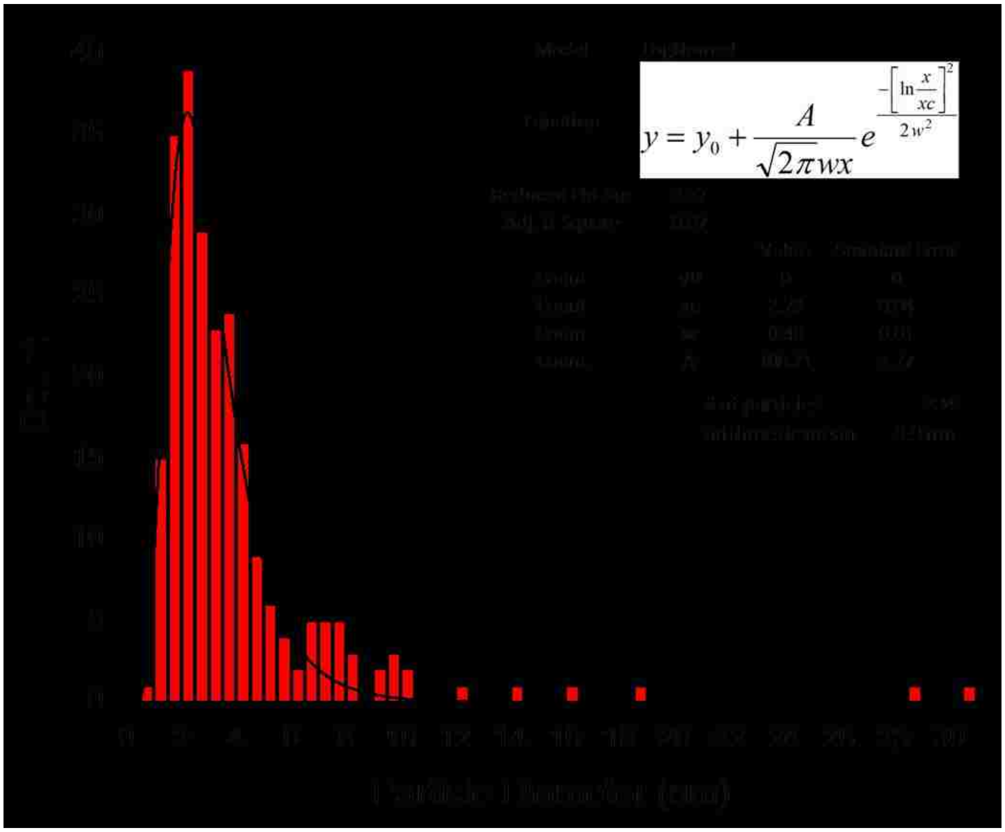

Figure 2.10 PSD corresponding to Figure 2.1 at 30 min. The data has been fit to a log normal distribution. The parameters for the fit are shown in the inset table. The larger particles seen in this image are not consistent with a log normal distribution as shown here and in Table 2.1.

Table 2.1 shows the calculated number of particles according to the log normal fit and the actual number of particles in each bin. The non-zero values are highlighted for ease of visualization. A log normal fit predicts that there will be no particles larger than

8.5nm while on reality, there are 12 particles that are larger that. The largest particle observed, 31 nm, is more than 3.5 times larger than what a log normal distribution predicts. Several other regions of the sample were analyzed in the same manner and fit to log normal distributions. In each case, we found that the abundance of the larger particles far exceeds what would be expected from a log normal distribution. Therefore we conclude that the growth of isolated particles as seen in this work would not be predicted by the classical mean field theory of OR.

Table 2.1 Table showing the probabilities of finding particles in each of the bins in Figure 2.10. The frequency column is the area under the log normal curve normalized to 1. The frequency was multiplied by the number of particles counted in this region (234) to obtain the calculated # of particles which is compared to the actual # of particles counted for each bin. The bins that contain non-zero values for particles are shaded. Comparison of the frequencies for the larger particles shows clearly that the presence of the large particles is unlikely in a log normal fit.

bin	frequency (norm. to 1)	calculated # of particles	actual # of particles	bin	frequency (norm. to 1)	calculated # of particles	actual # of particles
0	[illegible]	0	0	15.5	[illegible]	0	0
0.5	[illegible]	4	0	16	[illegible]	0	0
1	[illegible]	19	1	16.5	[illegible]	0	1
1.5	[illegible]	34	15	17	[illegible]	0	0
2	[illegible]	39	35	17.5	[illegible]	0	0
2.5	[illegible]	35	39	18	[illegible]	0	0
3	[illegible]	29	29	18.5	[illegible]	0	0
3.5	[illegible]	22	23	19	[illegible]	0	1
4	[illegible]	16	24	19.5	[illegible]	0	0
4.5	[illegible]	11	16	20	[illegible]	0	0
5	[illegible]	8	9	20.5	[illegible]	0	0
5.5	[illegible]	5	6	21	[illegible]	0	0
6	[illegible]	4	4	21.5	[illegible]	0	0
6.5	[illegible]	3	2	22	[illegible]	0	0
7	[illegible]	2	5	22.5	[illegible]	0	0
7.5	[illegible]	1	5	23	[illegible]	0	0
8	[illegible]	1	5	23.5	[illegible]	0	0
8.5	[illegible]	1	3	24	[illegible]	0	0
9	[illegible]	0	0	24.5	[illegible]	0	0
9.5	[illegible]	0	2	25	[illegible]	0	0
10	[illegible]	0	3	25.5	[illegible]	0	0
10.5	[illegible]	0	2	26	[illegible]	0	0
11	[illegible]	0	0	26.5	[illegible]	0	0
11.5	[illegible]	0	0	27	[illegible]	0	0
12	[illegible]	0	0	27.5	[illegible]	0	0
12.5	[illegible]	0	1	28	[illegible]	0	0
13	[illegible]	0	0	28.5	[illegible]	0	0
13.5	[illegible]	0	0	29	[illegible]	0	1
14	[illegible]	0	0	29.5	[illegible]	0	0
14.5	[illegible]	0	1	30	[illegible]	0	0
15	[illegible]	0	0	30.5	[illegible]	0	0
				31	[illegible]	0	1

The anomalous growth of particles was seen at 500°C for Pd/carbon where no coalescence of particles was detected. We did observe the fusion of neighboring particles when the Pd/carbon sample was heated to 600°C in H_2. In this case, coalescence was initiated by neck formation, and the particles appeared to move closer to each other prior to neck formation. Such directed motion has been suggested to occur due to growth-decay flow of the island edges driven by non-uniform surface concentration around the islands [35]. Images of particles undergoing coalescence (see Figure 2.9) could be misinterpreted as resulting from particle migration, but no migration of individual particles prior to the onset of coalescence was observed, as can be seen from the image sequence of the sample undergoing the fusion process. All of the particle motion was directed motion towards each other when the particles were in close proximity. The results presented here do not fully explain the anomalous growth of nanoparticles, since it was not possible to discern the features that are responsible for this growth pattern. But we can conclude that the process occurs due to migration of atomic species and not due to coalescence of nanoparticles. Further study is needed to fully elucidate this anomalous growth phenomenon that may be responsible for the long tail in the particle size distribution generally seen in heterogeneous catalysts. Factors that need to be considered are the heterogeneity of real catalyst supports and the role of the gas phase and adsorbates. Abnormal grain growth has also been studied in the field of metallurgy which may provide clues to operative mechanisms [38].

This study helps elucidate a phenomenon of great importance to heterogeneous catalysis, the growth of nanoparticles at elevated temperatures. By using model catalysts, we are able to study the evolution of individual nanoparticles and identify the mechanisms of catalyst sintering. Under our conditions, Ostwald ripening is the dominant mechanism and we did not detect any random migration of nanoparticles leading to coalescence. During Ostwald ripening we found anomalous growth patterns that result in some particles growing much faster than their neighbors. The frequency of occurrence of these larger particles does not fit the log normal distribution at short sintering times.

2.6 Conclusions

An ETEM study of Pd/carbon was performed by continuous observation of individual nanoparticles when the catalyst was heated to 500°C and above. Anomalous growth patterns were detected wherein some particles started to grow much larger than their neighbors. The anomalous growth patterns were not caused by migration and coalescence of particles. Rather, we found that coalescence occurred only at elevated temperatures and only when particles were in close proximity. No random migration of particles was detected; the only movement was a directed motion where neighboring particles were attracted to each other leading to neck formation and fusion. The dominant process leading to particle growth was Ostwald ripening. The anomalous growth of nanoparticles cannot be predicted by a mean field theory and must take into account local particle concentrations and the structure of individual nanoparticles. These anomalous growth patterns observed may help explain the long tail in the particle size distributions observed in heterogeneous catalysts. However, we were not able to discern any features that could help us predict which particles would show the anomalous growth patterns, since they occurred in regions that looked very similar to the rest of the sample. We can, however, rule out non-uniform metal loading, or a high concentration of nanoparticles in close proximity, as factors responsible for anomalous growth.

3. The Role of a Mixed Oxide Support on the Sintering of Gold Nanoparticles

3.1 Abstract

In this study, the effect of the morphology of a mixed oxide support on the sintering behavior of gold nanoparticles was investigated. The hydrolysis reaction of titanium isopropoxide was used to vary the morphology of titania coated on silica. This resulting titania/silica mixed oxide was used as a support for gold nanoparticles. These samples are subjected to calcination treatments in air at temperatures up to 700°C. It was found that hydrolyzed titania/silica served as a support for gold nanoparticles that were thermally stable at high temperatures while the non-hydrolyzed titania was not. AFM proved the hydrolyzed titania was twice was rough as the non-hydrolyzed titania. These finding were applied to a powder support, silica Stöber spheres. These powder samples are a bridge between model supports and commercially relevant supports. This study is proof that support morphology on a flat sample can play a role in the sintering of catalysts. This concept was used to make a thermally stable powder catalyst.

3.2 Introduction

Historically gold was thought to be a chemically inert metal that is resistant to corrosion and chemical reactions; because of this it is used for applications that take advantage of these unique properties such as jewelry and electronic components. Gold catalysts prepared by conventional synthesis methods, such as impregnation, are far less active than other noble metals such as platinum or palladium [39]. These gold particles are larger than the highly active platinum or palladium particles so modifications in synthesis methods were made in order to change this [40]. The deposition-precipitation method yielded a highly dispersed gold catalyst and it was found that an otherwise inert metal becomes an active catalyst when present as nanoparticles [39-42]. An example of this dramatic change in catalytic activity is shown in Figure 3.1 [43]. Turn over frequency (TOF) as a function of nanoparticle size for CO oxidation is at a maximum when particles are between about 2 and 4 nm in diameter and TOF decreases rapidly with larger particles. Gold can be a highly active catalyst at low temperatures but it is difficult to work with as this is only true in a very narrow size range.

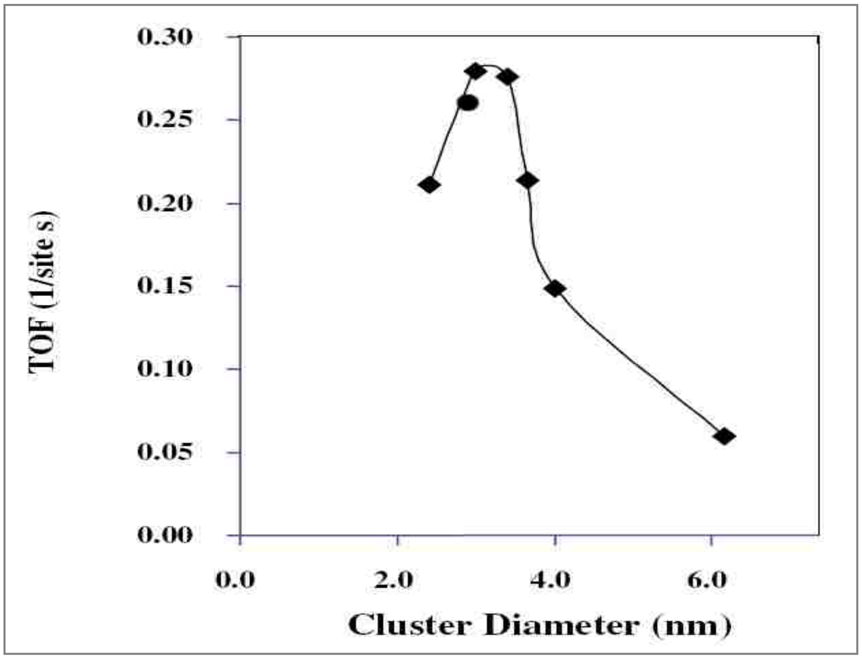

Figure 3.1 TOF for CO oxidation as a function of gold cluster diameter indicating that gold is much more active when in the size range of 2-4 nm [43].

One drawback to using gold as a catalyst is synthesizing nanoparticles in this narrowly active size range. And another challenge is maintaining this size range. The growth of catalyst particles during reaction conditions and at elevated temperatures is commonly referred to as sintering. This particle growth leads to a decrease in surface area and a loss of catalytic activity. Most catalytically active metals suffer from this same phenomenon but the problem is more severe for gold. Gold has a much lower melting temperature than Pd or Pt, which causes it to have a high vapor pressure and sinter at low temperatures compared to its noble metal counterparts. Due to its increased volatility and its loss of activity when reaching sizes as small as 5 nm, low temperatures can be used to observe sintering for shorter periods of time, making Au a good model system to use for this study.

The type of support can also have an effect on both the creation and stabilization of gold nanoparticles. The interaction between the metallic nanoparticles and the support can have a great effect on the resulting catalyst. A stronger interaction between the metal and support is desired in order for a better dispersed catalyst to be synthesized. Au is also known to be more stable on some supports than on others. Due to weak binding between Au and silica (SiO_2), synthesis of highly dispersed particles using this combination of metal and support is difficult to achieve. This is illustrated in Figure 3.2a where gold deposition was attempted on SiO_2 spheres. Because of the weak binding between the gold and SiO_2, there were few sites for the gold to bind to and only a few large particles were deposited, which would not make for a good catalyst. Because Au has a much higher affinity for TiO_2, the same deposition method yields a highly dispersed catalyst as can be seen in Figure 3.2b.

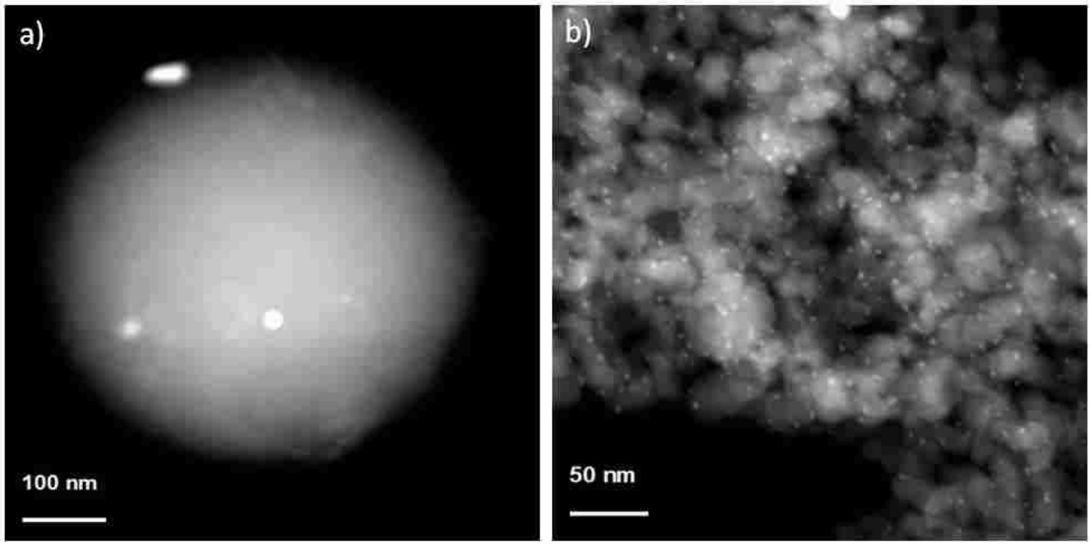

Figure 3.2 a) Gold deposited on silica Stöber spheres. Weak binding between the metal and support lead to large agglomerates of gold. b) Gold deposited on titania. Gold's higher affinity for titania leads to a highly dispersed catalyst.

Although highly dispersed gold can be obtained on TiO_2, it sinters readily at an elevated temperature, which is an indication of what would happen to the catalyst under reaction conditions. Wallace et al. determined that Au was thermally stable on a mixed oxide support such as TiO_2/SiO_2 [44]. An optimum amount of TiO_2 on SiO_2/Mo single crystal served as a support for stabilizing Au nanoparticles when exposed to high temperatures and reactions. Although this effect has been reproducible, the nature of the support was not fully understood. More research in this area is required in order to apply mixed oxide supports to a more practical Au catalyst. While these observations suggest that it is possible to make a stable Au catalyst in certain instances, a fundamental understanding of this phenomenon is needed. More insight into the characteristics of the support and their interaction with the metallic particles is needed.

This study's approach to understanding the stability of Au nanoparticles was to vary a mixed oxide support in a very systematic fashion to determine how small variations effect Au sintering at elevated temperatures. The first step was to synthesize well-defined TiO_2/SiO_2 supports using wet chemical deposition techniques. Gold was deposited on the varying supports and particle size distributions were monitored by analyzing electron microscopy images before and after ageing treatments in air at various temperatures. It was found that creating a rougher TiO_2 morphology allowed for decreased sintering of Au at temperatures as high as 700°C. This understanding was then used for similar synthesis techniques to create a stable Au catalyst on a mixed oxide powder support that is a step closer to a more practical catalyst.

3.3 Experimental Details

3.3.1 *Catalyst Preparation*

TiO_2 Deposition on flat SiO_2

Samples were prepared on 5 x 5 mm SiO_2 wafers obtained from Pella. The wafers were calcined at 750°C for 2 hours in air to create a surface oxide layer. TiO_2 was deposited on the wafer using titanium (IV) isopropoxide (Sigma-Aldrich, 99.999% trace metals basis) as a precursor. 14mL of methanol was stirred with 40mL of toluene for 10 minutes before 1.5mL of titanium isopropoxide was added. The solution was stirred for 10 minutes before the SiO_2 wafers were added and left in the solution overnight. The wafers were removed from the solution and rinsed with methanol and then DI water. They were dried at 125°C for 5 hours in air. The Ti isopropoxide hydrolyzes when it comes into contact with water and begins to polymerize to form a gel. This was taken advantage of in order to vary the morphology of the support. There are two sets of samples prepared in slightly different ways. The first set, which will be referred to as $Au/TiO_2/SiO_2$ wafer (dry), was prepared in a fume hood where no water was added during the TiO_2 deposition step which limited the hydrolysis reaction. During the preparation of the second set of samples, 50µL of DI water was added to the titanium isopropoxide solution during the TiO_2 deposition, which allowed for more hydrolysis to take place than in the previous set of samples. This sample will be referred to as $Au/TiO_2/SiO_2$ wafer (wet).

Gold Deposition

Au nanoparticles were deposited on the TiO_2/SiO_2 wafers using the deposition-precipitation method. Gold(III) chloride hydrate (Sigma-Aldrich, 99.999% trace metals basis) was dissolved in DI water and the pH of the solution was adjusted to 8 by adding sodium hydroxide (NaOH) dropwise. The support was then added to the Au solution and left for several hours. The support was removed from the solution and then washed with DI water and reduced in 3% H_2/N_2 for 2 hours at 200°C at a ramp rate of 0.73°C/ min to remove the surface chloride left behind by the Au precursor.

Synthesis of powder supports

SiO_2 for powder samples were prepared via the Stöber process [45]. 100 mL of tetraethylorthosilicate (TEOS), 14.4 mL of DI water, 100 mL of ethanol and 27.3 mL of ammonium hydroxide were mixed in a beaker and stirred for 2 hrs. The solution was then filtered, washed with ethanol and DI water, and allowed to dry overnight. Titania and gold deposition were performed via the same processes described above for the flat samples except that the powders were washed and filtered between steps.

WGC reference sample

Gold nanoparticles have been notoriously difficult to reproduce in terms of size distribution, so the World Gold Council (WGC) has standardized the synthesis and provides researchers with supported gold nanoparticles to ensure that there is a standard. The sample used as a reference in this study was obtained from the WGC and consisted of Au nanoparticles supported on Degussa P25 TiO_2.

3.3.2 *Ageing Treatments*

Calcination treatments were performed in a tube furnace in flowing air at 400°C and 700°C for 2 hours at a time.

3.3.3 *Electron Microscopy*

The wafer samples were examined by scanning electron microscopy (SEM) in a Hitachi S-5200 at 10 or 20 kV. The images were imported into DigitalMicrograph for analysis. The particles were measured and counted through a built in particle analysis script in the software. The particle sizes were binned and plotted to get the shown particle size distributions. Scanning transmission electron microscopy (STEM) experiments were performed in a JEOL-2010F at 200kV. All image analysis and particle counting was done in DigitalMicrograph™. Due to low contrast difference between the particles and support in STEM images, particles were counted by hand using a Measure Features script from the DM-script-database [46].

3.3.4 *Atomic Force Microscopy*

Imaging was performed using a Nanoscope IIIa atomic force microscope (AFM) in tapping mode under a constant flow of dry N_2 gas using a rectangular silicon cantilever with a spring constant of 40 N/m (Veeco model RTESPA-W). Standard Veeco imaging software (Nanoscope V531r1(17)) was used to capture and analyze the images.

3.4 Results

3.4.1 *Electron Microscopy*

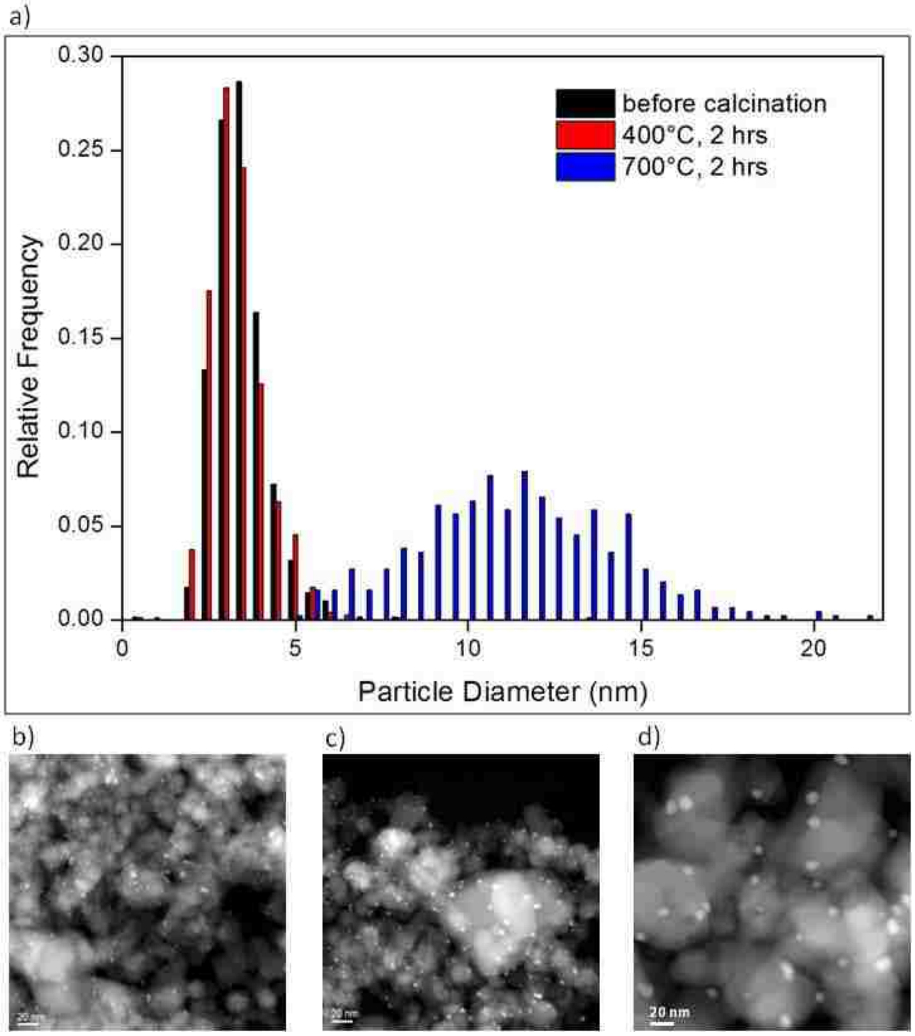

Figure 3.3 WGC sample (Au/TiO_2(P25)) a) PSDs before and after calcination treatment, b) STEM image of freshly reduced catalyst, c) STEM image after 400°C calcination in air for 2 hrs, d) STEM image after 700°C calcination in air for 2 hrs

It was discussed in the introduction that a highly dispersed catalyst could not be synthesized on a SiO_2 support but it could on a TiO_2 support. In order to demonstrate lack of stability on TiO_2, a Au/TiO_2 (Degussa P-25) sample obtained from the WGC was subjected to the same calcinations treatments as the synthesized samples. We used this as a reference to show that under the calcination conditions used for this study, gold nanoparticles would sinter significantly on a commonly used TiO_2 support. STEM images and corresponding particle size distributions are shown in Figure 3.3. Figure 3.3b is the freshly reduced catalyst where the bright spots are gold particles. Images 3.3c and 3.3d are after calcination treatments in air for 2 hours at 400°C and 700°C, respectively. After 2 hours at 400°C, the particles were relatively unchanged but after a subsequent treatment for 2 hours at 700°C the average particle size grew to >10nm and the distribution became much broader containing particles larger than 20 nm in diameter. This is proof that Au nanoparticles on TiO_2 by itself are not thermally stable.

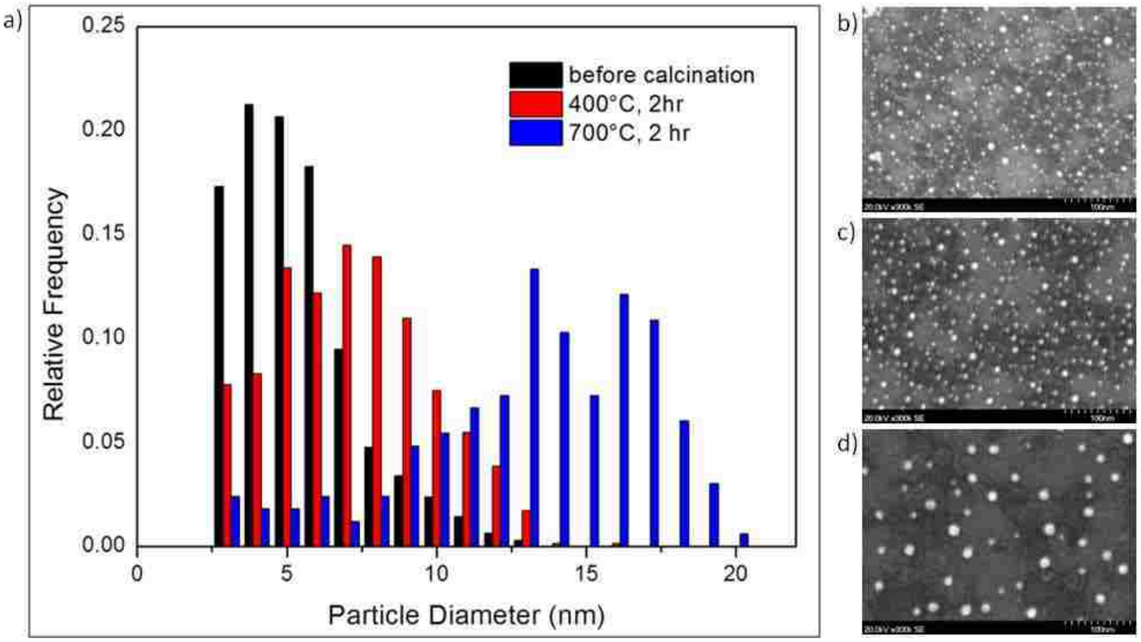

Figure 3.4 Au/TiO_2/SiO_2 wafer (dry), a) PSDs before and after calcination treatments, b) SEM image of freshly reduced sample , c) SEM image after 400°C calcination in air for 2 hrs, d) SEM image after 700°C calcination in air for 2 hrs.

Figure 3.4 shows SEM images of Au/TiO_2/SiO_2 wafer (dry), freshly reduced and after heat treatments for 2 hours at 400°C and 700°C, respectively. There is some sintering at 400°C but it becomes much more significant at 700°C where the average particle size almost triples. This is very similar to what happened with the reference sample. In contrast, Au/TiO_2/SiO_2 wafer (wet) showed very different sintering behavior when subjected to the same calcinations treatments. The particle size distribution and corresponding SEM images can be seen in Figure 3.5.

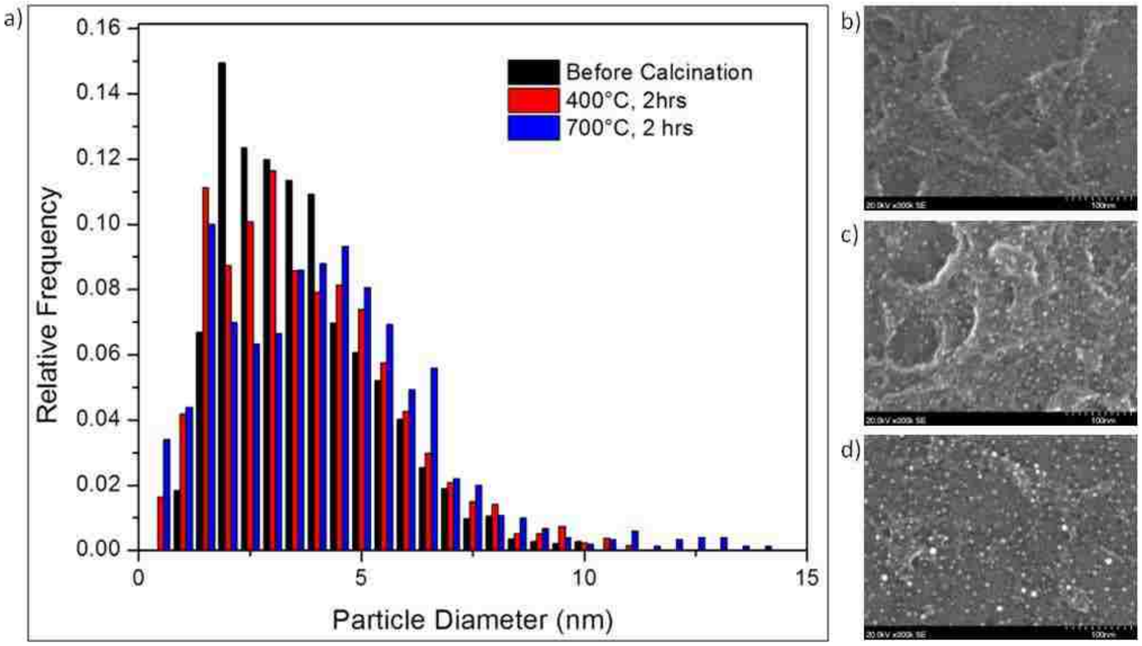

Figure 3.5 Au/TiO_2/SiO_2 wafer (wet), a) PSDs before and after calcination treatments, b) SEM image of freshly reduced sample , c) SEM image after 400°C calcination in air for 2 hrs, d) SEM image after 700°C calcination in air for 2 hrs.

The figure shows the PSD is almost unchanged after the calcinations treatments, some larger particles are formed and the size distribution broadens somewhat but this is a stark contrast to the other samples. It can also be noticed from the SEM images that the morphology of the support is quite different in the two prepared samples. It appears that the difference in TiO_2 hydrolysis resulted in a different morphology of the support. Adding water during the TiO_2 deposition procedure appears to have resulted in a rough surface. Surface roughness is not easily quantified through SEM but it can be much more easily seen through AFM.

3.4.2 *Atomic Force Microscopy*

Atomic force Microscopy (AFM) was used to characterize the difference in surface roughness between the wet and dry samples. Representative AFM images are shown in Figure 3.6 in which an area of $500nm^2$ is shown with a z-height of 5nm. The surface roughness of each sample was taken at several different areas and the average root mean squared for the dry and wet samples is 0.22 nm and 0.45 nm. The wet sample was, on average, twice as rough as the dry sample. The difference in morphology suspected by the SEM images is quantitatively confirmed with AFM.

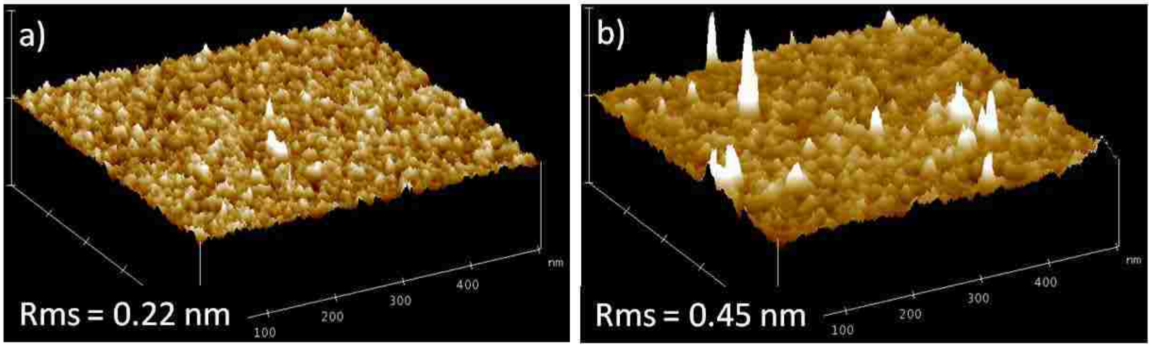

Figure 3.6 AFM images with a z-height of 5nm. a) Au/TiO_2/SiO_2 wafer (dry), b) Au/TiO_2/SiO_2 wafer (wet).

3.4.3 *Powder Samples*

It was seen that with the flat samples that the morphology of the TiO_2 on the SiO_2 plays a role in the thermal stability of Au NPs. A rougher TiO_2 surface could easily be manipulated by varying the degree of hydrolysis of the TiO_2 precursor and this rougher surface yielded Au NPs that were more resistant to sintering at temperatures up to 700°C. While this finding was useful in obtaining a fundamental understanding of variables that can affect sintering behavior, flat samples are not practically useful. This same technique was applied to a powder sample to see if the same concept still applied. SiO_2 Stöber spheres were used as the base for the support. The Stöber spheres on average 800 nm in diameter. They are smooth, non porous, and have a low surface area. While this isn’t a support that would typically be used in industrial applications because of its low surface area, it is a step closer from flat model supports to high surface area powders. The characteristics of these SiO_2 spheres make them a bridge between model supports and supports that would be used in industrial applications. This support is easier to study through microscopy because of its low surface area and lack of pores than a typically high surface area support would be. The Stöber spheres were coated with TiO_2 in much the same way as the flat samples, one dry and one wet sample. Figure 3.7 shows STEM images of the dry sample before and after calcination treatments along with the corresponding PSDs. Much like the dry flat sample, the particles were mostly stable after the 400°C calcination but there was significant particle growth after the subsequent 700°C calcination.

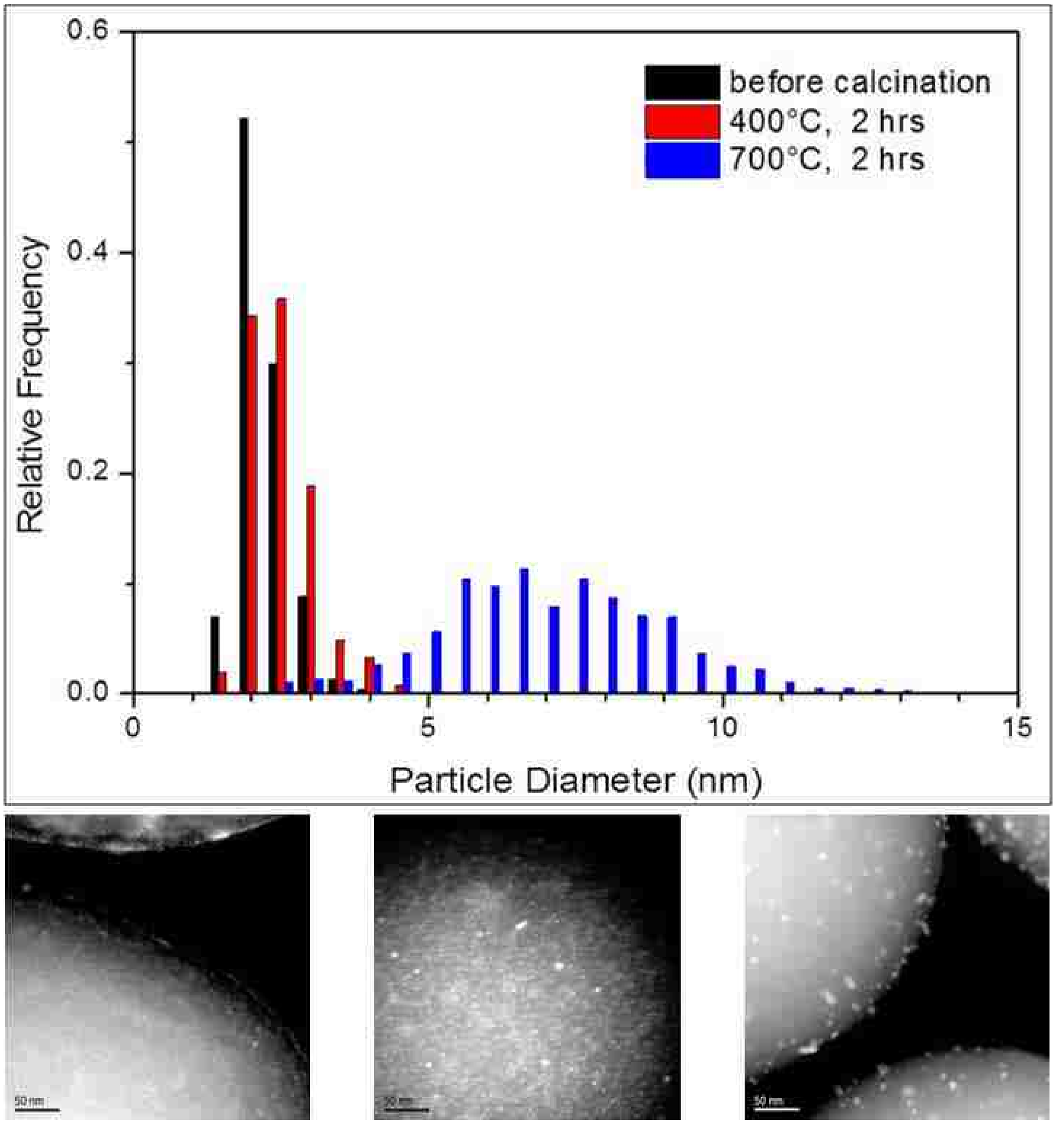

Figure 3.7 Au/TiO_2/Stöber spheres (dry), a) PSDs before and after calcination treatments, b) STEM image of freshly reduced sample, c) STEM image after 400°C calcination in air for 2 hrs, d) STEM image after 700°C calcination in air for 2 hrs.

The Stöber spheres were also coated with TiO_2 under wet conditions. The PSDs and microscopy images of the wet sample both before and after calcination treatments are shown in Figure 3.8. The figure clearly shows that much like the wet wafer sample, the Au particles are stable when deposited on hydrolyzed TiO_2 coated on SiO_2.

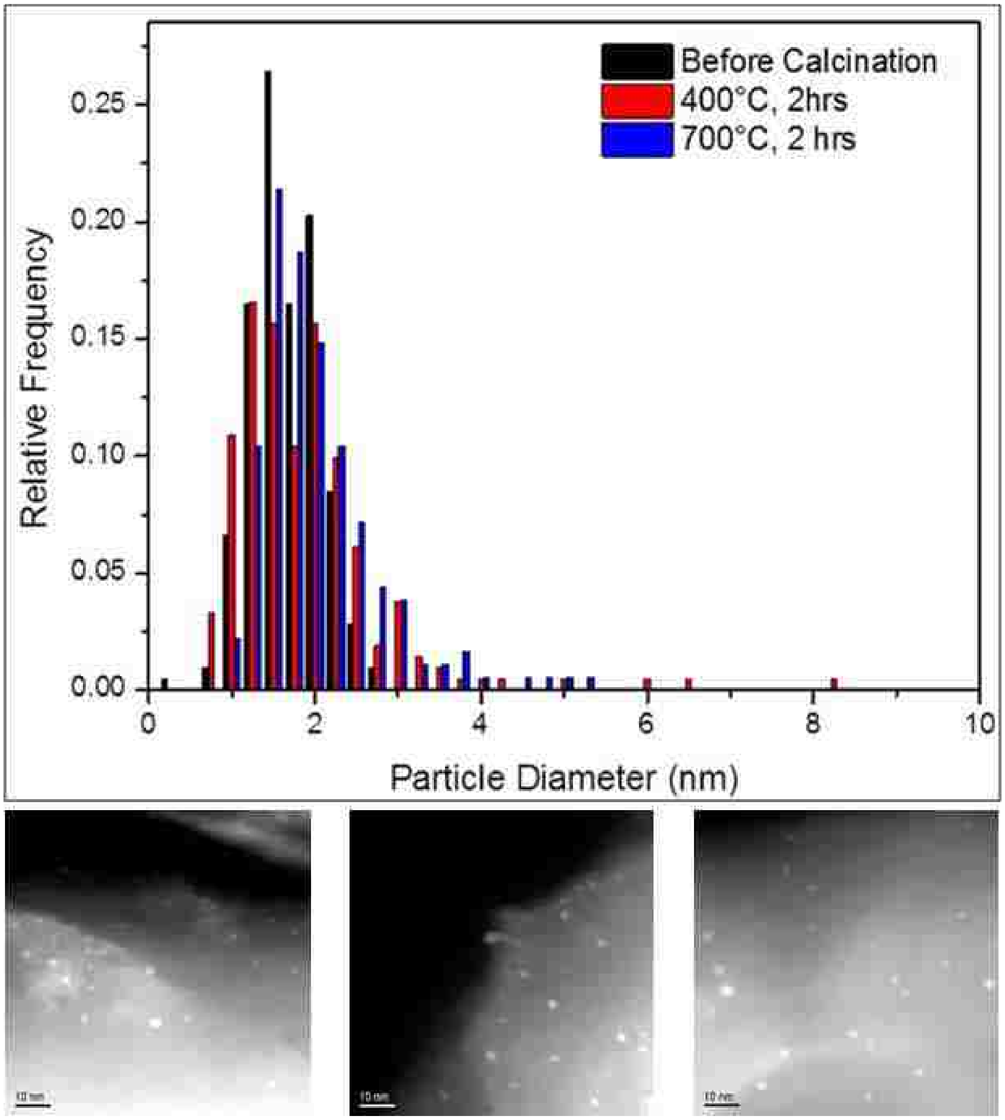

Figure 3.8 Au/TiO_2/Stöber spheres (wet), a) PSDs before and after calcination treatments, b) STEM image of freshly reduced sample, c) STEM image after 400°C calcination in air for 2 hrs, d) STEM image after 700°C calcination in air for 2 hrs.

3.5 Discussion

The electron microscopy images and analysis clearly show that the conditions during TiO_2 deposition on SiO_2 can greatly affect the thermal stability of Au NPs deposited on the mixed oxide support. It was found through AFM that the hydrolyzed TiO_2 created a rougher surface morphology than the TiO_2 deposited under dry conditions.

The average diameter of Au NPs are shown in Table 3.1 for the wet and dry samples both on the wafer and powder supports along with the WGC sample for reference. The % change compared to the fresh sample is also shown in the table. Most samples show little change in average particle size after the 400°C calcination but there is a more significant change in the WGC and dry samples after the 700°C calcination. The dry samples showed particles grew 157% and 240% for the dry samples, which is comparable to the 247% in particle growth for the WGC reference sample. In contrast, both the wet samples showed < 30% particle growth even after the 700°C calcination.

Table 3.1 Average diameters of samples, before and after calcination treatments. Table also shows % change of average diameter compared to the fresh catalyst.

		WGC	dry wafer	wet wafer	dry powder	wet powder
average diameter (nm)	fresh	3.2	4.9	3.4	2.0	1.5
	400°C	3.1	6.7	3.9	2.3	1.8
	700°C	11.1	12.6	4.4	6.8	1.9
Δ (%)	400°C	-3	37	15	15	20
	700°C	247	157	29	240	27

3.6 Conclusions

In this study, we were able to vary the morphology of TiO_2 on SiO_2 by varying the degree of hydrolysis of the TiO_2 precursor. The difference in surface roughness between the two different mixed oxides was shown with AFM on the flat samples. The rougher support (hydrolyzed TiO_2) was able to stabilize gold nanoparticles at temperatures up to 700°C while the gold nanoparticles on the smoother support sintered significantly. The concept of using this synthesis method to create a rougher surface on a flat support was used to create powder support that is a step closer to a practical catalyst. SiO_2 Stöber spheres were coated with hydrolyzed and non-hydrolyzed TiO_2 and we found that the same phenomena applied to the powder supports. This study is proof that the mixed oxide support morphology can have an enormous impact on the stability of the supported metal.

4. Improved Selectivity of Carbon-Supported Palladium Catalysts for the Hydrogenation of Acetylene in Excess Ethylene

4.1 Abstract

In this study we examine the role of the support for selective hydrogenation of acetylene. Palladium (Pd) nanoparticles with a narrow size distribution were deposited on three supports, carbon, alumina and magnesia. The Pd particles ranged from 0.5 to 1.0 nm in diameter. A novel synthesis based on room temperature alcohol reduction of the Pd acetate precursor allowed us to deposit similar sized Pd particles on all three supports. We used electron microscopy and X-ray absorption spectroscopy (EXAFS) to characterize these samples and to confirm the similarity of the distribution and the size of the nanoparticles on all three supports. The carbon-supported Pd yielded a higher selectivity to ethylene at 100% acetylene conversions (from acetylene/ethylene mixtures) when compared to the oxide-supported samples. This work provides clear evidence that the support can play an important role in the selective hydrogenation of acetylene. While alumina is extensively used in industry as the support for Pd and Pd alloys, considerable improvements in selectivity could be made by the use of carbon supports.

4.2 Introduction

Ethylene is a high volume commodity that is important for the polymer industry. It is used to produce chemical compounds such as ethylene oxide, polyethylene, and ethylene dichloride, which are precursors for many consumer products, including surfactants, detergents, plastic bags, films and piping. The steam cracking of hydrocarbons produces ethylene and acetylene is a byproduct of this process. The 0.5-

2% of acetylene in the ethylene is enough to poison the catalysts used to polymerize ethylene into polyethylene [47]. Palladium (Pd) catalysts have been shown to be effective to selectively hydrogenate acetylene to ethylene while preventing over hydrogenation to ethane [48]. The hydrogenation reaction is shown schematically in Figure 4.1. Catalysts used for this reaction must retain high selectivity to ethylene at high acetylene conversions since it is essential to reduce to amount of acetylene to 5-10 ppm in order to protect the polymerization catalysts [49].

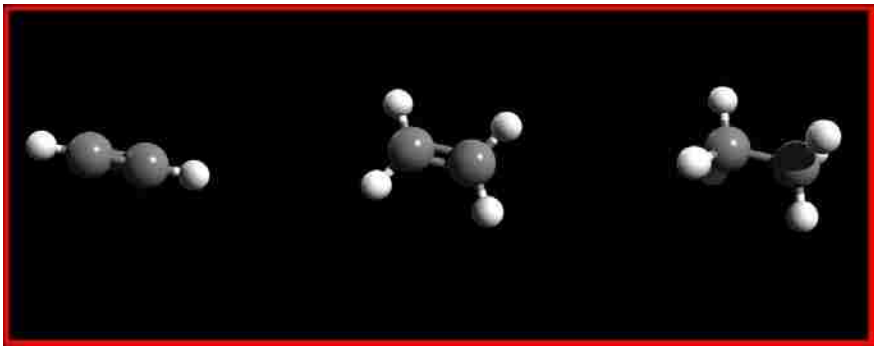

Figure 4.1 Schematic showing the hydrogenation of acetylene reaction

In current industrial practice, Pd catalysts are modified with an additive such as silver, silicon, germanium or lead [50-52] and α-alumina is often used as a support. The additives help to improve the selectivity, but there still many challenges in the industrial application of these selective hydrogenation catalysts. The catalyst experiences deactivation over time and undergoes restructuring during regeneration which affects its performance. There is often carbon monoxide (CO) in the feed stream which improves selectivity [53] but the CO leads to the undesirable formation of oligomers, often referred to as green oil. These green oils build up on the catalyst surface and cause deactivation [54-56].

Studt et al. [57] performed density functional calculation studies that suggest that ethylene selectivity is related to the binding energies of the adsorbates onto the metal surface. This study showed that the activation energy barrier for ethylene hydrogenation on pure Pd is about the same as the ethylene desorption energy. Their calculations show the addition of silver (Ag) to Pd increases the activation energy for the hydrogenation of ethylene to an energy that allows for desorption of ethylene before it can be further hydrogenated. This work suggests that selectivity in the acetylene hydrogenation reaction is strictly a result of binding of the adsorbates to the metal surface and is unaffected by the catalyst support. However, previous studies have shown that the support may play a role in selectivity [58]. Bauer et al. [59] studied selective hydrogenation of propyne and found that Pd supported on alumina was not selective to propene when conversion of propyne approached 100%. In contrast, the Pd supported on carbon nanotubes was more selective. The samples they studied had a broad particle size distribution, but they also found that particle size influenced selectivity. Therefore, to study the role of the support, we feel it is important to keep other parameters such as catalyst precursor and metal particle size constant.

It is difficult to synthesize catalysts having the same particle size (or dispersion) on different supports, using aqueous precursors. This is because supports such as SiO_2 or Al_2O_3 have different points of zero charge (PZC), which influence the adsorption of metal salts [2]. The PZC is 1.1 and 7.9 for SiO_2 and Al_2O_3 respectively, influencing the resulting particle size for catalysts prepared using incipient wetness impregnation [3]. And in the case of another support commonly used, zinc oxide (ZnO), the strongly acidic solutions of the precursor make it difficult to prepare catalysts without modifying the support morphology [4]. Hence, there is a need to use a synthesis method that has the ability to deposit similar sized particles on different supports starting from the same precursor. There are colloidal methods that use ligands and capping agents to generate uniformly sized particles but these ligands must be removed subsequently, otherwise they will interfere with the catalyst activity [7,60]. The removal of the ligands often involves high temperatures and harsh conditions that can cause particle sintering and also add an extra costly and time consuming step during synthesis, which could influence the support and/or metal support interface. The ligand removal step could also influence the selectivity and activity of the metal phase [8,9].

In this work we used a method recently developed by Burton et al. [10] where methanol is used as the reducing agent for a Pd acetate precursor at room temperature. Using this method, Pd nanoparticles can be deposited on both oxide and carbon supports while maintaining similar particle sizes. This synthesis method allowed us to generate highly dispersed Pd particles (~ 1 nm in diameter) so as to maximize the metal-support interaction. We prepared Pd particles with an average diameter less than 1 nm on carbon, Al_2O_3, and magnesium oxide (MgO). The Pd catalysts were tested for the hydrogenation of acetylene in excess ethylene, and the results show that the catalytic performance varies markedly with the support, with the carbon support providing the highest selectivity under conditions where the conversion of acetylene is near 100%.

4.3 Experimental Methods

4.3.1 *Preparation of supported catalyst*

Supported 1wt% Pd nanoparticle catalysts were synthesized via a method developed by Burton, et al. [10] The alcohol reduction method is carried out by dissolving anhydrous $Pd(OAc)_2$ (20 mg) in anhydrous methanol (30 mL) in a glass vial to get 3mM Pd acetate in methanol. This was done under ambient pressure and temperature. The vial was capped and placed in a ultrasonic bath for ~10 minutes, until the $Pd(OAc)_2$ was completely dissolved. The solution was then added to 1 gram of the support in a round bottom flask. Three supports were used in this study, carbon (Vulcan XC72R obtained from Cabot Corporation), MgO (Inframat Advanced Materials), and γ-Al_2O_3 (Catapal B obtained from Sasol). The BET surface areas are 274, 32, and 160 m^2/g for carbon, MgO, and Al_2O_3 respectively. The round bottom flask was then attached to a rotary evaporator, where the sample was maintained at ambient temperature until it dried completely (~20min). The time required to dry the powder varied depending on the fineness of support powder. The catalyst was removed from the flask and allowed to dry overnight. No further treatment was performed before characterization or testing. These 1wt% Pd catalysts do not need any calcination or reduction, since there are no ligands to remove, and the catalysts are reactive as-prepared. The methanol serves as a reducing agent and could also serve as the ligand that stabilizes the nanoparticles that are formed. However, if the solution is let standing for several hours, the Pd colloids will grow in size and fall out of the solution. This method of sample preparation to yield monodispersed nanoparticles on different supports is successful only when the solution is contacted with a support in a short amount of time.

4.3.2 *Electron Microscopy*

A holey carbon copper TEM grid was dipped into a solution of the catalyst powder dispersed in ethanol. We used an electron beam shower to reduce contamination during STEM imaging. An aberration corrected FEI Titan 80-300 kV G2 TEM-STEM was used to record images in the high angle annular dark field mode. The images were converted from TIA software (FEI) to DigitalMicrograph™ (Gatan) for analysis. Particles were counted by hand using the Measure Features script from the DM-script-database [46]. The images were filtered after analysis to reduce noise using the smooth special filter feature in DigitalMicrograph™ for presentation.

4.3.3 *X-ray Absorption Spectroscopy*

EXAFS measurements were performed at the Pd K-edge using the insertion-device beam line (10ID-B) of the Materials Research Collaborative Access Team (MRCAT) at the Advanced Photon Source of Argonne National Laboratory. The samples were loaded into an in situ holder and reduced in 3.5% H_2/He at 115°C for 1 hour and then cooled to room temperature in flowing He. The samples were then transferred to the beam line without air exposure. All spectra were taken in transmission mode at room temperature with a Pd foil in the reference position. Two spectra of each catalyst were recorded, one of the as-prepared sample and one of the sample after H_2 reduction.

Experimental EXAFS data $\chi(k)$ (where k is the photoelectron wave number) were processed by subtracting the background from the normalized absorption coefficient using the Athena [61] program of the IFEFFIT data analysis package [62]. The theoretical EXAFS signal was constructed using the FEFF6 code [63] and fitted to the data in r-space using the Artemis [61] program of the IFEFFIT package. S_0^2 (the passive electron reduction factor) was obtained by first analyzing the Pd foil, and the best fit value (0.84) was fixed during the fitting of the catalyst samples. The spectra were fitted in r-space by varying the coordination number of the single scattering path, the bond length disorder (Debye-Waller factor), σ^2, the effective scattering length (R), and the correction to the threshold energy, ΔE_0. The k-range used for Fourier Transform of the $\chi(k)$ was 2.5–13 $Å^{-1}$ and the r-range for fitting was 1.0-2.2 Å for the samples without a Pd-Pd contribution and 1.4-3.1 Å for the reduced samples. XANES analysis was also done using Athena by performing a linear combination fit of a Pd and PdO standard. Because of the small size of the particles, they cannot be properly represented by a Pd foil standard for the linear combination fitting. A sample of Pd nanoparticles supported on alumina that was synthesized using the above preparation procedure and reduced at 200°C in H_2 was used as the Pd reference for the XANES analysis. This sample was fully reduced at this temperature and has a coordination number of 6.7. The PdO standard used for XANES was an Aldrich bulk PdO.

4.3.4 *Catalytic Testing*

The catalyst was granulated by pressing the dried powder under ~5 metric tons with a Carver hydraulic press to produce a pellet. The pellet was ground and the powder sieved to between 106 and 250 µm using # 140 and # 60 US standard testing sieves from VWR, the size range for the catalyst particles was chosen to ensure proper flow in the microreactor and prevent channeling of the gas. A sample of 20 mg of this sieved catalyst was mixed with 400 mg SiC (350 µm average grain size, Washington Mills) as an inert to minimize temperature gradients. The mixed powder was packed in a 0.25 in. quartz tube between two plugs of quartz wool. A mixture of acetylene (0.5%) and ethylene (35%) in a balance of nitrogen was passed over the powder at a flow rate of 66 mL/min. The hydrogen flow rate was 1.4 mL/min. Product gases were analyzed by a Varian 3800 gas chromatograph equipped with a CP-PoraBOND U column and a FID detector. The reactor was heated from room temperature up to 125°C in a stepwise fashion and data collected every 10°C. At each temperature, the GC sampled five injections of the effluent gas before moving to the next temperature, which held the catalyst at each temperature for approximately 35 minutes. The catalyst was cooled in flowing nitrogen and the run was repeated. There was little difference between runs and therefore we have reported the second run for each sample. An average of all five injections at each temperature was used for data analysis.

A Pd/alumina industrial look-alike catalyst was used as a reference to provide a comparison with the catalysts prepared in this work. This reference catalyst consisted of 0.05wt% Pd loaded on α-Al_2O_3 beads. The egg-shell morphology ensures that Pd is present in the near-surface region on the Al_2O_3 beads. The Pd particle size shows a broad size distribution with a mean diameter of 10 nm. This sample is referred to as Pd/Al_2O_3 reference in order to distinguish it from the Al_2O_3 supported sample prepared using alcohol reduction. The amount of this reference catalyst used during reaction testing was scaled so that the amount of Pd in the reactor was kept constant for all of the runs. This reference catalyst was also ground and sieved so it would be compatible with the size of our reactor.

4.4 Results

4.4.1 *Transmission Electron Microscopy*

Aberration corrected electron microscopy (ACEM) was used to determine the particle size and morphology of as-prepared samples. A representative image of each sample, Pd/C, Pd/MgO, and Pd/Al_2O_3, is shown in Figure 4.2. The image contrast in this high angle annular dark field (HAADF) mode is atomic number dependent ($\sim Z^{1.7}$), hence the bright regions represent Pd particles while the less bright regions represent the support. All of the images are shown at the same magnification. The Pd particles range in size from 0.3 to 2.8 nm on all of the three supports.

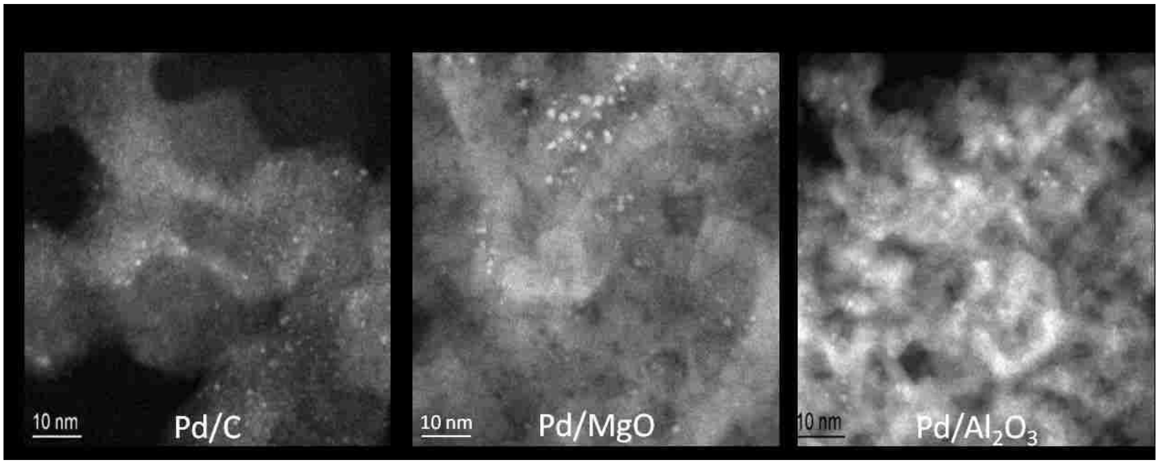

Figure 4.2 Representative STEM images of as-prepared 1wt% Pd on a) carbon, b) MgO, and c) Al_2O_3.

Five different images for each support were used to analyze the number of size of Pd nanoparticles. More than 100 particles were counted for each sample. The particle sizes were put into 0.2 nm bins to create the particle size distributions (PSDs) shown in Figure 4.3. The PSD for MgO is shifted to the right indicating that the Pd particles on the MgO support are slightly larger than on the other two supports. This can also be seen in the images in Figure 4.2. The analysis of STEM images gives a mean particle diameter of 0.7 nm, 1.0 nm, and 0.8 nm for Pd/C, Pd/MgO, and Pd/Al_2O_3, respectively.

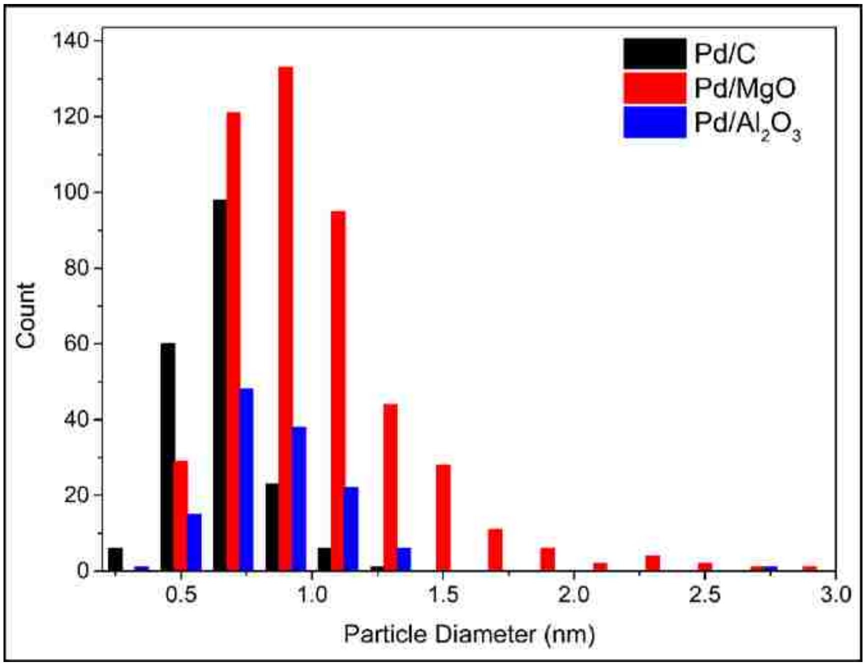

Figure 4.3 Particle size distributions from STEM images of as-prepared samples.

While the mean particle sizes are not identical, they show a narrow distribution. The microscopy results confirm that the synthesis method has enabled the deposition of similar sized Pd nanoparticles on three different supports using the same precursor. The differences in size can be related to the differences in BET surface area of the three supports. Since similar metal loading was used, the sample with the lower surface area (MgO) exhibited the largest particles. This indicates that while the methanol is able to reduce the Pd acetate to zero valent Pd in solution, the final nanoparticle size on the support is determined by the metal loading, which yields larger particles for the support having the lowest surface area.

4.4.2 *EXAFS*

To confirm that the particle sizes obtained through STEM analysis were representative of the entire sample, the samples were characterized using EXAFS. The EXAFS data plotted in r-space for the Al_2O_3 sample is shown in Figure 4.4.

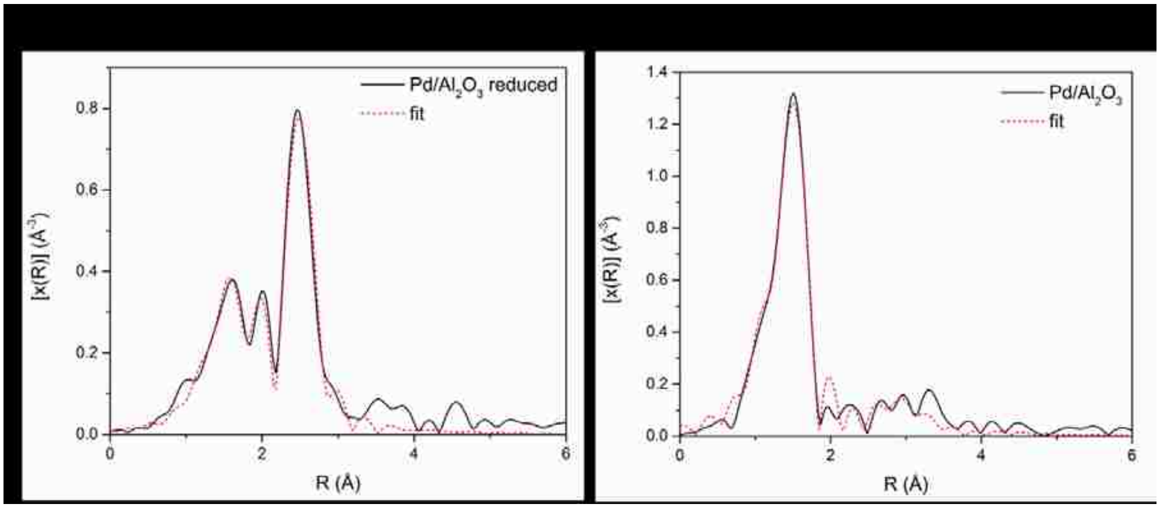

Figure 4.4 Fourier transform magnitudes of the k^2-weighted $\chi(k)$ data for the Pd K-edge EXAFS spectra of the Pd/Al_2O_3 samples, a) reduced at 115°C and b) as-prepared, along with the best fit.

This was obtained by Fourier transforming the k^2-weighted data from 2.5-12Å^{-1}. Figure 4.44 shows the magnitude of the Fourier transform for the Pd/Al_2O_3 sample, both as-prepared and after reduction at 115°C, along with their best fits. The r-space EXAFS data for the as-prepared samples is shown in Figure 4.5.

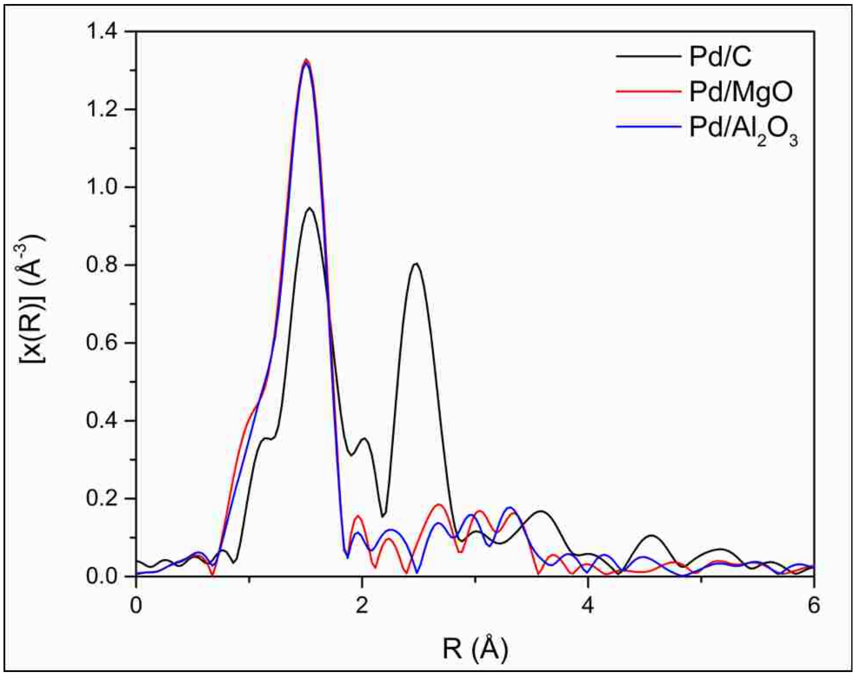

Figure 4.5 Fourier transform magnitudes of the k^2-weighted χ(*k*) data for the Pd K-edge EXAFS spectra of the as-prepared Pd on carbon, MgO, and Al_2O_3 samples.

The most notable feature in this graph is that the carbon sample has a prominent peak at 2.74Å (corresponding to the Pd-Pd distance), which is not present in the patterns derived from the oxide samples. Table 4.1 shows the results of EXAFS analysis of the as-prepared samples. The analysis gives a Pd-Pd coordination of 3.0 for the carbon sample and no Pd-Pd coordination for the oxide samples.

Table 4.1 XANES and EXAFS fitting results for Pd/C, Pd/MgO, and Pd/Al_2O_3 samples as-prepared. The numbers in parenthesis indicate the statistical error in the significant digit obtained from the fit in Artemis.

catalyst	%PdO (XANES)	scatterer	N	R (Å)	σ^2 (Å^2)	ΔE_0 (eV)
Pd/C	60	Pd-Pd	3.0(5)	2.740(6)	0.0065(9)	-5(1)
		Pd-O	2.8(3)	2.017(9)	0.004(1)	4(1)
Pd/MgO	100	Pd-O	3.9(4)	2.013(7)	0.0018(9)	3(1)
Pd/Al_2O_3	100	Pd-O	3.9(4)	2.011(8)	0.002(1)	4(1)

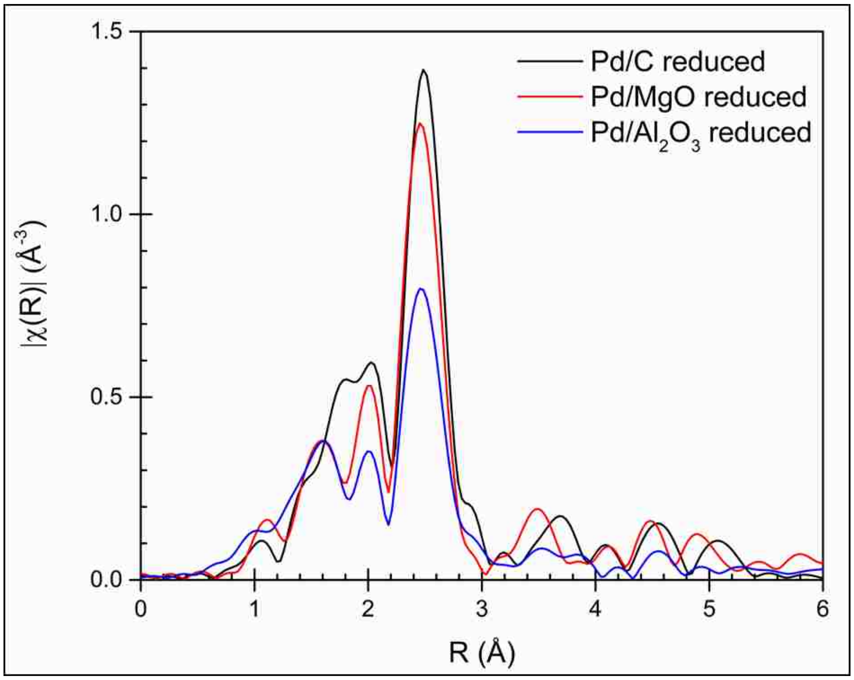

Figure 4.6 Fourier transform magnitudes of the k^2-weighted $\chi(k)$ data for the Pd K-edge EXAFS spectra of the Pd on carbon, MgO, and Al_2O_3 samples after reduction in H_2 for 1 hour at 115°C.

Figure 4.6 compares the EXAFS data in r-space for the three samples after reduction at 115°C. The reduced samples were used to emulate the working catalyst since all of the catalysts reached full conversion before 115°C and excess H_2 was used in the reaction. Table 4.2 shows the results of the XANES and EXAFS analysis of the reduced samples. All three samples showed Pd-Pd bonds at 2.74Å with the first shell coordination number ranging from 4.4 to 6.1. In the case of Al_2O_3 and MgO, there is a small peak that corresponds to Pd-O bonding at ~2.03Å.

Table 4.2 XANES and EXAFS fitting results for Pd/C, Pd/MgO, and Pd/Al_2O_3 samples after reduction at 115°C for 1 hour. The numbers in parenthesis indicate the statistical error in the significant digit obtained from the fit in Artemis.

catalyst	% PdO (XANES)	scatterer	N	R (Å)	σ^2 (Å^2)	ΔE_0 (eV)
Pd/C reduced	0	Pd-Pd	6.1(4)	2.742(3)	0.0077(4)	-2.4(5)
		Pd-C	1.6(5)	2.28(3)	0.006 (4)	7(3)
Pd/MgO reduced	12	Pd-Pd	6.1(6)	2.746(5)	0.0080(7)	-1.3(7)
		Pd-O	0.5(2)	2.02(3)	0.000(3)	11(5)
Pd/Al_2O_3 reduced	15	Pd-Pd	4.4(2)	2.738(4)	0.0091(5)	-0.9(3)
		Pd-O	0.6(1)	2.03(1)	0.001(2)	0.001(2)

The data fits show a small feature from Pd-O which is confirmed by XANES analysis. The higher white line intensity for the MgO and Al_2O_3 samples indicate the presence of Pd-O bonding which is similar to having about 12 and 15 % of the Pd present as PdO (by linear combination fitting of nanoparticle Pd and PdO standards). However, we believe that the Pd-O bonding detected in the oxide supported samples is not a separate PdO phase but rather the interaction between the Pd particle and the support. XANES data is shown in Figure 4.7. The carbon sample showed, in addition to the Pd-Pd neighbors, a second feature corresponding to a bond distance of 2.28Å, which fits a Pd-C bond.

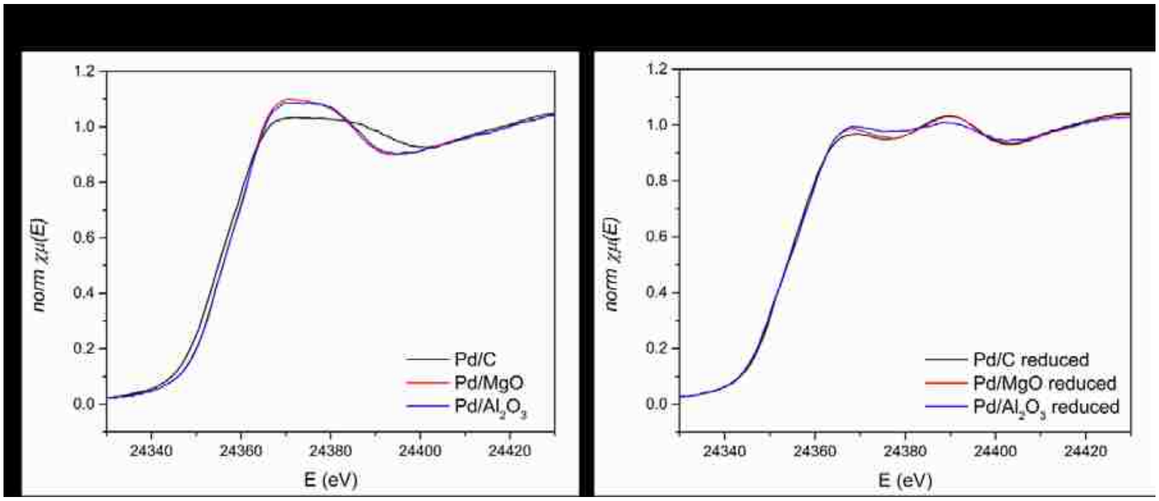

Figure 4.7 Pd K-edge XANES spectra of a) as-prepared catalysts and b) catalysts after reduction at 115°C for 1 hour.

4.4.3 *Catalytic Performance*

The reactivity and selectivity of each of the as-prepared catalysts was tested for the selective hydrogenation of acetylene. Figure 4.8 shows acetylene conversion as a function of temperature. All three catalysts reached 100% acetylene conversion between 75°C and 105°C. The oxide samples are more active than the carbon supported Pd. In each case, we did multiple hydrogenation runs and found the catalysts to be stable from run to run.

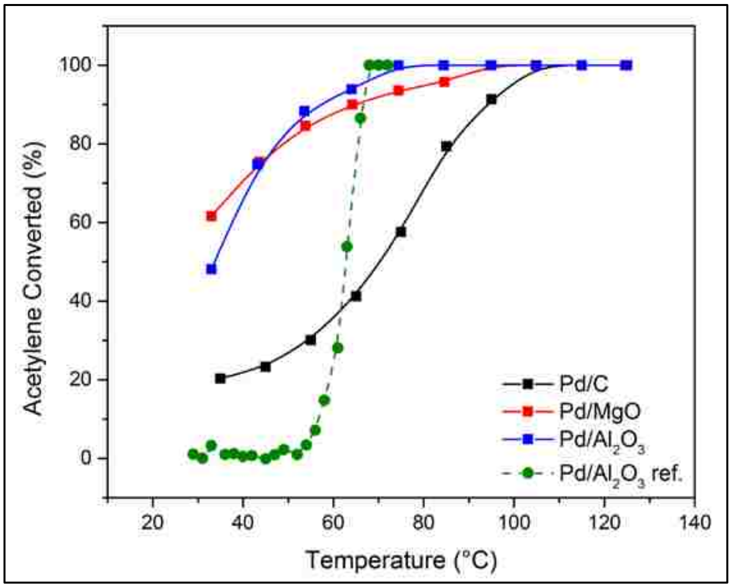

Figure 4.8 Acetylene conversion vs. temperature for as-prepared samples along with a reference sample of Pd/Al2O3. The reactor feed was a mixture od acetylene (0.5%) and ethylene (35%) in a balance of nitrogen was passed over the powder at a flow rate of 66mL/min.

Figure 4.9 shows reactivity measurements carried out over 5 hours under isothermal conditions showing the stability of these catalysts. Both the acetylene conversion and ethylene selectivity are constant over the 5 hour period at 3 different temperatures, 65°C, 75°C, and 85°C

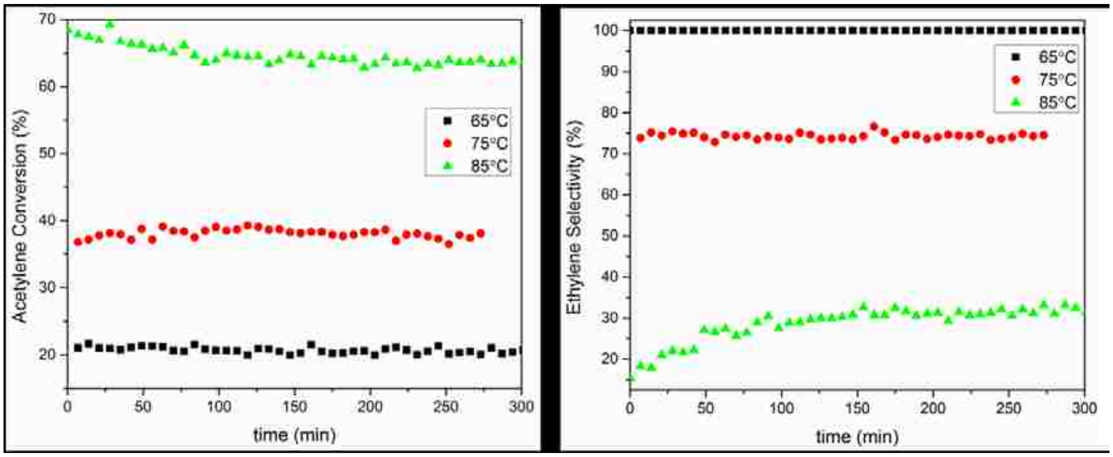

Figure 4.9 Plots showing acetylene conversion and ethylene selectivity vs. time at 65°C, 75°C, and 85°C for Pd/Al$_2$O$_3$ reference sample. The graphs show that both conversion and selectivity are constant after several hours under isothermal conditions.

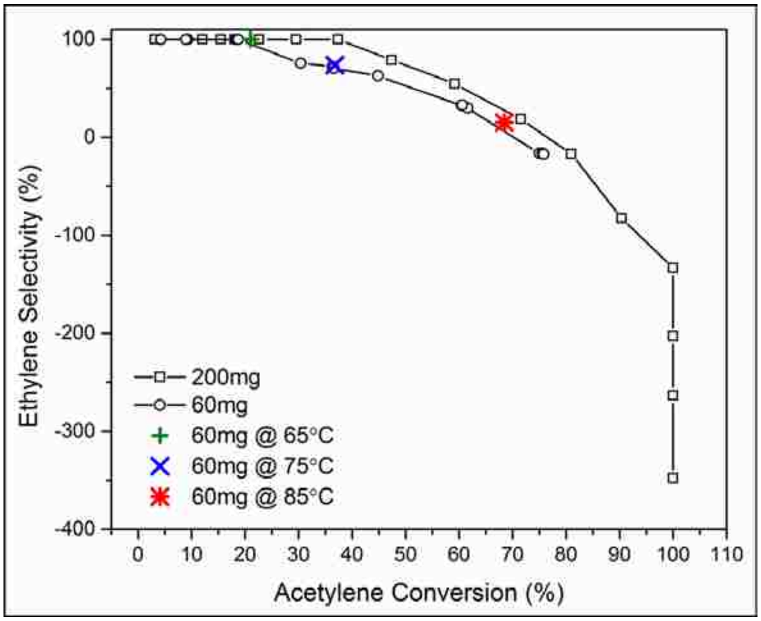

Figure 4.10 Plot showing selectivity vs. conversion data for 200mg and 60mg for Pd/Al_2O_3 reference samples. Data for 60mg of catalyst run under isothermal conditions is also shown.

Finally, we varied the amount of catalyst and show that the selectivity is not influenced by variations in the space velocity (Figure 4.10). Appendix A shows results that demonstrate the absence of heat and mass transfer limitations (via a Mears analysis) indicating that the observed behavior (selectivity vs conversion of acetylene) provides an intrinsic measure of the performance of the catalyst. In Figure 4.8 we only included results for the second run for each of the samples. The excess ethylene selectivity for this reaction is defined as the moles of ethylene generated per mole of acetylene consumed, as shown in the following equation:

$$excess\ ethylene\ selectivity = \frac{C_{effluent}^{ethylene} - C_{feed}^{ethylene}}{C_{feed}^{aceylene} - C_{effluent}^{aceylene}} \tag{4.1}$$

An excess ethylene selectivity of 100% indicates that all of the acetylene was converted to ethylene with no over-hydrogenation to ethane. A negative excess ethylene selectivity indicates all of the acetylene converted to ethylene was hydrogenated to ethane as well as consuming some of the ethylene feed. Positive excess ethylene selectivity is desirable, especially at near 100% conversion of acetylene, since it indicates that a significant portion of the acetylene has been hydrogenated to form ethylene without over-hydrogenation to ethane.

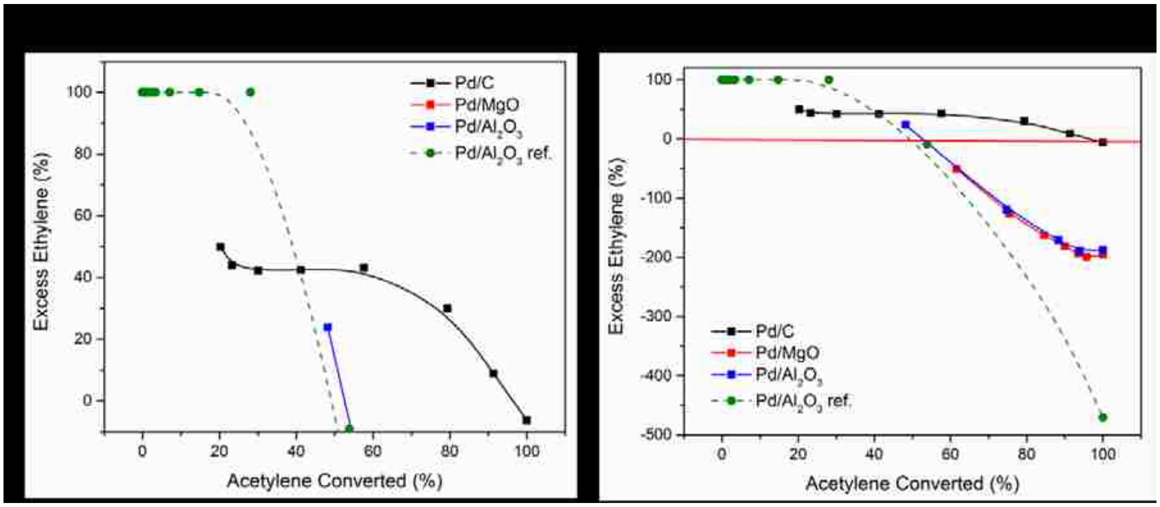

Figure 4.11 Ethylene selectivity vs. acetylene conversion of as-prepared catalysts along with a Pd/Al_2O_3 reference catalyst. a) Highlights the positive selectivity range showing only the Pd/C catalyst maintains positive selectivity at full conversion. b) Shows the entire selectivity range. The horizontal line corresponds to 0% excess ethylene, meaning all the acetylene has been converted to ethane.

Figure 4.11 shows the excess ethylene selectivity vs. acetylene conversion for the three samples. The Pd/C shows positive selectivity over the entire range of acetylene conversions, while the other Pd catalysts show negative selectivity at high acetylene conversion. Since this measure of selectivity involves a difference between two large numbers (we start with a 70:1 ratio of ethylene to acetylene), we also calculated excess ethylene using the difference between acetylene consumed and ethane formed as reported by Liu et al. [64] and Menezes et al. [65], this alternate definition gave identical results.

4.5 Discussion

The goal of this study was to prepare catalysts with similar particles sizes on a variety of supports. The electron microscopy data confirms that the majority of the particles are between 0.5 and 1 nm in diameter. EXAFS was used to corroborate the information obtained via STEM. We studied only the as-prepared samples to capture the characteristics that represent the sample as it was loaded into the reactor, representing the precursor to the working catalyst. Samples after reaction were not analyzed since imaging was difficult due to carbon contamination, as noted previously by Shao et al. [66]. The as-prepared samples showed significant oxygen coordination by EXAFS due to air exposure, similar to the report of Bauer et al. [59]. Hence samples after a mild 115°C reduction were also analyzed, and it was found that the reduced samples show a decrease in the contribution from oxygen neighbors and the presence of metal-metal nearest neighbors. These coordination numbers obtained from EXAFS ranged from 4.4-6.1 for the H_2 reduced samples.

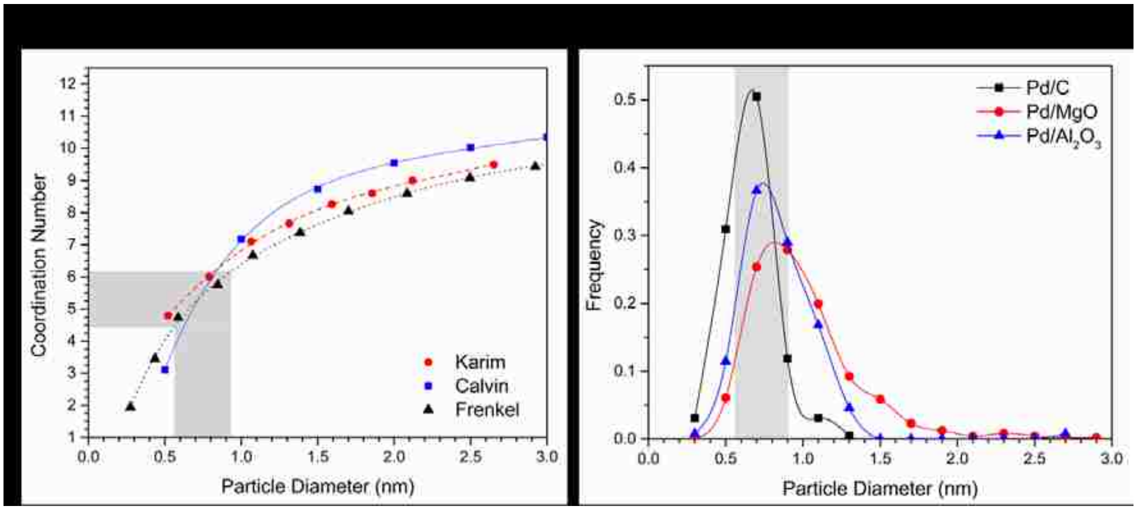

Figure 4.12 a) Correlation between coordination number and particle size obtained for Karim et al. [67], Calvin et al. [68], and Frankel et al. [69]. The shaded region indicates the coordination number obtained for EXAFS and how that range translates to a range in particle diameter. b) PSDs from STEM with particle size range obtained from EXAFS analysis shown in shaded region.

Figure 4.12a shows the EXAFS coordination number vs. particle diameter. Various models have been proposed to relate particle diameter to EXAFS coordination, Calvin [70] assumes a sphere while Karim [67] and Frenkel [69] both use hemispherical and cuboctahedral shapes, respectively. Despite the differences in assumed particle shapes and structures, these correlations provide similar numbers for particle diameter and constitute the error in assigning a particle diameter based on EXAFS that can be then be used to correlate with the TEM measurements. The shaded region in this graph indicates the range of coordination numbers obtained from EXAFS and how those numbers translate to a particle diameter range using the three correlations indicated. According to this figure, the particle diameters inferred from the coordination numbers obtained from EXAFS suggest particle diameters ranging from 0.5 to 0.9 nm. Figure 4.12b shows the PSDs obtained through STEM analysis. This is the same data shown in Figure 4.3, but plotted as particle frequency (normalized to the total number of particles counted) and shown as curves instead of bars. The shaded region in this graph is the particle size range suggested by EXAFS. This graph makes it clear that the particle sizes obtained from both STEM and EXAFS are consistent with each other. It should also be noted that while coordination numbers of 4.4 and 6.1 for Al_2O_3 and MgO, respectively, are consistent with the PSD from STEM (the average Pd nanoparticles size is smaller on Al_2O_3 compared to that on MgO), a 6.1 coordination number for Pd/C is larger than expected since the Pd nanoparticles were the smallest on carbon (average diameter = 0.7 nm). This can be explained by a difference in particle shape. The Pd particles on carbon are likely spherical while the particles on the oxides are probably hemispherical. A spherical particle with a coordination number of 6.1 will be smaller than a hemispherical particle with the same coordination number [69].

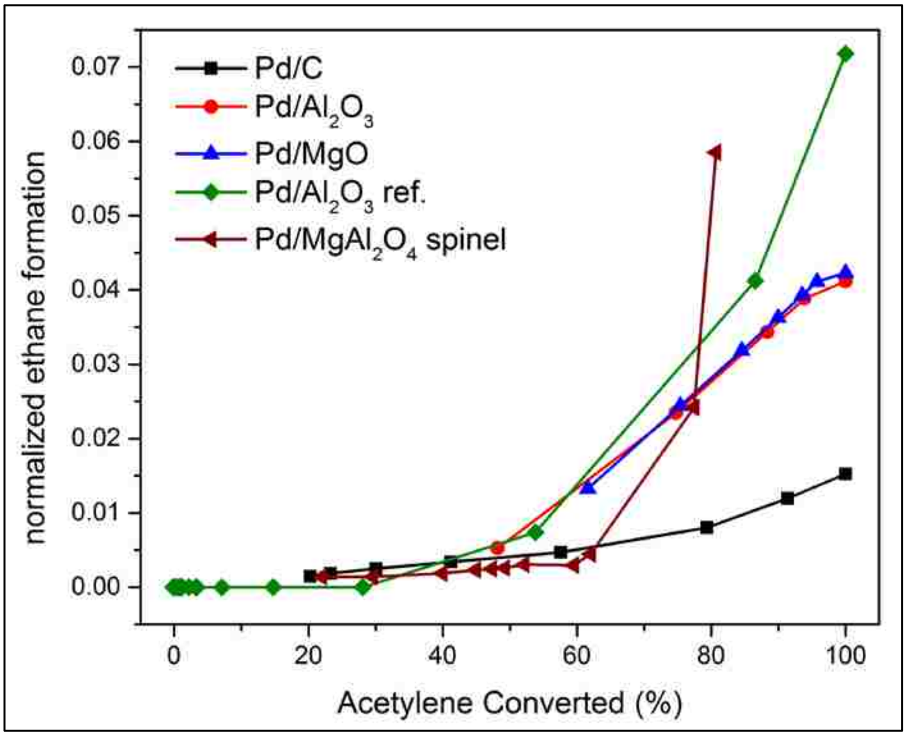

Figure 4.13 Ethane formed per mole of ethylene fed as a function of acetylene conversion of the as-prepared catalysts along with a reference Pd/Al_2O_3 sample and the data on Pd/$MgAl_2O_4$ reported by Studt et al. [57].

Figure 4.13 shows the catalyst selectivity in terms of ethane formed during the reaction as a function of acetylene conversion. The ethane formation was expressed per mole of ethylene in the feed. This normalization was done to allow comparison with published results where a different feed concentration of ethylene was used. The ethylene to acetylene ratio in our study, 70:1, was used to simulate industrial conditions. The selectivity data in this study is compared to data by Studt et al. [57] and to the Pd/Al_2O_3 reference sample. The figure shows that the Pd/C produces much less ethane at high acetylene conversion than the Pd sample used by Studt et al. [57] as well as the oxide supported Pd samples prepared by us in this work. The Pd/Al_2O_3 reference sample produced much more ethane at high acetylene conversions under these reaction conditions than any of the samples prepared by us. The reference Pd/Al_2O_3, while similar to industrial catalysts in that it is supported on α-alumina and has a shell of Pd, it does not include Ag or other promoters typically used in industry. Industrial catalysts use high ratios of Ag to Pd to further improve selectivity. Our results clearly show that Al_2O_3 may not be the best support to achieve high selectivity, and significant improvements in selectivity could be obtained just by switching to a carbon support. While carbon supports may not be desirable where oxidative treatments are necessary to burn off carbonaceous deposits, we have shown recently [71] that the improved acetylene selectivity can also be obtained on oxide supports where a carbon coating has been applied after metal deposition. The method of applying carbon coatings to oxide supports is simple and presents an alternative approach to modify oxide based catalysts. The results of this study show how carbon based supports could enhance the performance of Pd based selective hydrogenation catalysts used in industry. Further improvements would be obtained by adding modifiers such as Ag.

There are several hypotheses on the mechanisms responsible for the enhanced selectivity during alkyne hydrogenation. Recent work by Bauer et al. [59] as well as Tew et al. [72] suggests that carbon is incorporated into the Pd particles after exposure to the alkynes, and is responsible, in part, for poisoning the Pd surfaces and leading to higher selectivity in this reaction. Teschner et al. [73] have also proposed that the dissolution of small amounts of carbon into the Pd lattice inhibit bulk-dissolved hydrogen which is responsible for the non selective reaction leading to alkane formation. However, recent work from the same group [66], concludes that “subsurface PdC_x cannot be discussed as the main factor determining selectivity.” Since we did not have access to EXAFS measurements under reaction conditions, we cannot comment on the changes caused to our catalysts by exposure to the reacting gases. However, the focus of this study is not on the mechanisms leading to high selectivity, but to document conclusively that the support can play a significant role.

Therefore our characterization pertains to the as-prepared catalyst that is the precursor to the working catalyst. We see clear differences in the nature of the as-prepared catalysts that can be related to the improved selectivity. EXAFS shows that Pd/C is fully reduced at 115°C and retains some metallic Pd character even after air exposure at room temperature. On Al_2O_3 and MgO, the Pd is fully oxidized at room temperature in air (as-prepared) and is not fully reduced even after treatment in flowing H_2 at 115°C. The carbon support is therefore changing the reduction potential of Pd. The bonding of Pd with carbon makes it more electron rich compared to the Pd on the oxide supports. The increase in the electron density on Pd (seen by a lower white line intensity in Figure 4.7) is probably what makes the bonding with the reactants different, and could make dissolution of H_2 less favorable, changing the activity and selectivity. Electronic modification of Pd was also suggested as the cause for improved selectivity in the recent work of Yang et al. [74]. Another notable feature shown by EXAFS is the Pd-C coordination in the reduced Pd/C sample. This can also be noted as a contributing factor in the selectivity enhancement.

Although our EXAFS results do not indicate carbon incorporation into the Pd lattice (the Pd-Pd distance in the reduced Pd/C sample remains 2.74Å), the beneficial effect of the carbon can arise through its interaction with the Pd. The long Pd-C bond suggests that the carbon atoms on the support are coordinated to the Pd, and similar long bonds have also been seen in the literature [59,75]. The low coordination number of the sub-nanometer particles used in this study indicates that each particle consists of only about 13 atoms [76]. With so few atoms in each particle, it is possible that we do not provide opportunity for the dissolution of hydrogen into Pd, due to the Pd-C bonding, avoiding the non-selective pathway that leads to formation of ethane.

4.6 Conclusions

We have deposited a narrow size distribution of Pd nanoparticles on 3 different supports, one carbon and two oxides (MgO and Al_2O_3), using identical synthesis methods and Pd precursor. This allows us to eliminate the effects that particle size, ligands, or capping agents may have on the reaction and allows us to isolate the role of the support. We have shown carbon-supported Pd is more selective towards the formation of ethylene during the hydrogenation of acetylene (in excess ethylene) than either Al_2O_3 or MgO supported Pd. The enhanced selectivity of the Pd/C sample can be explained by the presence of carbon in the coordination sphere of Pd as evidenced by the occurrence of Pd-C bonding shown by EXAFS. Due to the low Pd coordination of the ultra-small particles, the metal-support interaction is maximized and allows for carbon modification of the electronic properties of Pd as shown by XANES. The low Pd coordination and the increase in electron density due to carbon bonding are possible contributing factors for the enhanced selectivity of monometallic Pd supported on carbon.

5. The Role of CeO_2 Surface Facets on the Reactivity of Sub-Nanometer Pd for CO Oxidation

5.1 Abstract

In this study we have shown the ability to deposit a highly dispersed Pd species on both rod-shaped and cubical ceria morphologies. CO oxidation turn over frequencies for ceria supported catalysts are an order of magnitude higher than either bulk Pd or alumina supported Pd and the turn over frequency of ceria rod supported Pd is an order of magnitude higher than ceria cube supported Pd. High-resolution electron microscopy and X-ray absorption measurements show that there is no discernible difference between the Pd species on either the rod or cube shaped support in terms of size, average coordination number, or oxidation state. After reduction in CO, Pd on both rods and cubes form small nanoparticles slightly larger than 1nm. Redox studies show that the nanoshape of ceria support plays a role in the redox properties of Pd. Pd supported on ceria rods has the ability to be quickly oxidized and reduced, yielding a unique redox property not present in Pd supported on ceria cubes. It can be concluded that this unique redox property is what contributes to Pd/ceria rods unique ability to serve as a highly active catalyst for low temperature CO oxidation.

5.2 Introduction

Cerium oxide (ceria) is a rare earth compound that has a high oxygen storage capacity (OSC) and a unique redox property that consists of the ability to rapidly form and eliminate oxygen vacancies on its surface. The formation of an oxygen vacancy replaces a CeO_2^{4+} site with a reduced and more reactive CeO_2^{3+} site, as shown in Figure 5.1 below [77].

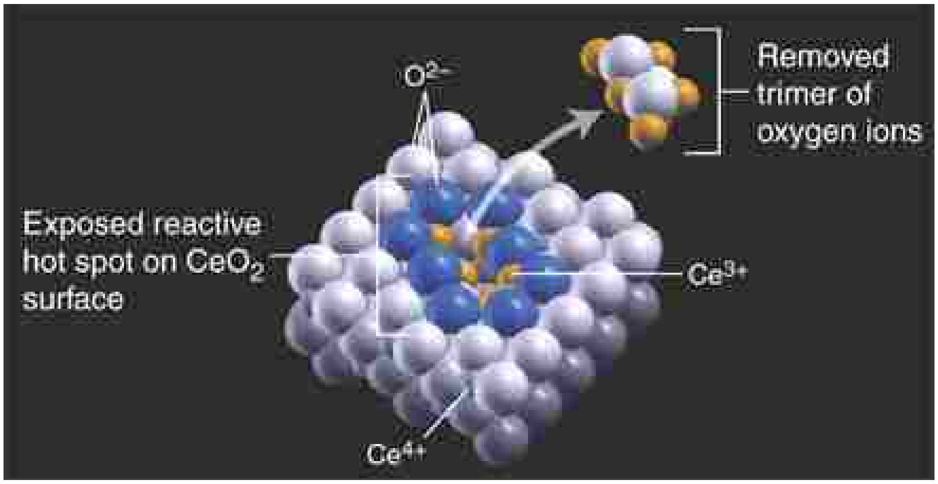

Figure 5.1 Schematic showing a CeO_2^{3+} site created by an oxygen vacancy [77].

Because of ceria's exceptional characteristics it is used in wide variety of applications such as a catalyst promoter in three-way automotive exhaust catalysts (TWC) [78], and as a solid electrolyte in electrochemical sensors [79,80] and fuel cells [81,82]. It is also an excellent catalyst support for noble metals, providing enhanced reactivity for water gas shift (WGS) and CO oxidation as compared to other commonly used oxides such as titania, alumina, and silica [83-86]. There is significant debate about the specific role of ceria in these reactions. Cargnello et al. [84] suggest that the perimeter atoms at the metal-ceria interface constitute the active sites for CO oxidation based on a correlation between the TOF and the number of active sites for a particular size and geometry of metal nanoparticles. Bunluesin et al. [83] found that CO oxidation activity is independent of metal particle size on ceria which is evidence that perimeter sites are not significant. They concluded that the migration of lattice oxygen from ceria to the metal is the factor contributing to the increased activity of ceria supported catalysts. In these studies the smallest metal particles considered were ~2.5 nm. As we make use of smaller, sub-nanometer particles that do not have a well-defined structure or geometry, it becomes increasingly difficult to investigate the nature of the active sites. Luo et al. [86] varied palladium (Pd) metal loading on ceria and found that 2-5wt% gave the highest activity at low temperatures for CO oxidation. They attributed this low temperature activity to an ionic Pd species as opposed to dispersed PdO or bulk PdO seen in the catalysts with higher metal loading. However, at the time this could not be fully investigated due to characterization technique limitations. This system could now be investigated more thoroughly with modern characterization methods.

Another aspect of ceria to be considered is the role of specific surface facets that can be exposed preferentially. The crystallographic faces of ceria, (111), (110), and (100) each exhibit different structure and composition. It has been shown that different ceria faces exhibit different properties such as oxygen storage capacity and polarity which may contribute to the activity differences. The (111) face has the lowest surface free energy and therefore is the most stable, while the (100) face has the highest surface free energy and is the least stable [87]. The different faces of ceria are shown in Figure 5.2, from most stable to least stable.

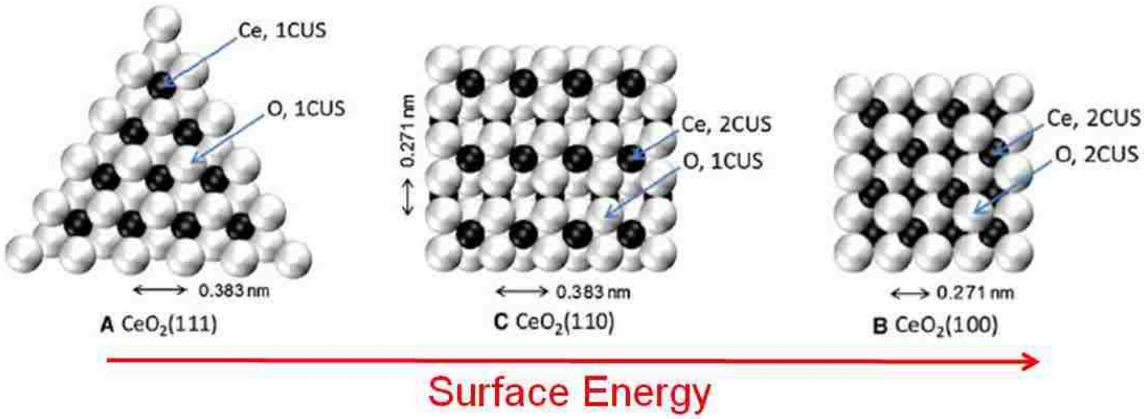

Figure 5.2 Schematic showing the different faces of ceria from most to least stable [87].

Previous studies have used single crystals and thin films of ceria to compare reactivity of different crystal faces [87,88]. Although these studies have given some insight into the fundamental differences of a specific faces behavior, the conditions during synthesis and characterization in these model studies and the low surface area of the samples are not realistic for real world catalysts. It has recently been shown that nano-shaped ceria particles (rods, cubes, and octahedra) can also preferentially expose different faces. The synthesis of these controlled morphologies is well developed and the resulting powder sample is practical to use as an industrial catalyst [89]. Studies have shown that these ceria shapes exhibit different reactivities for CO oxidation [90,91] and it is thought that this may be due to different crystallographic faces being exposed by each shape. Ceria cubes and octahedra preferentially expose the (100) and (111) faces, respectively and many studies suggest that rods expose (110) and (100) faces equally [90-92] (Mai 2005 J Phys Chem B,). Recent work in our group [93] was not able to detect any (110) facets in CeO_2 nanorods and we believe rods primarily expose the (111) face.

The goal of this research is to understand the role of the facets in ceria nanoshapes in modifying the reactivity of palladium for CO oxidation. This was done by first establishing that a similar Pd species is deposited on ceria cubes and ceria rods. Despite the similarity in Pd on the two supports, the resulting catalysts provide different reactivity for CO oxidation. Electron microscopy, X-ray absorption spectroscopy, CO-TPR and CO oxidation kinetics were used to show the difference in properties that a specific ceria facet provides to the palladium thereby increasing its activity for oxidation reactions.

5.3 Experimental Methods

5.3.1 *Preparation of supported catalysts*

Ceria rods and cubes were prepared through a hydrothermal treatment method developed by Mai et al. [89]. Cerium(III) nitrate hexahydrate (99.999% trace metals basis, Sigma-Aldrich) was used as the cerium source. A solution of 3.5g of cerium nitrate hexahydrate in 20 mL of DI water and a solution of 140 mL of 6M NaOH were mixed together and stirred for 30 minutes. This milky white solution was transferred to an autoclave with a Teflon liner and heated to 100°C and 180°C for 24 hours for rods and cubes, respectively. The sample was then washed in both DI water and ethanol several times and centrifuged in between each wash cycle. The washed and centrifuged sample was then dried overnight at 90°C in air.

Palladium was deposited on the ceria supports using a palladium tetraammine nitrate (10% aqueous solution, GFS Chemicals) precursor. Dry impregnation was used to reach 2wt% Pd on the ceria supports. After Pd deposition, the catalysts were calcined for 1 hour in air at 500°C at a ramp rate of 1°C/min.

Alumina supported Pd was used a reference catalyst for reactivity measurements. Boehmite alumina (Sasol Dispal) was calcined at 650°C for 10 hours to make γ-alumina.

The same method used for the ceria catalysts was used to deposit 2.5wt% Pd on the alumina. The Pd/Al_2O_3 sample was then calcined for 2 hours at 600°C in air.

5.3.2 *Electron microscopy*

A holey carbon copper TEM grid was dipped into a solution of the catalyst powder dispersed in ethanol. The Pd dispersion and ceria morphology were examined through transmission electron microscopy in a JEOL2010F operated at 200kV in both scanning transmission (STEM) and high-resolution (HR-TEM) modes. The Pd/ceria rods were further analyzed using an aberration corrected JEOL200F 200kV in high angle and medium angle annular dark-field STEM modes.

5.3.3 *Catalytic testing*

CO oxidation experiments used a micro-GC (Variant CP-4900) reactor system. 20mg of sample was packed between quartz wool in a U-tube reactor that was mounted in a temperature controlled oven. The samples were pre-oxidized in 7.5% O_2/He at 500°C for 1 hour. The sample was cooled to room temperature in the O_2/He mixture before introduction of the reaction gas mixture. The CO oxidation feed consisted of 1.5mL/min of CO, 1mL/min of O_2, and 75mL/min of UHP He. After introduction of reaction gases, the oven was heated to 300°C at a ramp rate of 2°C/min. The GC sampled the effluent gas approximately every 3 minutes.

CO temperature programmed reduction (CO-TPR) experiments were carried out in the same reactor system with a fresh sample. The samples were given the same pre-oxidization treatment, 500°C in a 7.5% O_2/He gas mixture, and then cooled to room temperature in He. The TPR feed consisted of 8.3mL/min of CO and 75mL/min of UHP He, the catalyst was heated to 300°C at 2°C/min.

5.3.4 *X-ray absorption spectroscopy*

In situ EXAFS measurements were performed at the Pd K-edge using the insertion-device beam line (10ID-B) of the Materials Research Collaborative Access Team (MRCAT) at the Advanced Photon Source at Argonne National Laboratory. 50mg of sample was mixed with 150mg of an inert silica powder and pressed into pellets. The pellets were placed in a continuous-flow EXAFS reactor cell that was mounted in a tube furnace. All spectra were taken in fluorescence mode with a Pd foil in the reference position. Spectra were taken of each catalyst in ambient conditions before the start of gas flow. 1% CO/He was flowed through the sample at room temperature at a flow rate of 50 sccm. Spectra at room temperature were taken and then the temperature was ramped to 200°C at 2°C/min in flowing CO while spectra were taken approximately every 2 minutes. The gas flow was switched to 100 sccm of 5% O_2/He and cooled to room temperature in an attempt to re-oxidize the sample that was reduced in CO. Spectra were taken in O_2 at room temperature. The temperature was increased to 40°C, spectra were taken in O_2 and then the gas flow was switched to the previous CO flow and spectra were taken in CO at temperature. This procedure was repeated at approximately 70°C and 100°C to analyze the redox properties of the catalysts. EXAFS measurements were done for both the rod and cube samples.

Experimental EXAFS data $\chi(k)$ (where k is the photoelectron wave number) were processed by subtracting the background from the normalized absorption coefficient using the Athena [61] program of the IFEFFIT data analysis package [62]. The theoretical EXAFS signal was constructed using the FEFF6 code [63] and fitted to the data in r-space using the Artemis [61] program of the IFEFFIT package. S_0^2 (the passive electron reduction factor) was obtained by first analyzing the Pd foil, and the best fit value (0.78) was fixed during the fitting of the catalyst samples. The spectra were fitted in r-space by varying the coordination number of the single scattering path, the bond length disorder (Debye-Waller factor), σ^2, the effective scattering length (R), and the correction to the threshold energy, ΔE_0. The k-range used for Fourier Transform of the $\chi(k)$ was 3−10 $Å^{-1}$ and the r-range for fitting was 1.0-3.0 Å. XANES analysis was also done using Athena by performing a linear combination fit. Because of the small size of the particles, they cannot be properly represented by bulk standards for the linear combination fitting. Fully reduced Pd nanoparticles supported on ceria and the as-prepared Pd on ceria were used for the standards for XANES analysis.

5.4 Results and Discussion

5.4.1 *Microscopy*

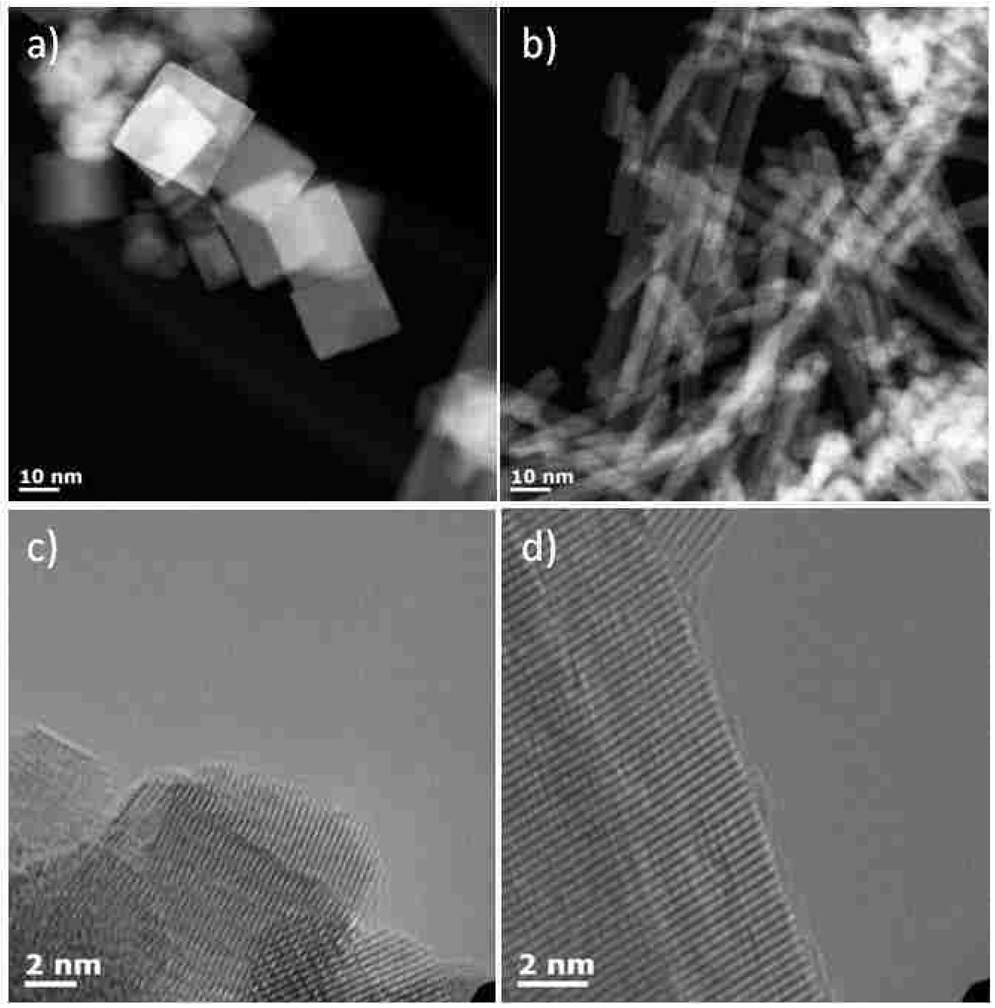

Figure 5.3 a) STEM image of ceria cubes, b) STEM image of ceria rods, c) HR-TEM image of 2wt%Pd/ceria cubes, d) HR-TEM image of 2wt%Pd/ceria rods

Scanning transmission electron microscopy (STEM) images of ceria cubes and ceria rods are shown in Figure 5.3a and 5.3b. Both the cubes and rods are well defined and have BET surface areas of 50 and 90 m^2/g, respectively. Figure 5.3c and 5.3d show high resolution transmission electron micrographs (HR-TEM) of 2wt% Pd on ceria cubes and rods, respectively. These images are representative of the samples and show that there is no visible Pd despite their high metal loading. This indicates the Pd is very highly dispersed in the form of small clusters or possibly single atoms. In order to further investigate the Pd dispersion on ceria rods, this sample was examined through aberration-corrected TEM that has a much higher resolution and the capability to resolve single atoms. Figure 5.4 shows bright field and high-angle annular dark field (HAADF) images of the edge of a ceria rod with 2wt% Pd, Pd particles are not seen in either mode. It should be noted that the resolution of these images allows the ceria lattice to be clearly resolved. The image contrast in HAADF is atomic number dependent (~$Z^{1.7}$), therefore heavier elements appear brighter. The contrast is also dependent on the thickness of the sample the electron beam is transmitting through. A thicker region of a sample will appear with more contrast than a thinner region that is of the same composition. Because of how we see contrast in HAADF images, it would be difficult to detect a single atom or cluster of atoms of Pd on a ceria support considering the ceria is much heavier than Pd and the amount of ceria (~10nm) the beam is going through is an order of magnitude greater than that of Pd.

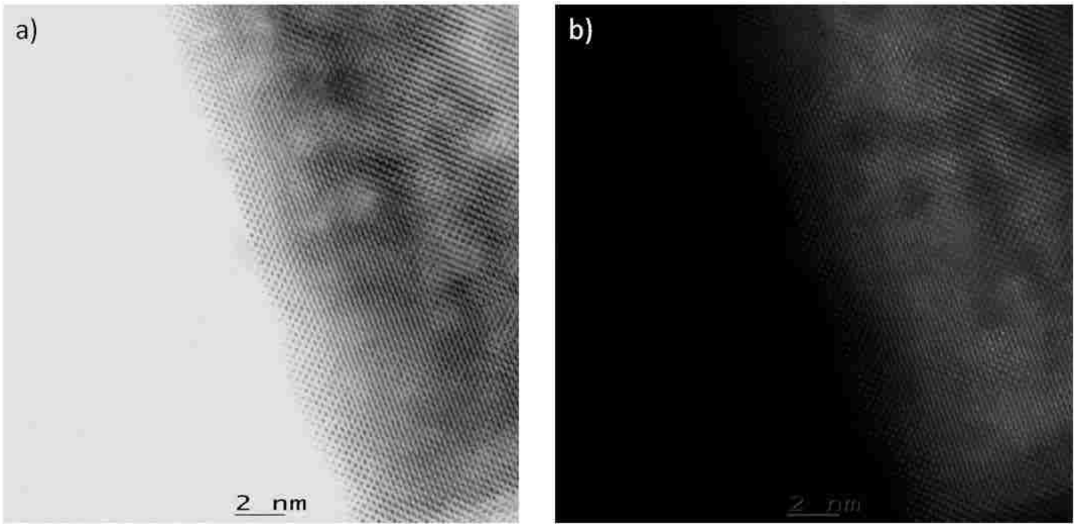

Figure 5.4 TEM images of 2wt%Pd/ceria rods a) bright field b) high-angle annular dark field (HAADF)

As mentioned previously, it has been reported many times that rods expose the (110) and (100) faces equally. In our work, we were never able to detect the (110) faces exposed, rather we mainly saw the (111) face being exposed. Figure 5.5 shows a rod exposing the (111) face. The lattice fringes run down the length of the rod and index to 3.17Å. This is evidence that rods have previously not been indexed properly and ceria rods primarily exposed the (111) face. It should also be noted that ceria rods contain many defects that are seen as areas of lighter contrast in Figures 5.3, 5.4, and 5.5. This is quite different from ceria cubes that expose the (100) face and have smooth faces.

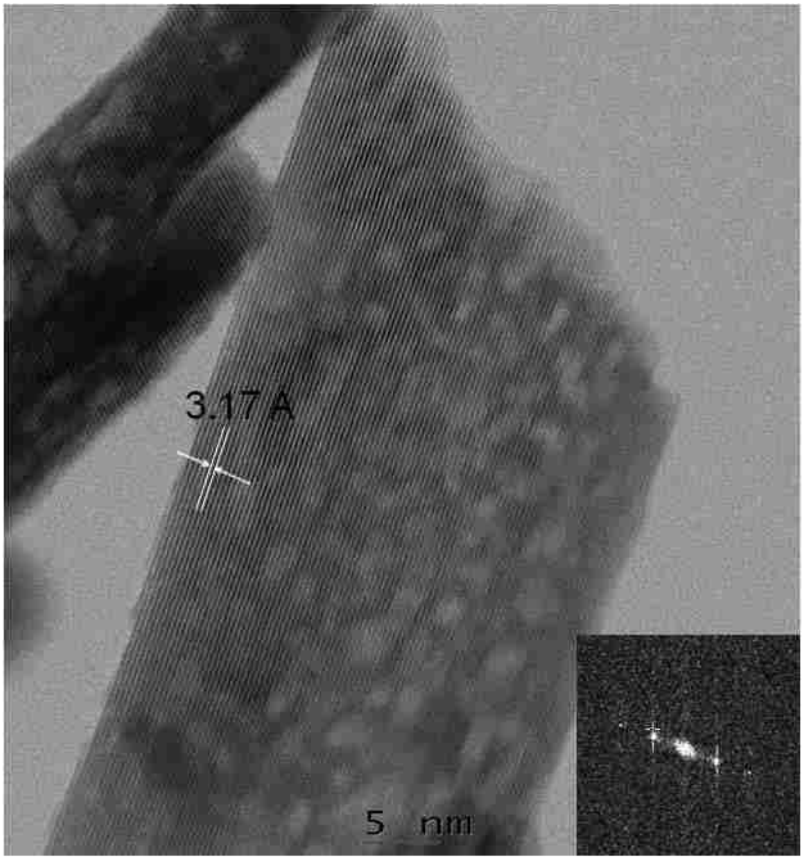

Figure 5.5 HR-TEM image of ceria rod showing the lattice fringes index to 3.17Å (111).

5.4.2 *CO Oxidation*

The bare ceria supports were tested for CO oxidation and in both cases, the ceria becomes active for CO oxidation at about 150°C and reaches 100% CO conversion by 300°C. Bare ceria is slightly active as an oxidation catalyst but this activity can be greatly increased by the addition of a noble metal.

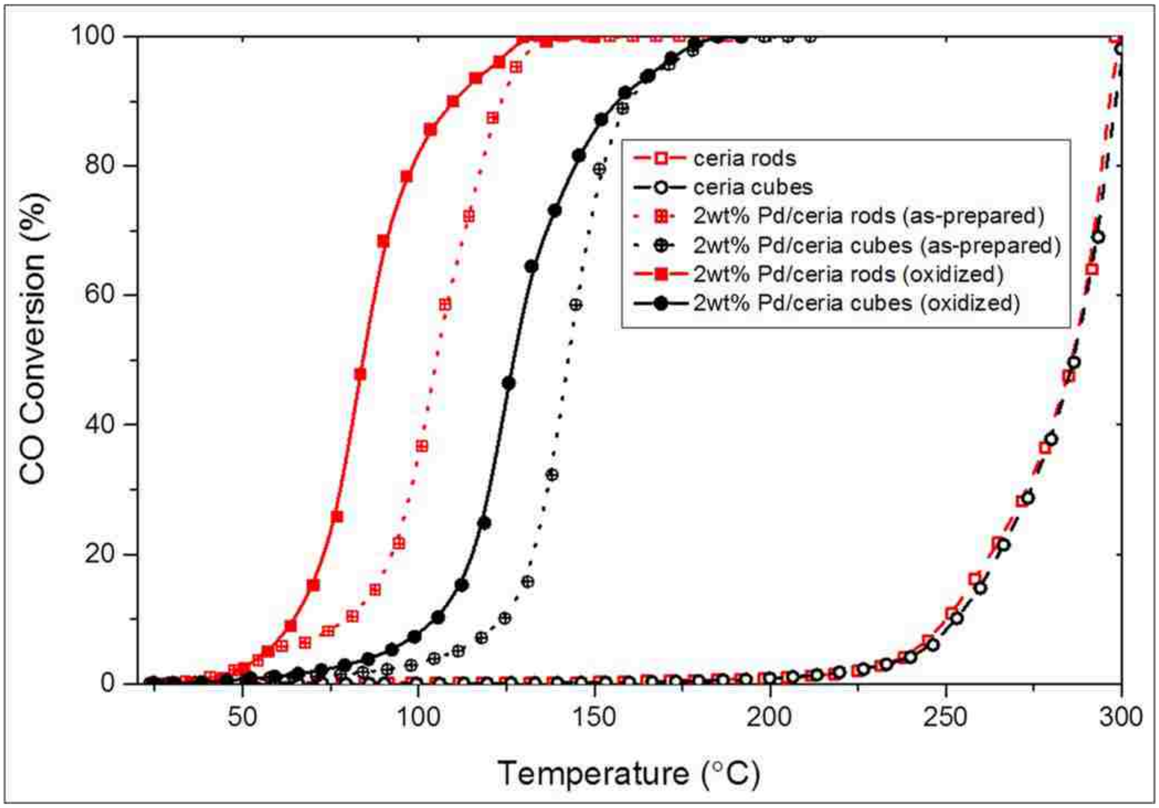

Figure 5.6 CO conversion vs. temperature for bare ceria, 2wt%Pd/ceria (as-prepared), and 2wt%Pd/ceria (oxidized).

The deposition of 2wt% Pd greatly increased the activity of the catalyst; the as-prepared Pd/ceria rods show activity at temperatures as low as 50°C whereas the bare ceria rods are completely inactive at that temperature. The as-prepared Pd/ceria rods reach full CO conversion by 150°C and the bare ceria rods full conversion isn't reached until 300°C.

We also found that giving the catalyst an *in situ* oxidation treatment at 500°C further increased the activity of the catalyst compared to the as-prepared sample. The as-prepared samples are calcined in air at 500°C so this *in situ* oxidation is not simply decomposing residuals from precursors or cleaning the surface of the catalyst. The structure of the catalyst is somehow changed by this *in situ* oxidation because doing this same treatment and then exposing the catalyst to ambient conditions yields very different results.

Figure 5.6 shows the CO oxidation light-off curves for the bare ceria, as-prepared Pd/ceria, and oxidized Pd/ceria for both the rod and cube supports. The two bare ceria supports are very similar to each other in terms of reactivity but the addition of Pd changes this. After the addition of Pd, the light-off temperature of the catalysts decreases by more than 150°C. The graph also shows that the *in situ* oxidation treatment further decreases the light off temperature for both the rod and cube supports. Although the rod and cube supports exhibit the same trend in increasing activity, the Pd/rods catalyst is more active than the cubes in both the as-prepared and oxidized states.

The turn over frequencies (TOF) were calculated assuming that the Pd was 100% dispersed on the ceria. These values are compared to both bulk Pd metal and 2.5wt% Pd/Alumina in Table 5.1. The table shows that the TOFs of ceria supported Pd are orders of magnitude higher than their on non-ceria supported counterparts.

Table 5.1 CO oxidation TOFs for 2wt%Pd/ceria compared to bulk Pd and Pd/alumina at 70°C

Catalyst	TOF (s^{-1})
bulk Pd metal	0.000130
2.5wt% Pd/alumina	0.000640
2wt% Pd/ceria rods	0.045000
2wt% Pd/ceria cubes	0.002200

This difference in activity is not due to the support itself because both the bare rods and bare cubes show similar activity and neither is active at these low temperatures. Also, this isn't simply a size effect of the Pd nanoparticles as the Pd size for both ceria supports is below the resolution limits of an aberration corrected microscope. The ACEM gives evidence that the Pd must be in the form of single atoms or small clusters on both the ceria rods and ceria cubes.

5.4.3 *EXAFS*

As shown previously, the Pd particles are too small to be detected by electron microscopy so x-ray absorption experiments were done to ascertain if any differences in Pd species or oxidation state were present. Figure 5.7 shows EXAFS spectra at the Pd k-edge of the as-prepared samples in r-space at room temperature in air along with a bulk PdO (Aldrich) sample for comparison. The Pd signal given by both samples is nearly identical and shows Pd-O bonding is very similar to the bulk PdO reference sample. The data is not phase corrected so the 2Å Pd-O bond shows up on the graph at ~1.5Å. The as-prepared samples first shell is fully coordinated with four Pd-O bonds. Neither sample shows evidence of Pd-Pd bonding, indicating that there is no Pd metal present. The bulk PdO reference shows a second shell at ~3 Å which is not present in the as-prepared samples. The absence of a second shell indicates a lack of long range order and indicates that the Pd is present in the form of a highly dispersed species. This figure gives critical information about the as-prepared catalyst, indicating that, initially, there is little to no difference in the Pd supported on either ceria rods or cubes and that it is in the form of a highly dispersed, isolated species.

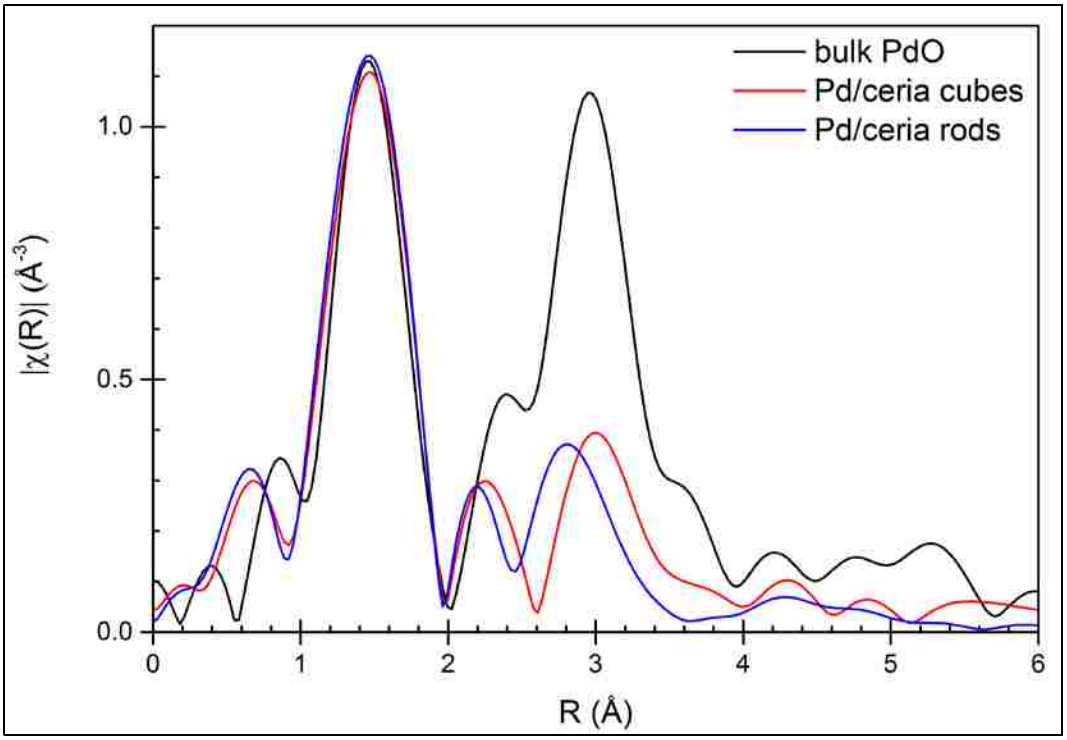

Figure 5.7 Fourier transform magnitudes of the k^2-weighted $\chi(k)$ data for the Pd-K edge EXAFS spectra of the as-prepared Pd/ceria rods and Pd/ceria cubes compared to bulk PdO.

Both CO-TPR and redox studies were performed in the EXAFS beamline. To aid in the understanding of the experimental procedure, a schematic of temperature vs. time is shown in Figure 5.8. The color of the line indicates the gas environment that the sample was exposed to and the open circles indicate when an EXAFS spectrum was obtained during the experiment.

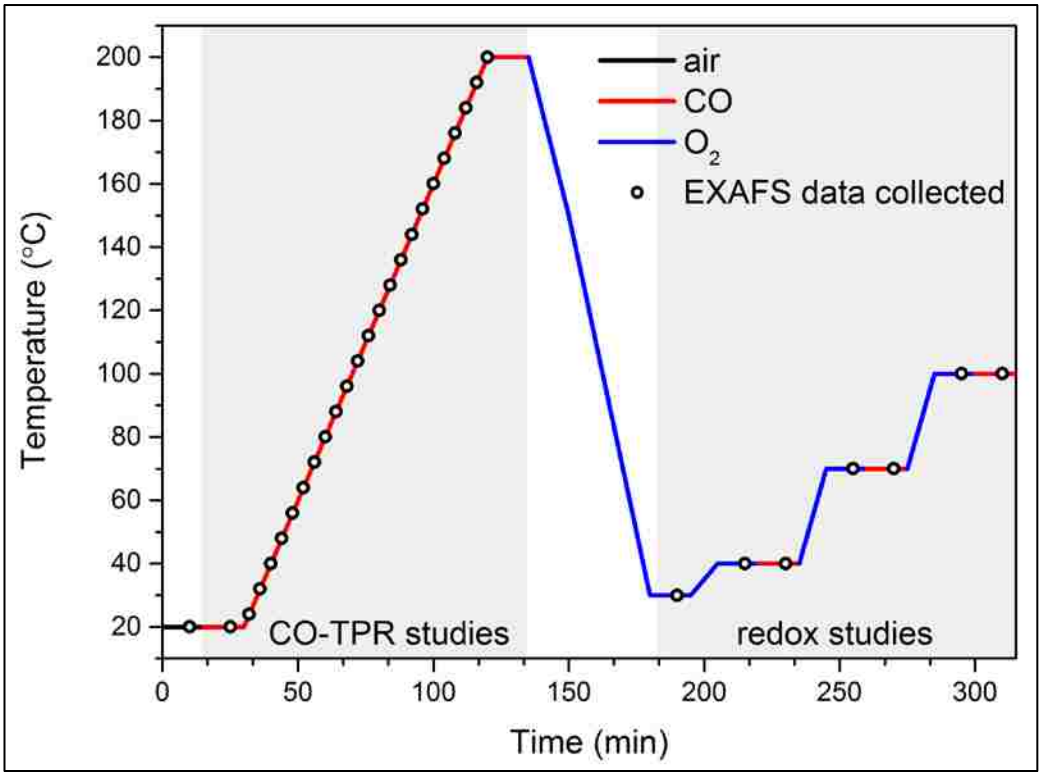

Figure 5.8 Schematic showing the experimental procedure during EXAFS experiments for CO-TPR and subsequent redox studies.

In situ CO-TPR in the EXAFS beamline was run up to 200°C. During the CO-TPR run, both the rod and cube supported samples slowly began to form Pd-Pd bonds as the Pd-O bonding decreased. Figure 5.9 shows the samples at 200°C in flowing CO. At this point, the spectra were no longer changing with increasing temperature and the samples were fully reduced. The data is not phase corrected and the 2.75Å Pd-Pd bond shows up at ~2.5Å in the graph. The spectra of the rod and cube samples are again very similar to each other, indicating there is little to no difference in the Pd after a reduction in CO. Pd foil is also shown in the graph as a reference. Bulk Pd is fully coordinated with 12 Pd-Pd bonds. The smaller amplitude of the Pd-Pd bond peak in the samples shows that the Pd in under-coordinated and is present in the form of nanoparticles. The Pd on the rods and cubes has Pd-Pd coordination numbers of 7.9 and 7.4, respectively. As shown previously, coordination number can be correlated with nanoparticle size and these coordination numbers correspond with Pd nanoparticles of about 1.4 nm for rods and 1.2 nm for cubes, after reduction in CO at 200°C. The EXAFS data tells us that the starting and ending states of Pd for the two catalysts are the same. Initially, the Pd is only bound to O and is present in the form of a highly dispersed species. After reducing the samples in CO at 200°C, there is little if any Pd-O bonding and the Pd has formed nanoparticles that are slightly larger than 1 nm. This information tells us that the working state of the catalyst must yield the differences in activity seen.

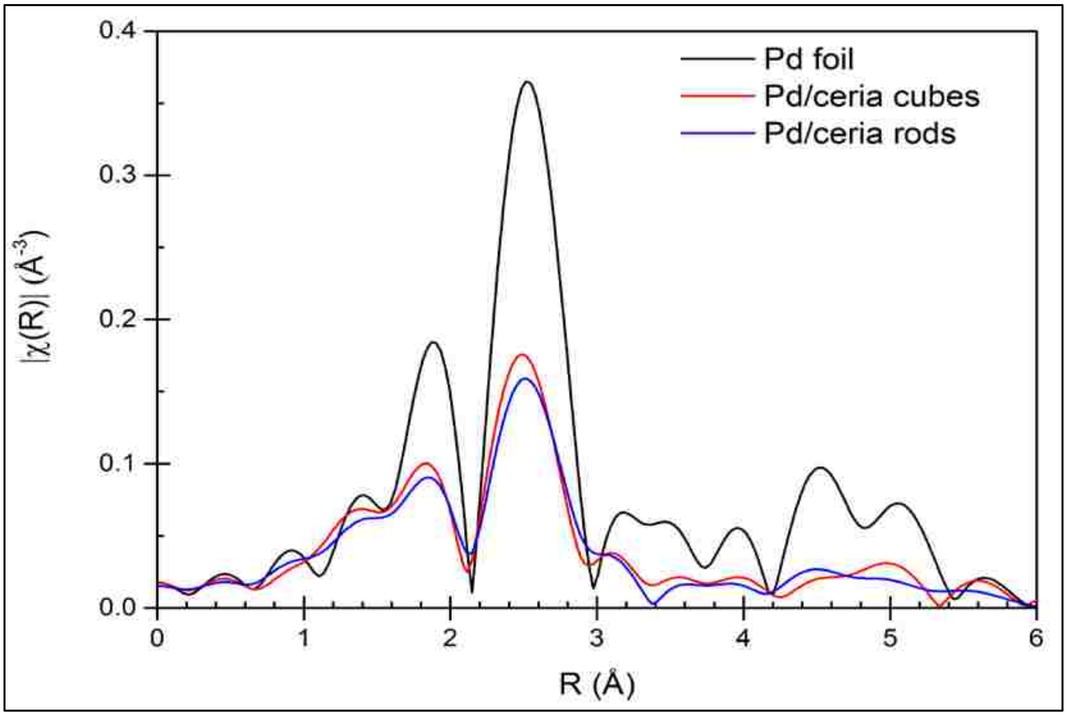

Figure 5.9 Fourier transform magnitudes of the k^2-weighted $\chi(k)$ data for the Pd-K edge EXAFS spectra of Pd/ceria rods and Pd/ceria cubes at 200°C in CO compared to bulk Pd.

XANES data was acquired during the *in situ* CO-TPR to help understand CO absorption on the catalyst. From the EXAFS data, we saw that the as-prepared catalyst was completely oxidized and did not contain any Pd metal. A linear combination fit was performed on spectra at about every 10°C as the catalyst was exposed to CO while the temperature was ramped to 200°C. Because the Pd was in the form of a very highly dispersed species on the ceria, using bulk PdO and bulk Pd as the fitting standards in the linear combination fit would not provide accurate results. The spectra of the as-prepared and the fully reduced catalysts were used as the reference standards for linear combination fitting. We are confident that the two end points contain fully oxidized and fully reduced small particles of Pd. After being exposed to CO, the Pd on both supports began to reduce and form metal.

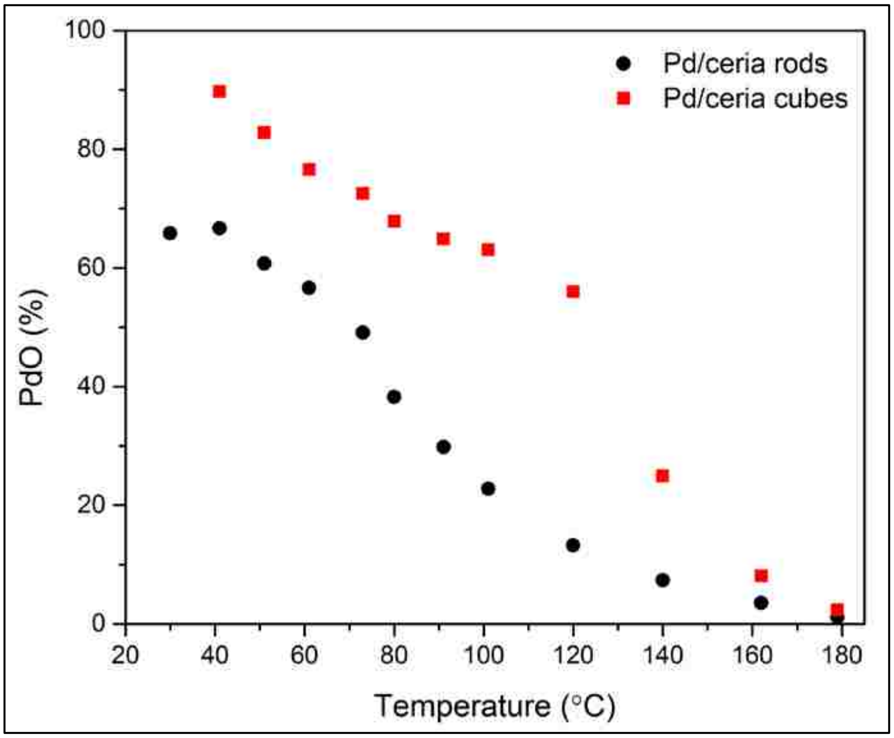

Figure 5.10 %PdO obtained from a linear combination fit of XANES data as a function of temperature in flowing CO for Pd/ceria rods and Pd/ceria cubes.

By 200°C, the spectra were unchanged by higher temperatures and it was concluded the Pd in both of the samples was fully reduced. The percentage of PdO from XANES is shown as a function of temperature during the CO-TPR run in Figure 5.10. The Pd on the ceria rods was reduced at lower temperatures than on the ceria cubes.

After the CO-TPR run, oxygen was flowed at 200°C to test the re-oxidation properties of the catalyst. The figure below shows the EXAFS results in r-space. Figure 5.11a shows the Pd/ceria rods as-prepared, after CO-TPR at 200°C, and after re-oxidization at 200°C.

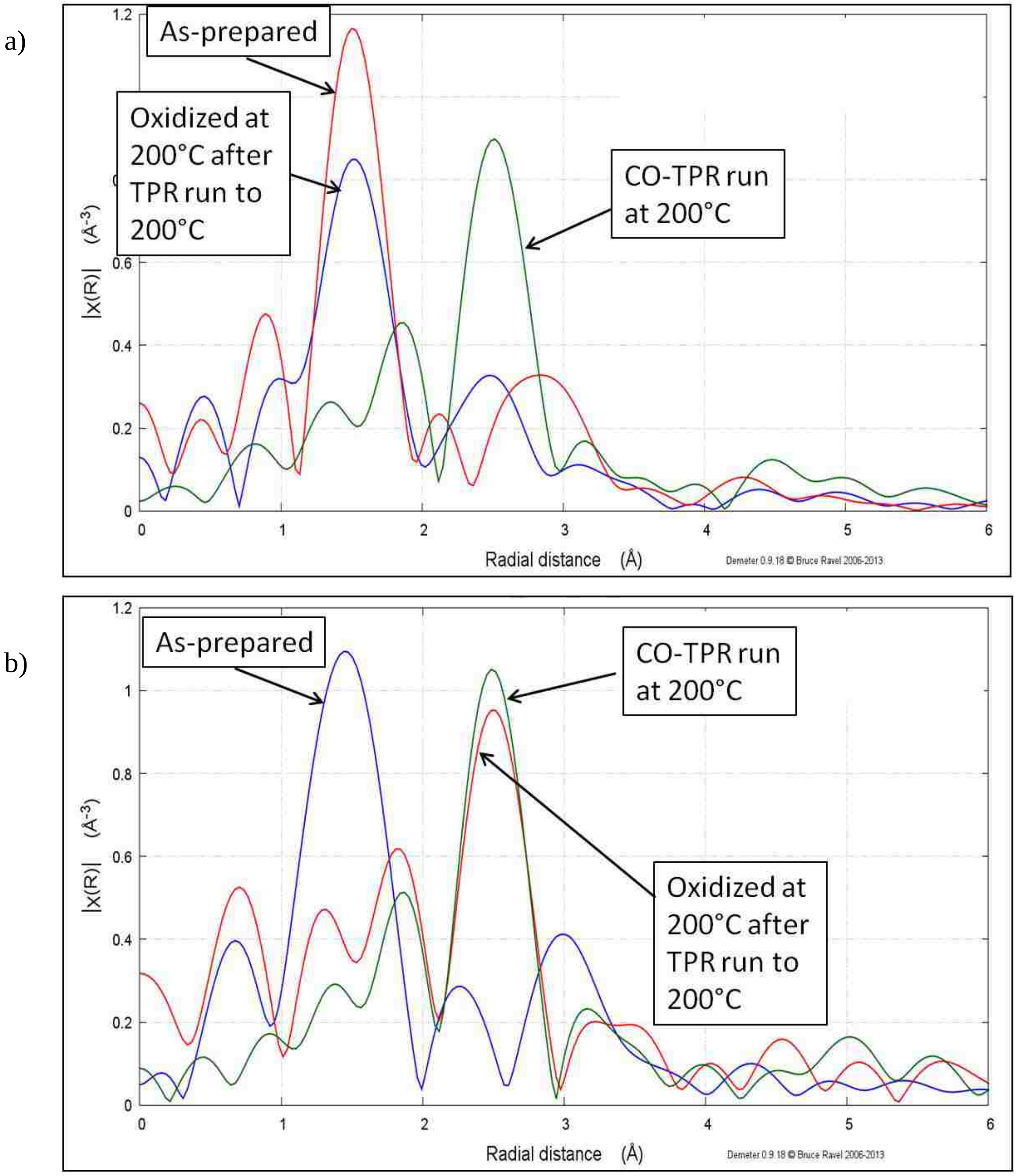

Figure 5.11 Fourier transform magnitudes of the k^2-weighted $\chi(k)$ data for the Pd-K edge EXAFS spectra of Pd/ceria, as-prepared, at 200°C in flowing CO, and re-oxidation at at 200°C. a) rods, b) cubes.

As already seen, the as-prepared catalyst shows a highly dispersed phase of PdO and after the TPR run shows nanoparticles of metallic Pd. After a subsequent oxidation, Pd on the rod catalyst is re-oxidized and almost returns to the original as-prepared state. There is no longer any Pd-Pd bonding and only Pd-O bonds are present. Figure 5.11b shows the same scenario for the Pd/ceria cube catalyst except that oxidation treatment after TPR did not re-oxidize the Pd. After the oxidation, the catalyst remains almost unchanged and exhibits only Pd-Pd bonding and no Pd-O bonding. This is proof that not only are the redox properties of the ceria itself different, but the ceria has the ability to change the redox properties of the metal supported on it. To further investigate this phenomenon, these catalysts were reduced in CO and oxidized at increasing temperatures to understand the effect of temperature on the redox properties.

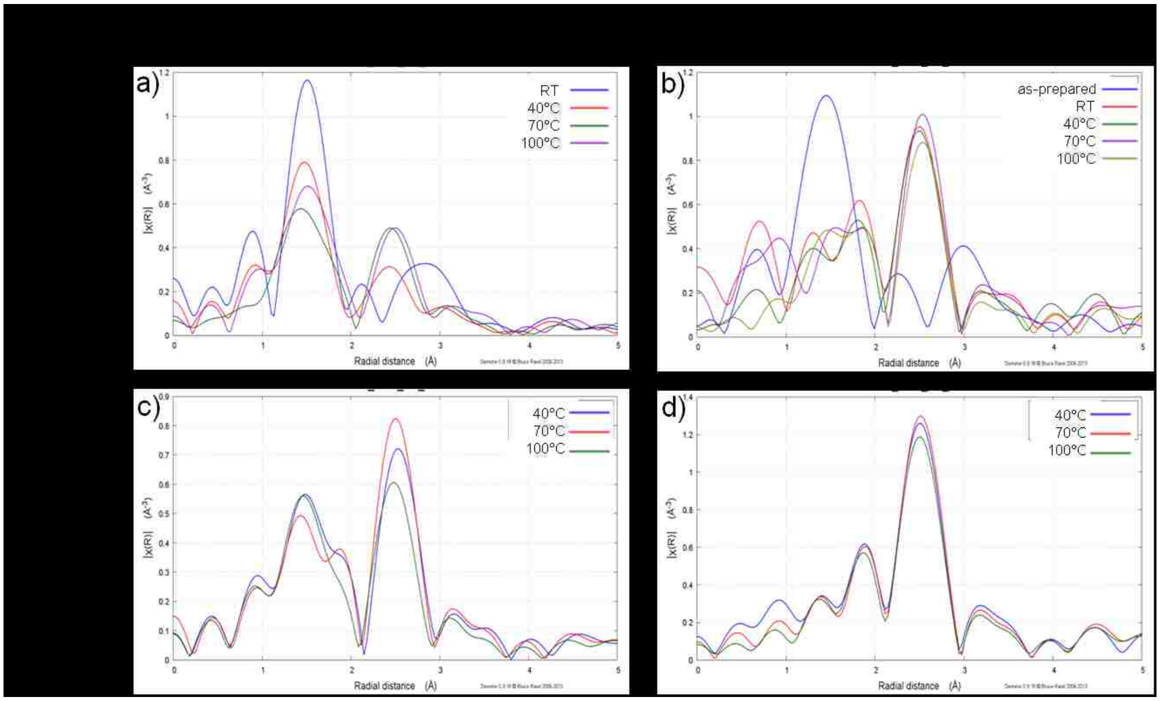

Figure 5.12 Fourier transform magnitudes of the k^2-weighted $\chi(k)$ data for the Pd-K edge EXAFS spectra during redox studies of Pd/ceria rods and Pd/ceria cubes at 40°C, 70°C, and 100°C.

These redox studies were done at 40°C, 70°C, and 100°C and the experimental procedure is illustrated in Figure 5.8. Figure 5.12a and 5.12c show the rod data and

5.12b and 5.12d show the cube data. Figure 5.12a and 5.12b are in flowing O_2 and 5.12c and 5.12d are in flowing CO. The rods show Pd-O bonding in flowing O_2 and Pd-Pd bonding in flowing CO at all temperatures. This indicates that the Pd on ceria rods has the ability to easily reduce and oxidize at these temperatures. In contrast, the cubes show very different Pd redox behavior. The Pd on cubes is reduced in CO by 200°C but doesn't have the ability to re-oxidize in O_2 even at temperatures as high as 100°C.

The EXAFS and XANES data gives us unique insight into the redox properties of Pd supported on ceria. It has been previously shown that ceria has unique redox properties and we have shown that this property can be transferred to the metal in specific cases.

5.4.4 *CO-TPR*

CO-TPR studies were done in the same system used for our reaction studies in order to quantify how much CO was being consumed and how much CO_2 was being produced during a TPR run since we did not have the capabilities to run the EXAFS experiments *in operando*. Since we suspected that these catalysts would be slightly active at room temperature, CO was first flowed without any heat. Figure 5.13 shows the CO_2 peak area acquired from the GC for both the rod and cube samples as a function of time along with the temperature profile included in the right y-axis. The first 12 min of the experiment was done without flowing CO in order to establish a baseline for the peak areas and to ensure there were no trace amounts of gases in the reactor lines. CO is introduced to the system at ~12 minutes and CO_2 is immediately produced in both samples at room temperature. As the CO_2 produced by the catalysts decreased, the temperature was increased as it was in the EXAFS runs. We see that although both catalysts produce CO_2, the rods produce far more both at room temperature and at elevated temperatures. The rods also begin to produce CO_2 at temperatures slightly lower than the cubes. This verifies our previous results and allows us to understand not only do Pd/ceria rods allow for the conversion of CO to CO_2 at lower temperatures but it also has the ability to convert CO at room temperature.

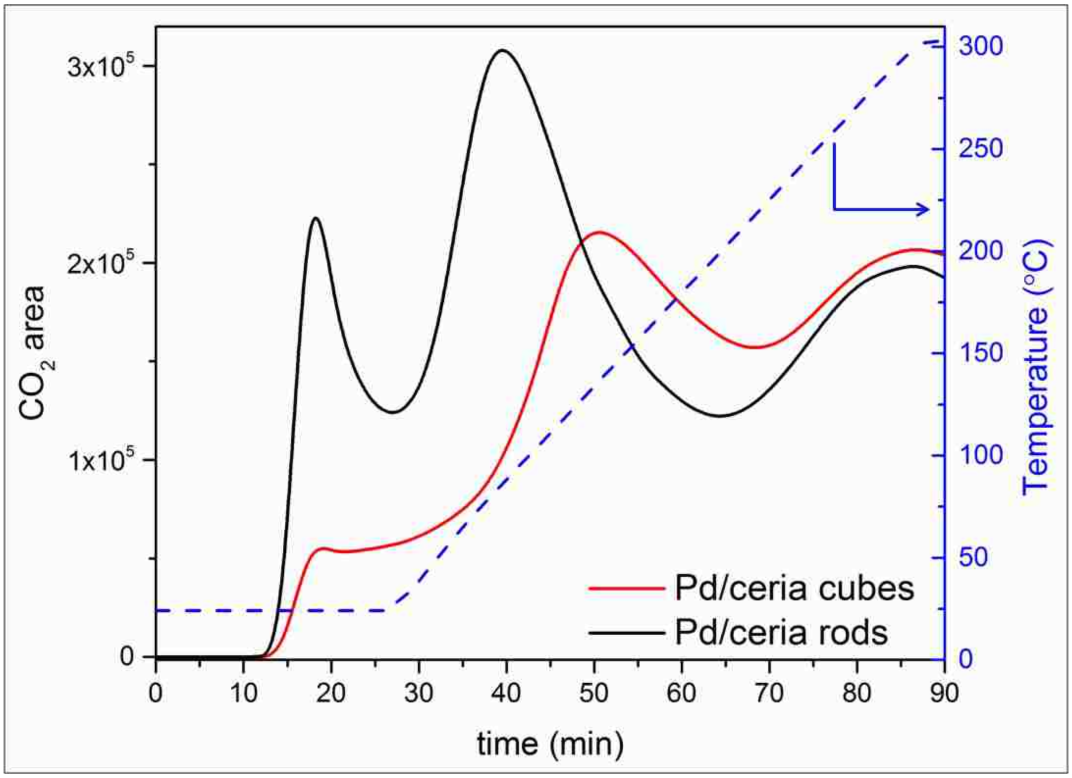

Figure 5.13 Comparison of CO_2 produced during CO-TPR both at room temperature and at temperatures up to 300°C for Pd/ceria rods and Pd/ceria cubes.

5.5 Conclusions

We have deposited a highly dispersed Pd species on two different ceria supports, rods and cubes. Electron microscopy shows that even with atomic resolution, the Pd is not visible on the ceria. EXAFS shows that the precursor to the catalysts is very similar on both supports and is the form of a highly dispersed oxidized form of Pd. EXAFS also shows that the Pd on both supports are in the form of fully reduced, ~1nm, nanoparticles after a reduction in CO at 200°C. XANES shows a clear difference in the reducibility of the Pd on the two supports with the Pd on ceria rods is more easily reduced than on ceria cubes. Redox studies at several temperatures show that Pd supported on ceria rods can easily go between oxidized and reduced states, even at low temperatures while this is not the case for Pd/ceria cubes. The unique redox properties of Pd/ceria rods can help explain the high activity for CO oxidation at low temperatures.

While there are interesting findings in this study, it also leaves room for much more investigation. We have shown that ceria rods provide Pd with a unique redox property that is much different than Pd supported on ceria cubes. The most obvious difference between the rods and cubes are the exposed crystal facets and the presence of defects in rods. Further investigation would give insight into if either or both of these factors are contributing to the different in activity for CO oxidation.

6. Conclusions

A systematic study was performed by varying the amount of nucleation sites on a support in order to determine how these sites played a role on the dispersion of a catalyst. Various synthesis methods, such as impregnation, colloid deposition, deposition-precipitation, and alcohol reduction were employed in order to produce catalysts that were best suited for each system. Electron microscopy and X-ray absorption spectroscopy were used to gain information about the characteristics and structure of supported metal nanoparticles. Acetylene hydrogenation and CO oxidation were used as probe reactions to test the selectivity and activity of the synthesized catalysts.

We gained insight into the sintering mechanisms of nanoparticle systems in which anomalously large particles are formed. We now know that this can occur during Ostwald ripening and the anomalously large particles lie far out of the range of the log normal distribution that has been proposed for this sintering mechanism. This *in situ* study has also ruled out the possibility that these large particles were formed in areas of a locally high concentration of particles.

We found that the morphology of a mixed oxide support can play a role in the stabilization of nanoparticles at high temperatures. This idea and method of synthesis used to investigate flat samples was also successfully applied to powder catalyst supports. While there is still work to be done to understand the exact nature of the differences in support, this is a step forward in applying concepts learnt about inhibiting sintering of nanoparticles and deactivation of catalysts from flat, model samples to more practical catalysts.

We also investigated the role a support can have through its interaction with metal particles in a reaction. We found that by using mono-dispersed sub-nm Pd species, we could carefully study the role of the support in both hydrogenation and oxidation reactions.

These studies have addressed both synthesizing and maintaining a highly dispersed catalyst in order to maximize reactivity. Atomic scale aspects of nanoparticles were investigated to determine how small differences effected reactivity. While these studies have many interesting finding that can advance the field of heterogeneous catalysis by learning how to optimize a catalyst, it has also brought many questions that will lead to additional fascinating studies.

7. Appendix A

7.1 Mears analysis for external mass diffusion

A Mears analysis was performed to ensure that mass diffusion limitations were not encountered during reaction conditions for our palladium on alumina samples. The hydrocarbon feed into the reactor consisted of 0.5% acetylene, 35% ethylene, and the balance nitrogen at a flow rate of 66mL/min. Hydrogen was fed into the reactor at 1.4mL/min. We present the results of the analysis for the industrial look-alike 0.05 wt% Pd/α-alumina catalyst. 400mg of catalyst sample was used and the temperature was varied from room temperature to 160°C. The temperature was held constant while 5 runs were performed, then the temperature was raised by 10°C. We collected reactivity data for the sample while heating and also while cooling.

The Mears criterion to exclude mass transfer limitations is:

$$\frac{k'_1 R_p}{k_c} < 0.15$$

where

k'_1 : measured (pseudo-first order) reaction rate constant(sec^{-1})
R_p: particle radius (m)
k_c: gas-solid mass transfer coefficient (m/s)

$$k_c \sim \frac{\mathcal{D}_{acetylene-nitrogen}}{\delta}$$

Where

$\mathcal{D}_{\text{acetylene-nitrogen}}$: diffusion coefficient of acetylene in nitrogen
δ: boundary layer thickness

$$\mathcal{D}_{\text{acetylene-nitrogen}} = 2.19 \times 10^{-5}\ \frac{m^2}{s} \text{ at } 140°\text{C}$$

$$\delta = 47 \times 10^{-6}\ \text{m}$$

(δ is an upper bound based on the empty space between closely packed 150μm catalyst particles)

then

$$k_c = \frac{2.19\ \times 10^{-5}}{47 \times 10^{-6}} = 0.47\ \frac{\text{m}}{\text{s}}$$

Pseudo first order reaction rate constant for the acetylene reaction

$$\frac{dC_A}{d\tau} = -k\ C_A$$

$$\ln\left(\frac{C_A}{C_{A0}}\right) = -k\tau$$

Where $\tau = \frac{W}{\rho_b \cdot v}$

$$k = \frac{-ln(1-x)\ \cdot \rho\ \cdot\ \nu}{W}$$

From the reactivity data of Pd/Al_2O_3, the acetylene conversion at 140°C is 77%.
The bulk density of the catalyst is

$$\rho_b = 830\ \frac{\mathrm{kg}}{\mathrm{m}^3}$$

The volumetric flow rate of the reactants is

$$\nu = 2.5\ \times\ 10^{-6}\ \frac{m^3}{s}$$

$$k'_1 = \frac{-\ln(1-.77)\ \cdot 830\ \cdot 2.5\ \times\ 10^{-6}}{4\ \times\ 10^{-4}} = 7.6\ sec^{-1}$$

Substituting these values into the Mears criterion gives

$$\frac{k'_1 R_p}{k_c} = \frac{7.6\ \times 150\ \times 10^{-6}}{0.47} =\ 0.0024\ <<\ 0.15$$

So we can conclude that our system is free of external concentration gradients between the catalyst particle surface and the fluid bulk. Since the other catalysts are less reactive, they will also satisfy the Mears criterion for absence of mass transfer limitations.

7.2 Mears analysis for interphase heat transfer limitation

A Mears analysis was also performed to ensure that heat transfer limitations were not encountered during reaction conditions for our palladium on alumina samples.
Mears analysis to exclude interphase heat transfer limitations:

$$\frac{|\Delta H_R|\ \mathcal{R}\ \mathrm{R_p}\ E_a}{R_g\ h\ T_0^2} < 0.15$$

where

ΔH_R: heat of reaction (J/mol)
$\mathcal{R}$: measured rate of reaction per particle volume
R_p: particle radius
E_a: activation energy
R_g: ideal gas constant
h: gas-solid heat transfer coefficient
T_0: temperature of bulk fluid

$$\Delta H_R = -172\ \times\ 10^3\ \frac{J}{mol}$$

$$R_p = 150\ \times\ 10^{-6}\ m$$

$$E_a = 39.6 \times 10^3 \ \frac{J}{mol}$$
$$R_g = 8.314 \ \frac{J}{mol}$$
$$T_0 = 140℃ = 413K$$

The measured rate of reaction per particle volume can be calculated from:

$$\mathcal{R} = k_1' C_{C_2H_2}$$

Where $C_{C_2H_2}$(concentration of acetylene at reactor inlet) = 0.1 $\frac{mol}{m^3}$

$$\mathcal{R} = 7.6 \times 0.1 = 0.76 \ \frac{mol}{m^3 \cdot s}$$

The heat transfer coefficient can be calculated from:

$$h = \frac{2\,\lambda_g}{d_p}$$

where

λ

$\lambda_{g:}$ thermal conductivity of the gas

$$\lambda_g = y_{C_2H_2}\lambda_{C_2H_2} + y_{C_2H_4}\lambda_{C_2H_4} + y_{N_2}\lambda_{N_2} + y_{H_2}\lambda_{H_2}$$

$$\lambda_g = 0.005(52) + .343(60) + .632(42) + .021(250) = 53\frac{mW}{m \cdot K} = 53 \times 10^{-3} \ \frac{W}{m \cdot K}$$

$$h = \frac{2 \times 53 \times 10^{-3}}{150 \times 10^{-6}} = 707 \ \frac{W}{m^2 \cdot K}$$

Substituting these values into the Mears criterion gives

$$\frac{172 \times 10^3 \times 0.76 \times 150 \times 10^{-6} \times 39.6 \times 10^3}{8.314 \times 707 \times 413^2} = 0.0078 \ll 0.15$$

From this calculation we can conclude that our system does not suffer from interphase heat transfer limitations.

8. References

[1] I. Chorkendorff, Concepts of Modern Catalysis and Kinetics, 2nd ed., Wiley-VCH, n.d.

[2] J. Brunelle, Pure Appl. Chem. 50 (1978) 1211.

[3] H.A. Benesi, R.M. Curtis, H.P. Studer, J. Catal. 10 (1968) 328.

[4] A.M. Karim, T. Conant, A.K. Datye, Phys Chem Chem Phys 10 (2008) 5584.

[5] J.A. Schwarz, C. Contescu, A. Contescu, Chem. Rev. 95 (1995) 477.

[6] G.A. Somorjai, J.Y. Park, Top. Catal. 49 (2008) 126.

[7] J.Y. Park, C. Aliaga, J.R. Renzas, H. Lee, G.A. Somorjai, Catal Lett 129 (2009) 1.

[8] C.H. Bartholomew, Appl. Catal., A 212 (2001) 17.

[9] P. Forzatti, L. Lietti, Catal. Today 52 (1999) 165.

[10] P.D. Burton, T.J. Boyle, A.K. Datye, J. Catal. 280 (2011) 145.

[11] I.M. Lifshitz, V.V. Slyozov, Journal of Physics and Chemistry of Solids 19 (1961) 35.

[12] C. Wagner, Journal of Electrochemistry 65 (n.d.) 581.

[13] B.K. Chakraverty, Journal of Physics and Chemistry of Solids 28 (1967) 2401.

[14] C.G. Granqvist, R.A. Buhrman, J. Catal. 42 (1976) 477.

[15] G.M. Schwab, Advances in Catalysis (1979).

[16] F. Solymosi, Catalysis Reviews 1 (1968) 233.

[17] J.G. McCarty, G. Malukhin, D.M. Poojary, A.K. Datye, Q. Xu, J. Phys. Chem. B 109 (2005) 2387.

[18] J. Sehested, A. Carlsson, T.V.W. Janssens, P.L. Hansen, A.K. Datye, J. Catal. 197 (2001) 200.

[19] Q. Xu, K.C. Kharas, B.J. Croley, A.K. Datye, ChemCatChem 3 (2011) 1004.

[20] R. Baker, Catalysis Reviews: Science and Engineering 19 (1979) 161.

[21] R. Baker, Catalysis Reviews: Science and Engineering 19 (1979) 161.

[22] P. Harris, Int. Mater. Rev. 40 (1995) 97.

[23] R. Baker, P.S. Harris, R.B. Thomas, Surf. Sci. 46 (1974) 311.

[24] L.M. Sanders, Diffusion of Three-Dimensional Metal Particles on an Oxide Surface: Implications for the Sintering of Heterogeneous Catalysts, University of New Mexico, Albuquerque, NM USA, 2003.

[25] A.K. Datye, Q. Xu, K.C. Kharas, J.M. McCarty, Catal. Today 111 (2006) 59.

[26] P. Wynblatt, N. Gjostein, Prog. Solid State Chem. 9 (1975) 21.

[27] S.D. Coughlan, M. Fortes, Scripta Metall. Mater. 28 (1993) 1471.

[28] G.A. Fuentes, E. Salinas-Rodriguez, Stud. Surf. Sci. Catal. 139 (2001) 503.

[29] P. Wynblatt, Acta Metallurgica 24 (1976) 1175.

[30] P. Wynblatt, N. Gjostein, in:, P. Emmett, E. Drauglis, R. Jaffee (Eds.), The Physical Basis for Heterogeneous Catalysis, Drauglis, E, 1975, p. 3.

[31] P. Harris, E.D. Boyes, J.A. Cairns, J. Catal. 82 (1983) 127.

[32] P. Harris, J. Catal. 97 (1986) 527.

[33] H.K. Kuo, P. Ganesan, R.J. Deangelis, J. Catal. 64 (1980) 303.

[34] K.T. Kim, S.K. Ihm, J. Catal. 96 (1985) 12.

[35] W.C. Yang, M. Zeman, H. Ade, R.J. Nemanich, Phys. Rev. Lett. 90 (2003) 136102.

[36] S.R. Challa, A.T. Delariva, T.W. Hansen, S. Helveg, J. Sehested, P.L. Hansen, F. Garzon, A.K. Datye, J. Am. Chem. Soc. (2011).

[37] K. Morgenstern, G. Rosenfeld, G. Comsa, Surf. Sci. 441 (1999) 289.

[38] A.D. Rollett, W.W. Mullins, Scripta Mater. 36 (1997) 975.

[39] M. Haruta, N. Yamada, T. Kobayashi, S. Iijima, J. Catal. 115 (1989) 301.

[40] G.C. Bond, D.T. Thompson, Catalysis Reviews 41 (1999) 319.

[41] G.J. Hutchings, J. Catal. 96 (1985) 292.

[42] T. Choudhary, D.W. Goodman, Appl. Catal., A 291 (2005) 32.

[43] M. Valden, X. Lai, D.W. Goodman, Science 281 (1998) 1647.

[44] W. Wallace, B. Min, D.W. Goodman, in:, Top Catal, 2005, pp. 17–30.

[45] W. Stober, A. Fink, E. Bohn, J. Colloid Interface Sci. 26 (1968) 62.

[46] D.R.G. Mitchell, Portal.Tugraz.at (n.d.).

[47] W.T. McGown, C. Kemball, D.A. Whan, M.S. Scurrell, J. Chem. Soc., Faraday Trans. 1 73 (1977) 632.

[48] G.C. Bond, D.A. Dowden, N. Mackenzie, Trans. Faraday Soc. 54 (1958) 1537.

[49] C. Nguyen Than, B. Didillon, P. Sarrazin, C. Campbell, Catalytic Hydrogenation Process and a Catalyst for Use in the Process, 6,040,489, 1999.

[50] W.-J. Kim, S.H. Moon, in:, Catal Today, 2012, pp. 2–16.

[51] Q.W. Zhang, J. Li, X.X. Liu, Q.M. Zhu, Appl. Catal., A 197 (2000) 221.

[52] A. Borodziński, G.C. Bond, Catalysis Reviews 50 (2008) 379.

[53] J. Moses, A.H. Weiss, K. Matusek, L. Guczi, J. Catal. 86 (1984) 417.

[54] A. Pachulski, R. Schödel, P. Claus, Appl. Catal., A 400 (2011) 14.

[55] R.-J. Liu, P.A. Crozier, C.M. Smith, D.A. Hucul, J. Blackson, G. Salaita, Appl. Catal., A 282 (2005) 111.

[56] Y. Jin, A.K. Datye, E. Rightor, R. Gulotty, W. Waterman, C.M. Smith, M. Holbrook, J. Maj, J. Blackson, J. Catal. 203 (2001) 292.

[57] F. Studt, F. Abild-Pedersen, T. Bligaard, R.Z. Sorensen, C.H. Christensen, J.K. Nørskov, Science 320 (2008) 1320.

[58] D. Duca, F. Arena, A. Parmaliana, G. Deganello, Appl. Catal., A 172 (1998) 207.

[59] M. Bauer, R. Schoch, L. Shao, B. Zhang, A. Knop-Gericke, M. Willinger, R. Schlögl, D. Teschner, J. Phys. Chem. C 116 (2012) 22375.

[60] G.A. Somorjai, J.Y. Park, Angew. Chem. 47 (2008) 9212.

[61] B. Ravel, M. Newville, J. Synchrotron Radiat. 12 (2005) 537.

[62] M. Newville, J. Synchrotron Radiat. 8 (2001) 96.

[63] S. Zabinsky, J. Rehr, A. Ankudinov, R. Albers, M. Eller, Phys. Rev. B: Condens. Matter 52 (1995) 2995.

[64] X. Liu, C. Mou, S. Lee, Y. Li, J. Secrest, Ben W L Jang, J. Catal. 285 (2012) 152.

[65] W.G. Menezes, L. Altmann, V. Zielasek, K. Thiel, M. Bäumer, J. Catal. 300 (2013) 125.

[66] L. Shao, B. Zhang, W. Zhang, D. Teschner, F. Girgsdies, R. Schlögl, D.S. Su, Chem. --Eur. J. 18 (2012) 14962.

[67] A.M. Karim, V. Prasad, G. Mpourmpakis, W.W. Lonergan, A.I. Frenkel, J.G. Chen, D.G. Vlachos, J. Am. Chem. Soc. 131 (2009) 12230.

[68] S. Calvin, C.J. Riedel, E.E. Carpenter, S.A. Morrison, R.M. Stroud, V.G. Harris, Phys Scripta T115 (2005) 744.

[69] A.I. Frenkel, C.W. Hills, R.G. Nuzzo, J. Phys. Chem. B 105 (2001) 12689.

[70] S. Calvin, S.X. Luo, C. Caragianis-Broadbridge, J.K. McGuinness, E. Anderson, A. Lehman, K.H. Wee, S.A. Morrison, L.K. Kurihara, Appl Phys Lett 87 (2005) 233102.

[71] H.N. Pham, A.E. Anderson, R.L. Johnson, K. Schmidt-Rohr, A.K. Datye, Angew. Chem. 51 (2012).

[72] M.W. Tew, M. Janousch, T. Huthwelker, J.A. van Bokhoven, J. Catal. 283 (2011) 45.

[73] D. Teschner, E. Vass, M. Hävecker, S. Zafeiratos, P. Schnörch, H. Sauer, A. Knop-Gericke, R. Schlögl, M. Chamam, A. Wootsch, A. Canning, J. Gamman, S.D. Jackson, J. McGregor, L. Gladden, J. Catal. 242 (2006) 26.

[74] B. Yang, R. Burch, C. Hardacre, P. Hu, P. Hughes, J. Phys. Chem. C (2014).

[75] M.W. Tew, M. Nachtegaal, M. Janousch, T. Huthwelker, J.A. van Bokhoven, Phys Chem Chem Phys 14 (2012) 5761.

[76] J.M. Montejano-Carrizales, J.M. Montejano-Carrizales, J.M. Montejano-Carrizales, J.M. Montejano-Carrizales, F. Aguilera-Granja, F. Aguilera-Granja, F. Aguilera-Granja, F. Aguilera-Granja, J.L. Moran-Lopez, J.L. Moran-Lopez, J.L. Moran-Lopez, J.L. Moran-Lopez, Nanostruct. Mater. 8 (1997) 269.

[77] C. Campbell, C.H. Peden, Science 309 (2005) 713.

[78] B.-S. Shin, J.-H. Bae, J.-P. Yoo, S.-J. Choung, Y.-I. Song, G.-K. Yeo, Korean J. Chem. Eng. 15 (1998) 474.

[79] E.L. Brosha, R. Mukundan, D.R. Brown, F.H. Garzon, J.H. Visser, Solid State Ionics 148 (2002) 61.

[80] R. Mukundan, E.L. Brosha, D.R. Brown, F.H. Garzon, J. Electrochem. Soc. 147 (2000) 1583.

[81] E.P. Murray, T. Tsai, S.A. Barnett, Nature 400 (1999) 649.

[82] V.V. Kharton, F. Marques, A. Atkinson, Solid State Ionics 174 (2004) 135.

[83] T. Bunluesin, E.S. Putna, R.J. Gorte, Catal Lett 41 (1996) 1.

[84] M. Cargnello, V.V.T. Doan-Nguyen, T.R. Gordon, R.E. Diaz, E.A. Stach, R.J. Gorte, P. Fornasiero, C.B. Murray, Science 341 (2013) 771.

[85] S. Hilaire, X. WANG, T. Luo, R.J. Gorte, J. Wagner, Appl. Catal., A 215 (2001) 271.

[86] M.-F. Luo, Z.-Y. Hou, X.-X. Yuan, X.-M. Zheng, Catal Lett 50 (1998) 205.

[87] D.R. Mullins, P.M. Albrecht, F. Calaza, Top. Catal. 56 (2013) 1345.

[88] J.L. Lu, H.J. Gao, S. Shaikhutdinov, H.J. Freund, Surf. Sci. 600 (2006) 5004.

[89] H.-X. Mai, L.-D. Sun, Y.-W. Zhang, R. Si, W. Feng, H.-P. Zhang, H.-C. Liu, C.-H. Yan, J. Phys. Chem. B 109 (2005) 24380.

[90] Z. Wu, M. Li, S.H. Overbury, J. Catal. 285 (2012) 61.

[91] K. Zhou, X. Wang, X. Sun, Q. Peng, Y. Li, J. Catal. 229 (2005) 206.

[92] R. Si, M. Flytzani-Stephanopoulos, Angew. Chem. 47 (2008) 2884.

[93] S. Agarwal, L. Lefferts, B.L. Mojet, D.A.J.M. Ligthart, E.J.M. Hensen, D.R.G. Mitchell, W.J. Erasmus, B.G. Anderson, E.J. Olivier, J.H. Neethling, A.K. Datye, ChemSusChem 6 (2013) 1898.